THE PLANNING OF A SOUTH AFRICAN AIRBORNE SYNTHETIC APERTURE RADAR MEASURING CAMPAIGN

L.A. Alexander

April 24, 1994

Declaration

I declare that this dissertation is my own work. It is being submitted for the degree of Master of Science in Engineering at the University of Cape Town. It has not been submitted before for any degree or examination at this or any other university.

Signed by candidate
Signature Removed

Leon Alexander

Acknowledgments

My grateful thanks to Nikita Wullschleger and Dr. Robert Newton, both of the Geology Department at the University of Cape Town for their assistance. Nikita is at present investigating the use of remote sensing, in particular Landsat TM imagery for the interpretation of the Southern Kalahari geology. He provided most of the Kalahari literature used in this thesis. Both Nikita and Dr. Newton gave invaluable assistance with the geology aspect of the proposed campaign.

I would also like to thank Tom Alsen, Becky Eatock, Jasper Horrel, Alastair Knight, Marten Kabutz and Alan Langman of the Radar Remote Sensing Group for their assistance. A special thanks to Prof. Inggs to whom I feel deeply indebted for his advice and assistance throughout the project.

Finally, I wish to thank my parents and brothers for their support.

Synopsis

This thesis sets out the results of work done in preparation for a South African Airborne Synthetic Aperture Radar (SAR) measuring campaign envisaged for 1994/5. At present both airborne and spaceborne SARs have found a niche in remote sensing with applications in subsurface mapping, surface moisture mapping, vegetation mapping, rock type discrimination and Digital Elevation Modelling. Since these applications have considerable scientific and economic benefits, the Radar Remote Sensing Group at the University of Cape Town committed themselves to an airborne SAR campaign. The prime objective of the campaign is to provide the South African users with airborne SAR data and enable the Radar Remote Sensing Group to evaluate the usefulness of SAR as a remote sensing tool in South Africa.

In this thesis the details of how SAR images are formed are not important. Instead, the emphasis is on how the electromagnetic wave interacts with the surface because this determines how and what a SAR can measure. To this end, theoretical models namely, physical optics, small perturbation and geometric optics models were investigated since these models enable the backscatter from a randomly rough surface to be determined. The Bragg resonance phenomena, which accounts for the relatively high backscatter from periodic surfaces was also investigated since this model is important in many sea surface imaging applications. Because the theoretical models are difficult to use, empirical and semi-empirical models are popular. In subsurface applications, the penetration depth is determined by the microwave attenuation in the sand medium. The factors affecting the microwave attenuation in sand are the frequency of the radar signal, and the real and imaginary part of the permittivity. The lower the frequency, and the lower the loss tangent (defined as the ratio of imaginary part of the permittivity to the real part of the permittivity), the lower the microwave attenuation in the sand medium.

Both attenuation and scattering models are functions of the complex dielectric constant of the medium. This necessitated the need for an investigation into the factors influencing the complex permittivity of soil. These factors, listed in order of greatest influence are soil moisture, soil water salinity, soil type, soil density and soil temperature. The relative permittivity of dry soil ranges from 3 to 4, independent of frequency. As water is added, the relative dielectric permittivity increases rapidly as pure water has a value of approximately 80 for frequencies below 1 GHz. It is therefore obvious that the dielectric constant of a soil is greatly influenced by the volumetric water content. The water content of soil generally

consists of *free* and *bound* water where the amount of *bound* water is determined by the surface area of the soil particles. The smaller the individual soil particles the greater the total surface area. Thus, the amount of *bound* water in the soil is dependent on the soil textural composition. The real part of the complex dielectric constant of soil water is unaffected by salt content whereas the imaginary part of the complex dielectric constant is affected, especially at low frequencies where ionic conductivity dominates. The remaining factors have negligible influence on the permittivity. Theoretical and empirical models for soil permittivity are available but the latter is more popular because the theoretical models are complicated and require too many input variables. The empirical models are not without problems. The real part of the permittivity can be successfully modelled from about 1 MHz to 18 GHz, whereas the imaginary part of the permittivity can only be successfully modelled from about 1 GHz to 18 GHz because the effects of ionic conductivity, which cannot easily be included in the model, dominate at frequencies lower than 1 GHz.

Polarimetric imagery is a relatively new development in radar imagery and is at present an active research area. Polarimetric radars have the capability of identifying a scatterer from its polarization signature which is obtained by a technique known as polarization synthesis. For example, a dihedral corner reflector signature can be used to identify buildings in an image, or a large smooth dielectric surface signature indicates the locations of clear-cut areas in an image of forest vegetation.

Next, the intended applications namely, subsurface geological mapping, surface rock type discrimination, near-surface soil moisture content mapping, vegetation mapping, and Digital Elevation Modelling are discussed. Since the prime objective of this thesis is the planning of an airborne SAR campaign, the most important part of each application discussed is the optimum parameters for that application.

There are numerous geological applications of SAR which generally fall into one of two groups, namely surface and subsurface applications. The latter, which is a unique feature of radar imaging, will be discussed first. Low loss material, such as dry sand, which covers most of the surface of arid regions can easily be penetrated with low frequency radar. Thus, the images formed reveal the subsurface geology. The optimum parameters for subsurface imaging are chosen to minimize the microwave attenuation or maximize the microwave penetration depth in the medium. For a given frequency and soil moisture content, sand consistently has the lowest attenuation. However, the greatest influence on microwave attenuation is the moisture content of the soil. Greater microwave penetration is observed for soils with lower moisture content. In addition, lower radar frequencies yield greater microwave penetration of the obscuring medium. The optimum incidence angle for subsurface imaging is a compromise between minimizing the path length

in the sand medium and avoiding incidence angles at which specular reflections at the air-sand interface dominates the radar backscatter. Thus the optimum incidence angle for subsurface applications is between 10° and 20°.

SAR has been used very successfully in rock type discrimination since it is uniquely sensitive to the roughness or texture of the surface being imaged. The growing trend to use multifrequency and multipolarization radars has enabled considerably more information about the surface to be extracted from the radar image. The most powerful means of discriminating between surfaces with different degrees of roughness is to exploit the wavelength dependence of the Rayleigh criterion. In this way roughnesses can be used to aid in the mapping of different lithologies and superficial deposits in terrain that is bare of vegetation. Also, the use of multipolarization has enabled rock types to be mapped with greater accuracy since each rock type can be matched to a particular polarization signature which is obtainable via a technique known as polarization synthesis.

SAR has the ability to measure the near-surface soil moisture content remotely. Radar backscatter is influenced by physical parameters (surface roughness and surface permittivity) and radar parameters (incidence angle, frequency and polarization). The soil moisture is inferred from the surface permittivity which is in turn deduced from the measured radar backscatter. To determine soil moisture content from radar backscatter successfully, requires the effects of vegetation, surface roughness and local incidence angle on the observed backscatter to be minimized or removed completely. This is accomplished by choosing an optimum frequency, incidence angle and polarization for imagery from which the soil moisture content will be extracted. Several researches have shown that the optimum parameters for soil moisture measurement is an incidence angle of 10°, a frequency of 4 GHz, and HH or VV polarization.

The feasibility of vegetation type discrimination, particularly for crop type distribution mapping was also investigated. To distinguish between two crops in a radar image requires that the backscatter from these crops differ in intensity. This backscatter intensity is influenced by vegetation parameters such as the canopy density and crop height. Unfortunately, the measured backscatter is also greatly influenced by the soil moisture and roughness. Hence, successful vegetation mapping depends on the degree to which the effect of the soil moisture can be minimized. Researchers have shown that the soil moisture influence is minimized by using incidence angles of approximately 40° and frequencies in the vicinity of 8 GHz.

Two sea surface imaging applications were investigated namely, oil pollution and fish shoal monitoring. Detecting, monitoring and mapping of oil spills on the sea surface are applications based on the Bragg scattering phenomenon which accounts for the observed sensitivity of imaging radars to the amplitude of ocean capillary waves. The presence of oil on the ocean surface significantly reduces

the amplitude of capillary waves which in turn significantly reduces the radar backscatter from that surface. Thus, oil on the sea surface corresponds to dark patches. Fish shoal monitoring is also based on the Bragg scattering phenomenon. Researchers have shown that certain fish species such as the bluefin tuna break the water surface by repeatedly jumping out of the water. This behaviour, which is associated with feeding, produces a rough surface which results in greater backscatter and thus appears as a bright feature in the radar image. Similarly, net floats cause a roughening of the surface which enables the location of the nets to be mapped. The optimum parameters for sea surface imaging applications are difficult to determine because of insufficient data on the subject. Nevertheless, an estimate of the optimum frequency and incidence angles are gleaned from the limited literature on the topic. Since Bragg scattering is the theoretical basis for both oil pollution and shoal monitoring, these applications are probably optimum at high frequencies (X-band), large incidence angles (40°), and VV polarization.

Digital Elevation Models (DEM) can be generated by extracting topographic information from SAR data using Shape-from-shading, Stereoscopic imaging and Interferometric SAR techniques. In shape-from-shading, the radar backscatter is assumed to be proportional to the local incidence angle which is a function of the terrain slope and incidence angle. Since the incidence angle is fixed by the sensor hardware, the slope of the terrain can be inferred from the backscatter. The DEM is then constructed from the terrain slope information. The accuracy of the DEM is extremely sensitive to the accuracy with which the backscatter intensity versus local incidence angle can be modelled. The accuracy of the model is in turn dependent on the roughness of the terrain because rougher surfaces yield better models. Since roughness is frequency dependent, higher frequencies yield better models. An exact frequency can only be determined if the surface roughness is known but C-band frequencies will probably be high enough. The optimum incidence angle is chosen to minimize the likelihood of layover and shadowing. Without *a priori* knowledge of the topography, the optimum incidence angle is 45°.

Stereoscopy is another technique whereby topographic information can be extracted from two overlapping images. The method is based on the apparent movement or parallax of features in the stereo image pair. The elevation of a feature is proportional to the observed parallax of the feature. The method requires two images of similar image quality, tone and texture, but different imaging geometry to present parallaxes for the height perception. The optimum stereo geometry is a compromise between two equally important criteria. Firstly, the two images forming the stereo pair must be very similar in image quality, terrain illumination, tone and texture so that the stereo pair correlates well. Secondly, the two images forming the stereo pair must be sufficiently different in geometry to present parallaxes for height perception. Since radar actively illuminates the terrain, significant differences in viewing geometry also imply illuminations differ-

ences. In addition, the optimum incidence angles and intersection angle are also dependent on the terrain relief. For relatively flat terrain, the incidence angles should range from about 20° to 60° with an intersection angle greater than about 30°. For relatively high relief terrain, the incidence angles should range from 40° to 70° with intersection angles ranging from 15° to 30°.

Due to the coherent nature of SAR, interferometric principles can be used to extract height information from raw SAR data. If two receiving antenna are placed in the range-height plane, then the phase difference of the echoed power can be determined. This means that differences in height, modulo the radar wavelength, can be detected. In this way three dimensional terrain maps can be constructed. The accuracy of the DEM is maximized through minimization of phase errors, wavelength, and slant range and maximization of the baseline distance. However, the level of phase noise in the system increases with increasing baseline distance up to a critical baseline distance where the signals are no longer correlated. It can be shown that the optimum baseline distance ranges from 0.2 to 0.8 of the critical baseline distance. These baseline distances are limited by aircraft dimensions when both antennas are mounted on the same aircraft which implies that the frequency can be chosen so that the baseline distance is optimum.

Ideally, one imaging radar could be configured to have frequency and incidence angle ranges that would contain the optimum parameters for all the envisaged applications. Unfortunately, a combination of financial and technical limitations made this ideal imaging radar unrealistic. Hence, some compromises had to be made which automatically implied implementing some applications with less than optimum imaging parameters.

The details of the proposed South African airborne SAR campaign is contained in the appendix.

Contents

List of Figures

List of Tables

Chapter 1

Introduction

This thesis sets out the results of work done in preparation for a South African Airborne Synthetic Aperture Radar (SAR) measuring campaign envisaged for late 1994. Since the development of the first SAR in the 1950's, the capabilities of SARs have steadily improved to the present-day high resolution, multifrequency and multipolarization SARs. Both airborne and spaceborne SARs have found a niche in remote sensing with applications in subsurface mapping, surface moisture mapping, vegetation mapping, rock type discrimination and Digital Elevation Modelling (DEM). Since these applications have considerable scientific and economic benefits, the Radar Remote Sensing Group (RRSG) at the University of Cape Town (UCT) committed themselves to an airborne SAR campaign.

The prime objective of the campaign is to provide the South African users with airborne SAR data and enable the Radar Remote Sensing Group to evaluate the usefulness of SAR as a remote sensing tool in South Africa. This will be carried out through a number of project objectives :

- To investigate the capability of a unique low frequency radar to penetrate the sand cover of arid regions enabling the subsurface geology to be mapped.
- To attempt to locate subsurface water in arid regions.
- To determine the feasibility of using radar images for rock type discrimination.
- To investigate the feasibility of measuring surface soil moisture.
- To investigate the feasibility of mapping the distribution of a crop such as sugar cane.
- To investigate the feasibility of using stereo radar imaging or Shape-From-Shading techniques to generate Digital Elevation Models (DEM).

- To investigate the feasibility of Interferometric SAR for the generation of DEMs.
- To determine the feasibility of detecting oil spills using an imaging radar. This involves a controlled oil spill off the South African coast, followed by cleaning up operations.
- To determine the feasibility of using radar images of the sea surface to determine the location of schools of fish. This technique can also be used to monitor large marine mammals such as whales.

Synthetic Aperture Radar (SAR) was invented because of an ever increasing need for higher resolution in ground mapping radars. Conventional ground mapping radars were designed to achieve range resolution by the radiation of a short pulse and azimuth resolution by the radiation of a narrow beam. Pulse compression techniques can be used to obtain shorter pulses. However, SAR derives its name from the technique used to improve resolution in azimuth. Beamwidth is a function of antenna dimensions and frequency, thus the bigger the antenna, the narrower the beamwidth. SAR is based on the generation of an effective long antenna by signal-processing means rather than by the actual use of a long physical antenna. Very detailed descriptions of SAR can be found in Curlander [16] and Hovanessian [51, p211]. Since SAR is an active system that transmits a beam of electromagnetic (EM) radiation in the microwave and radio frequency region, it is not dependent on the sun and can thus be used at any time of the day or night. In addition, clouds (consisting of water vapour) have very little effect at microwave and radio frequency EM radiation and thus permit all-weather SAR operation.

In this thesis the details of how SAR images are formed are not important. Instead, the emphasis is on how the electromagnetic wave interacts with the surface because this determines how and what a SAR can measure. Thus, the report begins with a chapter on electromagnetic wave interaction at the surface and inside the medium. Topics covered are: an expression for electromagnetic attenuation of the wave inside the medium, reflection coefficients of layered mediums and an extensive section on electromagnetic surface scattering. This subsection includes a discussion of both theoretical and empirical surface scattering models which, as will be shown later, is crucial to many SAR applications.

Both attenuation and scattering models (discussed in the previous chapter) are functions of the complex dielectric constant of the medium. This necessitated the need for a separate chapter on the complex dielectric properties of soil. Topics covered in this chapter include a brief overview of the techniques used to measure the complex permittivity, a discussion of the factors affecting the complex permittivity of soil, and a discussion highlighting the successes and failures of permittivity models.

The next chapter discusses the advances made in polarimetry, in particular the theoretical bases for polarization signature synthesis. The chapter aims to show the reader the origin of polarization signatures and how it can be used to identify the geometry of the scatterer. However, polarimetric applications are discussed in the chapters dealing with particular applications.

SAR has made a significant contribution to remote sensing of geology especially in arid regions where mapping of paleodrainages and the detection of subsurface water is possible. Since most of South Africa is semi-arid, a large section of the chapter on geological applications of SAR is devoted to subsurface mapping. This is followed by a section on surface mapping which discusses methods for extracting geological information from SAR images. Since the prime objective of this thesis is the planning of an airborne SAR campaign, the most important section of this chapter is a discussion of the optimum parameters for a particular application. The geology chapter contains two sets of optimum radar and soil parameters namely, subsurface and surface mapping parameters.

The following chapter discusses near-surface soil moisture measurement and vegetation type discrimination. These two topics are discussed simultaneously because it is impossible to separate the backscatter components attributable to soil and vegetation completely, i.e. the backscatter of an agricultural scene is invariably the sum of backscatter from both vegetation and soil. Firstly, the measurement of non-vegetated soil moisture is discussed. This is then extended to the moisture measurement of vegetated soils. Next, techniques for vegetation type discrimination are discussed. The optimum parameters for both soil moisture measurement and vegetation type discrimination are also discussed.

By a phenomenon known as Bragg scattering, imaging radars are extremely sensitive to capillary waves on the sea surface. Therefore, a chapter on sea surface imaging discusses two applications based on the Bragg scattering phenomena namely, detecting oil spills on the sea surface and monitoring schools of fish just below the sea surface. The chapter ends with a section on optimum parameters for sea surface imaging.

The following chapter deals with three methods for obtaining Digital Elevation Models (DEM). The methods are: Shape-From-Shading, Stereoscopic imaging and Interferometric SAR (InSAR). Each method is discussed separately since the techniques used and the parameters at which the accuracies are maximized are different for each application.

The thesis concludes with a summary of the applications and shows that the choice of the radar parameters for any SAR campaign is a compromise.

The details of the proposed South African airborne SAR campaign is contained in the appendix.

Chapter 2

Electromagnetic theory

SAR images are two-dimensional plots of radar reflectivity or backscatter intensity with each pixel in the image representing the average backscatter of a resolvable area. The backscatter intensity is predominantly affected by surface or subsurface properties such as permittivity and roughness. To relate the backscatter to surface characteristics, a model for electromagnetic (EM) surface scattering is required. Also, for subsurface applications, the attenuation of EM waves in the medium as well as the backscatter from the surface and subsurface layers needs to be modelled. Hence, this chapter discusses attenuation of EM waves inside a medium, EM reflection coefficients of layered mediums and, in particular, the EM scattering from random surfaces.

2.1 Electromagnetic (EM) wave loss mechanisms

This section discusses the loss mechanisms experienced by radar signals in a homogeneous medium, namely volume scattering and conduction. The mechanism of volume scattering causes a redistribution of the energy in the transmitted wave into other directions. This results in a loss from the transmitted wave. Also, a propagating wave inside a physical medium experiences a loss due to conduction. The total loss which is the sum of scattering and conduction losses is usually referred to as extinction.

2.1.1 The volume scattering loss mechanism

The scattering loss is usually negligible compared to the conduction loss. Roth [78] showed that for a finite range of frequencies and/or particle size the scattering

loss can be of a similar order of magnitude as the conduction loss. In Roth's expression (see Equation 2.1), r_0 is the average size of the particles which constitute the medium and λ is the wavelength of the transmitted signal. The scattering loss is large in a general region indicated by the formula below.

$$0.1 < \frac{r_0}{\lambda} < 100 \tag{2.1}$$

For subsurface geological applications, the medium through which the radar signal is expected to penetrate is sand with an average particle size usually less than 1 mm (see Appendix B). Thus, for wavelengths longer than 1 cm (or frequencies below 30 GHz), the scattering loss is negligible.

2.1.2 The conduction loss mechanism

The main loss mechanism in microwave propagation is the conduction loss, since scattering loss is negligible for the medium and frequencies used. The conduction loss is automatically included in the solution to Maxwell's equations when a lossy medium is assumed. The conduction loss is implicit in the terms (loss tangent, skin depth or penetration depth) used in subsurface radar applications to express the signal attenuation in the medium. The mathematics described below shows the origin of the loss tangent, skin depth and penetration depth.

The differential form of Maxwell's equations shown below is for an isotropic, source free, *lossy* medium.

$$\nabla \times E = -\mu \frac{\partial H}{\partial t} \tag{2.2}$$

$$\nabla \times H = \sigma E + \varepsilon \frac{\partial E}{\partial t} \tag{2.3}$$

ε = permittivity of the medium,
μ = permeability of the medium,
σ = conductivity of the medium.

The time harmonic form of Maxwell's equations are solved by Ulaby [98, p65]. The solution is given for a wave propagating through a lossy medium in the z direction.

$$E_x(z) = E_{xo} \exp(-\jmath\omega\sqrt{\mu\varepsilon_c}z) \tag{2.4}$$

The characteristic permittivity ε_c consists of a real and imaginary part.

$$\varepsilon_c = \varepsilon - \jmath\frac{\sigma}{\omega} \tag{2.5}$$

$$= \varepsilon' - \jmath\varepsilon'' \tag{2.6}$$

Throughout this thesis the real part of the permittivity will be assigned the variable ε', and the imaginary part, ε''.

Further expansion of Equation 2.4 results in

$$\jmath\omega\sqrt{\mu\varepsilon_c} = \jmath k\sqrt{(\varepsilon_r' - \jmath\varepsilon_r'')} \tag{2.7}$$

where the relative permittivity ε_r is given by

$$\varepsilon_r = \varepsilon_c\varepsilon_0 \tag{2.8}$$

and the wave number k is given by

$$k = \omega\sqrt{\mu\varepsilon} = \frac{2\pi}{\lambda}. \tag{2.9}$$

Equation 2.7 can be written in a form which makes it easier to define the field attenuation coefficient α and the phase constant β.

$$\jmath\omega\sqrt{\mu\varepsilon_c} = \alpha + \jmath\beta \tag{2.10}$$

$$\alpha = k\left[\frac{1}{2}(\sqrt{1+\tan^2\delta} - 1)\right]^{\frac{1}{2}} \tag{2.11}$$

$$\beta = k\left[\frac{1}{2}(\sqrt{1+\tan^2\delta} + 1)\right]^{\frac{1}{2}} \tag{2.12}$$

The loss tangent, $\tan\delta$ is defined as :

$$\tan \delta = \frac{\sigma}{\omega \varepsilon} = \frac{\varepsilon''}{\varepsilon'} \tag{2.13}$$

The most often quoted value in subsurface radar imaging is the skin depth δ_s. The skin depth δ_s is defined as the inverse of the field attenuation coefficient α. A value sometimes quoted is the penetration depth δ_p. This value is also a function of the field attenuation coefficient.

$$\delta_s = \frac{1}{\alpha} \tag{2.14}$$

$$\delta_p = \frac{1}{2\alpha} \tag{2.15}$$

The values for skin depth and penetration depth do not indicate the subsurface depth to which the radar can successfully image. The skin depth and penetration depth are determined by the medium through which the microwaves are propagating, whereas the image depth is determined by the parameters of the imaging radar as well as the medium in which the wave is propagating. The image depth is usually a fraction of the skin depth value.

The above section has shown that the conduction loss is indirectly referred to when the loss tangent, skin depth or penetration depth is quoted in literature. These terms are defined in equations 2.13, 2.14 and 2.15. Equations 2.9, 2.11 and 2.13 can be combined to obtain an equation for α as a function of complex dielectric constant and radar wavelength.

$$\alpha = \frac{2\pi}{\lambda_0} \left\{ \frac{\mu_r \varepsilon_r'}{2} \left[\left(1 + \left(\frac{\varepsilon_r''}{\varepsilon_r'} \right)^2 \right)^{\frac{1}{2}} - 1 \right] \right\}^{\frac{1}{2}} \tag{2.16}$$

λ_0 = Wavelength in free space,
μ_r = Relative permeability of the material. For most earth materials, $\mu_r \approx 1$.

A thorough treatment of electromagnetic theory is contained in the books by Balanis [4] and Chew [14].

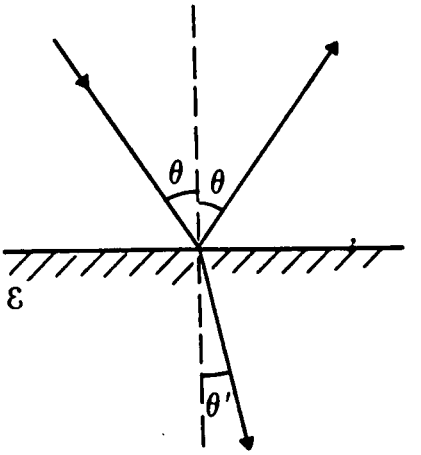

Figure 2.1: An illustration of two homogeneous mediums with a radar signal being absorbed and reflected. (Elachi [28, p12])

2.2 Layered mediums

A plane wave incident on a medium will in general be partially absorbed and partially reflected as illustrated in Figure 2.1. To determine the amount of energy that will be absorbed and/or reflected, the reflection and transmission coefficients need to be calculated. Expressions for the reflection (2.17, 2.18) and transmission (2.19, 2.20) coefficients can be found in Ulaby [98, p73].

Any transmitted signal can be decomposed into two orthogonal components, namely TE and TM waves. When the E field vector is perpendicular to the plane of incidence, it is said to be perpendicularly polarized, horizontally polarized, or a TE wave. When the E field vector is parallel to the plane of incidence, it is said to be parallel polarized, vertically polarized, or TM wave. Thus, expressions 2.17 and 2.19 are for TE waves, and expressions 2.18 and 2.20 are for TM waves.

$$R_{\perp} = \frac{\eta_2 \cos\theta_1 - \eta_1 \cos\theta_2}{\eta_2 \cos\theta_1 + \eta_1 \cos\theta_2} \tag{2.17}$$

$$R_{\parallel} = \frac{\eta_1 \cos\theta_1 - \eta_2 \cos\theta_2}{\eta_1 \cos\theta_1 + \eta_2 \cos\theta_2} \tag{2.18}$$

$$T_{\perp} = \frac{2\eta_2 \cos\theta_1}{\eta_2 \cos\theta_1 + \eta_1 \cos\theta_2} \tag{2.19}$$

$$T_{\parallel} = \frac{2\eta_1 \cos\theta_1}{\eta_1 \cos\theta_1 + \eta_2 \cos\theta_2} \tag{2.20}$$

In the above formulas, the intrinsic impedance η is given by

$$\eta = \sqrt{\frac{\mu}{\varepsilon}} \tag{2.21}$$

and θ_1 is the incidence angle of the transmitted radar signal. The transmission angle θ_2 is calculated by substituting k_1, k_2 (Equation 2.9) and θ_1 into Snell's Law (Equation 2.22).

$$k_1 \sin\theta_1 = k_2 \sin\theta_2 \tag{2.22}$$

Equations 2.17 to 2.21 show that the intrinsic impedance of the medium determines the amount of reflected energy. Since the permeability $\mu \approx 1$ for most earth materials, the complex permittivity ε determines the amount of energy reflected at the interface. Hence, chapter 3 is devoted entirely to the measuring and modelling of the complex permittivity.

It should be noted that there exists an incidence angle at which total transmission (or zero reflection) occurs for vertically polarized waves. This angle is known as the Brewster angle, θ_B. To calculate the Brewster angle, use Equation 2.18. Since no reflection occurs at the boundary,

$$R_{\|} = 0 \tag{2.23}$$

which, together with Snell's Law gives

$$\tan\theta_B = \sqrt{\frac{\varepsilon_2}{\varepsilon_1}}. \tag{2.24}$$

The phenomenon of total transmission does *not* occur for horizontally polarized waves.

2.3 Surface Scattering

The surface scattering strength is proportional to the relative complex dielectric constant of the surface and the angular scattering pattern is governed by the surface roughness. Thus, to determine the amount of energy reflected in any direction requires sophisticated scattering models. Surfaces are generally classified into two extremes, either smooth or rough. In reality, a surface will exhibit both smooth and rough surface characteristics making classification difficult. In spite of this classification problem, the terms smooth and rough are commonly used. The progression from smooth surface to rough surface is illustrated in Figure 2.2.

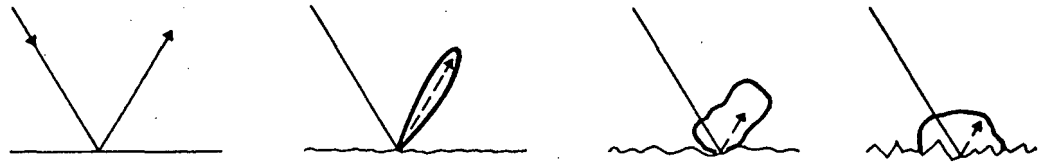

Figure 2.2: An illustration of surface scattering patterns. The patterns show the relative strength and direction of the backscatter. (Elachi [28, p13])

2.3.1 Smooth surfaces

If the incident signal is specularly reflected, the surface from which it reflected is labelled 'smooth'. A smooth surface obeys the Fresnel reflection laws, i.e. the incidence angle θ_i is equal to the reflection angle θ_r. Specular reflection is also known as the coherent scattering component.

2.3.2 Rough surfaces

If the incident signal is reflected or scattered in all directions, the surface from which it was reflected is labelled 'rough'. In this extreme case, the scattering pattern approaches that of a Lambertian surface. Scattering from rough surfaces is also known as the diffuse or non-coherent scattering component.

Since the angular scattering pattern is governed by the surface roughness, a quantitative description of the surface is needed. Two parameters are used to indicate the degree of roughness of a surface, namely the standard deviation of the surface height, σ and the surface correlation length, l. The definition of σ and l given below was obtained from Ulaby [98, p822]

Standard deviation of surface height (σ)

Assume that a rough surface can be modelled by the expression $z(x, y)$ where the height at any point (x, y) is given by $z(x, y)$. Now consider the dimensions of the area to be given by L_x and L_y. The mean height is given by

$$\overline{z} = \frac{1}{L_x L_y} \int_{L_x/2}^{-L_x/2} \int_{L_y/2}^{-L_y/2} z(x, y)\, dx\, dy \tag{2.25}$$

and the second moment is

$$\overline{z^2} = \frac{1}{L_x L_y} \int_{L_x/2}^{-L_x/2} \int_{L_y/2}^{-L_y/2} z^2(x,y)\, dx\, dy. \tag{2.26}$$

The standard deviation of the surface height, σ is then given by

$$\sigma = (\overline{z^2} - \overline{z}^2)^{\frac{1}{2}} \tag{2.27}$$

This expression is usually reduced to one dimension since $z(x)$ and $z(y)$ is statistically independent of $z(x,y)$, i.e the height profile in the x direction is in no way influenced by the height profile in the y direction. For numerical manipulation, the continuous profile is digitized into discrete values. Ulaby [98, p823] suggests that the sample spacing be less than one-tenth the radar wavelength ($\Delta \leq 0.1\lambda$).

In the one dimension discrete case, σ is given by

$$\sigma = \left[\frac{1}{N-1} \left(\sum_{i=1}^{N} (z_i)^2 - N(\overline{z})^2 \right) \right]^{\frac{1}{2}} \tag{2.28}$$

where

$$\overline{z} = \frac{1}{N} \sum_{i=1}^{N} z_i$$

and N is the number of samples.

Surface correlation length (l)

The normalized autocorrelation function for a one-dimensional surface profile z(x) is defined as

$$\rho(x') = \frac{\int_{L_x/2}^{-L_x/2} z(x)\, z(x+x')\, dx}{\int_{L_x/2}^{-L_x/2} z^2(x)\, dx} \tag{2.29}$$

The above expression is a measure of the similarity between the height z at a point x and at a point x' distance from x.

For the discrete case, $x' = (j-1)\,\Delta\, x$ where j is an integer greater than one and Δx is the sample spacing, the formula is

$$\rho(x') = \frac{\sum_{i=1}^{N+1-j} z_i \, z_{j+i-1}}{\sum_{i=1}^{N} z_i^2} \tag{2.30}$$

The surface correlation length l is defined as the displacement x' for which $\rho(x')$ is equal to $1/e$. This implies that if two points are separated by a distance greater than l, then their heights may be considered to be statistically independent of one another.

Criteria for "smoothness"

The Rayleigh criterion states that if the phase difference between the two reflected rays shown in Figure 2.3 is less than $\pi/2$ radians, then the surface may be considered smooth.

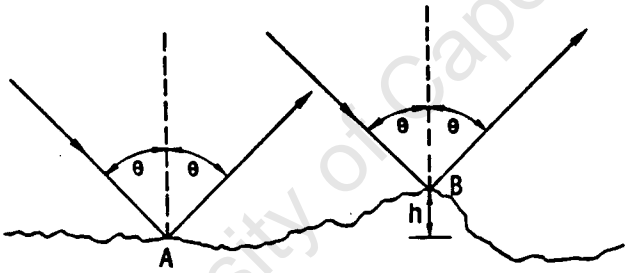

Figure 2.3: An illustration of two coherent rays reflecting from a rough surface. (Ulaby [98, p827])

The phase difference between rays reflected from points A and B is $\triangle\phi = 2kh\cos\theta$ where $k = 2\pi/\lambda$. For $\triangle\phi < \pi/2$, then

$$h < \frac{\lambda}{8\cos\theta} \tag{2.31}$$

In the Rayleigh criterion, h is taken to be the average micro-height variation of the surface. A more stringent criterion, the Fraunhofer Criterion [98, p827], is sometimes used because it is more consistent with experimental observations.

$$h < \frac{\lambda}{32 \cos \theta} \tag{2.32}$$

2.3.3 Surface Scattering Models

The Kirchhoff Scattering Model

The Kirchoff or Physical Optics Model is one of the most commonly used scattering models. This model assumes that plane boundary reflection occurs at every point on the surface which implies that a local region of the surface boundary is treated as an inclined plane. This places the following restrictions on the use of Kirchhoff's model.

$$kl > 6 \tag{2.33}$$

$$l^2 > 2.76\sigma\lambda \tag{2.34}$$

Where k is the wave number and λ is the wavelength of the transmitted signal. The correlation length l and standard deviation σ is defined in Section 2.3.2. The analytic solution to Kirchhoff's model based only on the above assumptions is difficult, hence additional assumptions are needed to obtain an approximate analytic solution. The two additional assumptions are :

- For surfaces with large standard deviation of surface heights the *stationary-phase approximation* will be used,
- For surfaces with small slopes and a medium or small standard deviation of surface heights, the *scalar approximation* is used.

In the *scalar approximation* of Kirchhoff's model, the total backscatter σ_{pp} is given by

$$\sigma_{pp} = \sigma_{ppc} + \sigma_{ppn} + \sigma_{pps} \tag{2.35}$$

where σ_{ppc} is the coherent backscatter, σ_{ppn} is the non-coherent backscatter and σ_{pps} is the scattering due to the surface slopes.

The coherent backscatter σ_{ppc} is given by the Fresnel power reflection coefficient. This term contributes to the total backscatter only if the surface is smooth and

the viewing geometry results in near-normal incidence angles. Since this is rarely the case, this term is usually ignored.

The non-coherent backscatter which is important at all angles, is given by

$$\sigma_{ppn} = (|R_{pp}|kl\cos\theta)^2 e^{-K_0} \sum_{n=1}^{\infty} \frac{K_0^n}{n!n} \exp\left[-\frac{(kl\sin\theta)^2}{n}\right] \tag{2.36}$$

The scattering due to surface slopes is given by

$$\begin{aligned}\sigma_{pps} &= 8\sin\theta(k^2\sigma l\cos\theta)^2 e^{-K_0}\left[|R_{pp}|^2\sin\theta + \Re\{R_{pp}R_{pp1}^*\}\cos\theta\right] \\ &\quad \times \sum_{n=1}^{\infty} \frac{K_0^{n-1}}{n!n} \exp\left[-\frac{(kl\sin\theta)^2}{n}\right]\end{aligned} \tag{2.37}$$

where

$$K_0 = 4k^2\sigma^2\cos^2\theta$$

and

k = wave number of transmitted signal,
l = correlation length of the surface,
σ = standard deviation of the surface height,
θ = incidence angle,
R_{pp} = $R_{\perp 0}$ or $R_{\|0}$ depending on the choice of polarization,
R_{pp1} = $R_{\perp 1}$ or $R_{\|1}$ depending on the choice of polarization,
R_{pp1}^* = complex conjugate of R_{pp1}.

Expressions for R_{pp} and R_{pp1} are obtained by applying the Taylor series expansion to $R_\perp$ or $R_\|$ with respect to the surface slopes along the x- and y-directions. Explicit forms of R_{pp} and R_{pp1} are given in Ulaby [98, p1002].

From equations 2.36 and 2.37 it can be seen that the Kirchhoff model approaches the Fresnel power reflectivity model when $k\sigma$ approaches zero.

A complete theoretical treatment of Kirchhoff's model is contained in Ulaby [98, p925].

The Small Perturbation Model

When a rough surface has a standard deviation much less than the incident wavelength (5% or less) and an average surface slope less than the surface standard deviation times the wave number, the small perturbation model is used. Mathematically, the conditions are expressed as

$$k\sigma < 0.3 \tag{2.38}$$

$$\sqrt{2}\sigma/l < 0.3 \tag{2.39}$$

where k is the wave number of the transmitted signal. The correlation length l and standard deviation σ is defined in section 2.3.2.

The first-order bistatic scattering coefficient for either a horizontally or vertically polarized incident wave is given by [98, p961]

$$\sigma_{pq} = 8k^4\sigma^2\cos^4\theta\,|\alpha_{pq}|^2 W(2k\sin\theta) \tag{2.40}$$

where

$$\begin{aligned}
\alpha_{hh} &= R_{\perp} \\
\alpha_{vv} &= (\varepsilon_r - 1)\frac{\sin^2\theta - \varepsilon_r(1+\sin^2\theta)}{\left[\varepsilon_r\cos\theta + (\varepsilon_r - \sin^2\theta)^{1/2}\right]^2} \\
\alpha_{hv} &= \alpha_{vh} = 0
\end{aligned}$$

and $W(2k\sin\theta)$ is the Fourier transform of the surface correlation coefficient, also known as the roughness spectrum. Thus, the first-order backscatter from a slightly rough surface depends on a particular frequency component of the surface roughness spectrum.

Generally, the small perturbation model assumes that the surface roughness has a Gaussian surface correlation function $\rho(\zeta)$ where

$$\rho(\zeta) = \exp\left(-\frac{\zeta^2}{l^2}\right) \tag{2.41}$$

which means that the roughness spectrum is give by

$$W(2k\sin\theta) = \frac{1}{2}\, l^2 \exp\left[-(kl\sin\theta)^2\right]. \tag{2.42}$$

However, Oh [71] showed empirically that $\rho(\zeta)$ is better approximated by an exponential rather than a gaussian surface correlation function. An exponential surface correlation function $\rho(\zeta)$ is given by

$$\rho(\zeta) = \exp\left(-\frac{|\zeta|}{l}\right) \tag{2.43}$$

and the roughness spectrum is given by

$$W(2k\sin\theta) = \frac{1}{2}\, l^2\left[1 + (2kl\sin\theta)^2\right]^{-1}. \tag{2.44}$$

A complete theoretical treatment of small perturbation model is contained in Ulaby [98, p949]. Engman [30] showed empirically that the small perturbation model worked best for radar backscatter measured at L-band frequencies.

The Geometric Optics Model

The geometric optics model is applied to relatively rough surfaces whose backscatter coefficient is relatively constant for small incidence angles.

This model is valid for the following conditions,

$$(2k\sigma\cos\theta)^2 > 10 \tag{2.45}$$

$$kl > 6 \tag{2.46}$$

$$l^2 > 2.76\sigma\lambda \tag{2.47}$$

which limits the use of this model to short wavelengths.

This model has the form

$$\sigma_{HH} = \left[\frac{|R_\perp(\theta)|^2}{2m^2\cos^4\theta}\right] \times \exp\left(\frac{-\tan^2\theta}{2m^2}\right) \tag{2.48}$$

where $R_\perp(0)$ is the reflectivity at $\theta = 0$ and m is the RMS surface slope. For a surface with an exponential correlation function,

$$m = \frac{\sigma}{l} \tag{2.49}$$

and a Gaussian correlation function,

$$m = \frac{\sqrt{2}\sigma}{l}. \tag{2.50}$$

This model does not produce good agreement with backscatter measurements [30] [98], and hence is not discussed any further.

Bragg Resonance

Bragg resonance is a theory that accounts for relatively high backscatter at large incidence angles (greater that 30°). In this theory, the backscatter arises primarily from resonant components in the roughness spectrum, even though the energy in the resonant-frequency range is quite small compared with the total energy. Bragg scattering occurs when the illuminated surface has a periodic structure. To simplify the theory, assume that the surface is sinusoidal, with a wavelength L that is being illuminated at an angle θ. Bragg resonance will occur if

$$\frac{2L}{\lambda} \sin\theta = n, \quad n = 1, 2, ... \tag{2.51}$$

where λ is the wavelength of the transmitted signal.

Theoretical scattering models at radar frequencies

The behaviour of scattering models at radar frequencies was investigated by Engman [30] and Oh [71]. They found that at radar frequencies, the validity conditions of the models become very restrictive. A graph of the validity conditions of the Small Perturbation (SPM), Physical Optics (PO) and Geometric Optics (GO) models for random surfaces characterized by a Gaussian autocorrelation function is shown in figure 2.4. The validity condition of the GO model (being incidence angle dependent) assumed $\theta = 40°$. Also plotted on the graph is the radar roughness of four surfaces at L-, C- and X-band. The subscripts numbered 1 to 4 corresponds to surface standard deviations of $s = 0.4$ cm, $s = 0.32$ cm, $s = 1.12$ cm and $s = 3.02$ cm respectively. Figure 2.4 shows that the expected surface roughness and radar frequency determines which scattering model can be used.

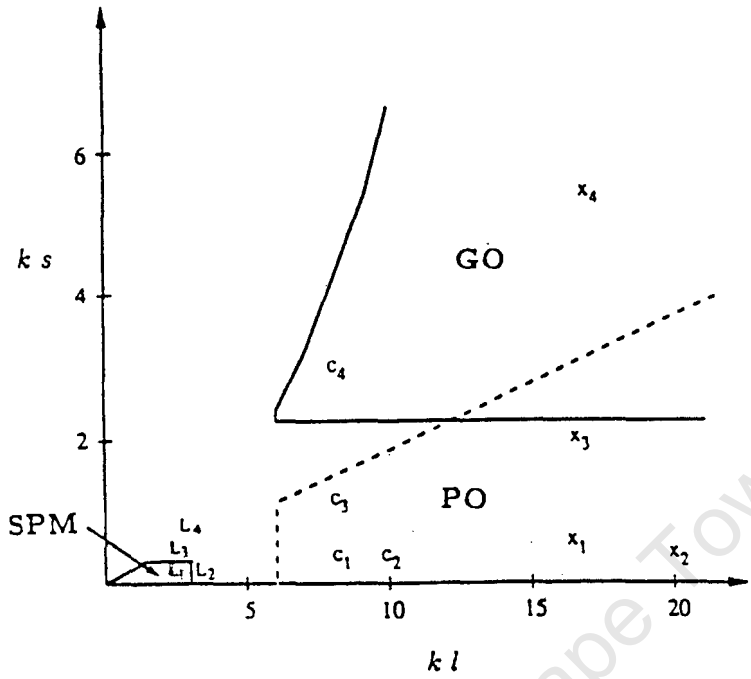

Figure 2.4: Region of validity of the Small Perturbation (SPM), Physical Optics (PO) and Geometric Optics (GO) models. (Oh [71, p374])

Empirically, the standard deviation of the surface heights appears to be a good measure of the surface roughness conditions. However, the surface correlation length does not appear to be related to the measured backscatter [30]. Oh [71] derived semi-empirical models which in his opinion is more consistent with measured backscatter than the classical models.

Empirical scattering models

Theoretical model prediction of radar backscatter has only recently become popular. Previously, only empirical models were used. In addition, the complexity of the theoretical models has resulted in many uses preferring empirical models.

In empirical models the surface is described using common language terms such as "Soil and Rock" rather than mathematical terms such as surface correlation length l, surface standard deviation σ and surface permittivity ε. Thus, a very

large data base is required to include the many possible surface types which can range from rocks, soils to vegetated surfaces. Ulaby [95] compiled a data base of radar backscatter as a function of incidence angle for numerous surfaces, discrete frequencies (L-, S-, C-, X-, Ku-, Ka-, W-band) and common polarizations (HH,VV,HV). To this data he fitted a function of the form shown in Equation 2.52 which is based on the apparent exponential relationship as well as the classical (Lambertian) cosine function.

In Ulaby's [95] data base the terrain is initially subdivided into four major categories: barren and sparsely vegetated land, vegetated land, urban land, and snow-covered land. The barren and sparsely vegetated category is subdivided into exposed rock and stony soils like desert pavements, gravels and soils typical of arid environments. This category also includes non-vegetated (or bare) soil surfaces of agricultural lands which is further subdivided into smooth, medium rough and rough surfaces. The vegetated land category includes both naturally occurring vegetation and agricultural crops which are subdivided into four units on the basis of canopy structure and substrate conditions: trees, shrubs, grasses, and wetlands.

Ulaby's empirical model provides for each terrain (or surface) category a set of 21 (7 frequencies $\times$ 3 polarizations) statistical distribution tables organised by frequency band, polarization configuration and incidence angle. At each incidence angle for which data is available, the following information is provided in a statistical distribution table :

- The number of σ^0 data points available in the data base.
- The maximum, median and minimum values of the σ^0 distribution.
- The mean and standard deviation of the σ^0 distribution.

For each category, frequency band, and polarization, the angular behaviour of the mean σ^0 is determined by an iterative least-square and non-linear curve-fitting routine. The function relating mean σ^0 to incidence angle is given by:

$$\sigma^0_{mean} = P_1 + P_2 \exp(-P_3\theta) + P_4 \cos(P_5\theta + P_6) \tag{2.52}$$

Such models are easy to use but have limited accuracy since the surface properties (permittivity and roughness) are not well defined. Although the permittivity (real part) of most rocks is relatively constant at approximately 7, the permittivity of soil varies greatly depending on the soil moisture content which results in modelling errors. Usually, empirical models are derived using image "tie" points. The tie point method uses the surface cover and local incidence angle associated

with several pixels in the image to derive a function relating measured backscatter (pixel value) to local incidence angle. This method works well when the surface cover is homogeneous as in images of forest canopies [45].

Chapter 3

The complex dielectric constants of Soil

In this chapter the results of an investigation into the complex dielectric constant (real ε' and imaginary ε'' part) of soil is discussed. A knowledge of the complex dielectric constant of soil is necessary to determine the depth of signal penetration which is important in subsurface radar applications. In addition, the real part of the dielectric constant determines the amount of energy that is absorbed or reflected at the air-soil interface. The study of soil dielectric behaviour is limited to radar frequencies from 1 MHz to 18 GHz.

This chapter starts with a brief discussion of methods used to measure the dielectric constant. Next, the factors (moisture, frequency, soil type, temperature, salinity and density) which determine the dielectric constant of soil are discussed. The chapter ends with a discussion of dielectric models.

3.1 Dielectric constant measurement techniques

This section is a summary of methods used to measure the dielectric constant of soil and has been included to show the reader that measuring the dielectric constant is relatively difficult, hence the need to predict the dielectric constant from parameters which are easier to measure.

3.1.1 Waveguide Transmission Technique

This method was used by Hallikainen [48] and is suitable for frequencies up to 6 GHz at which point the waveguides become small making sample preparation difficult. The dielectric constant is indirectly obtained by measuring the

amplitude $|T_m|$, and phase ϕ_m of the TE_{10} mode transmission coefficient. Theoretically, the transmission coefficient is determine by the waveguide dimensions, the free-space wavelength and the relative complex dielectric constant. Thus, the relative complex dielectric constant can be calculated when the other parameters are known. Since the complex dielectric constant ε consists of a real part ε' and imaginary part ε'', an iterative procedure is used.

3.1.2 Free-Space Transmission Technique

This method was used by Hallikainen [48] to measure the dielectric constant of the soil above 4 GHz. The method is basically similar to the waveguide system except that the dielectric-filled waveguide is replaced by two horn antennas placed above and below the soil sample. The theory used for the waveguide transmission technique is modified for the free-space transmission technique by making the dimensions of the "waveguide" infinite. Again, an iterative procedure is used to obtain the complex dielectric constant.

3.1.3 Time Domain Reflectometry

Time domain reflectometry (TDR) is a popular method for measuring dielectric constant of soils (Hoekstra [50], Topp [89, 90] and references therein). In TDR, the soil sample is packed in a coaxial line approximately 20 cm long. Great care should be taken when placing the sample in the coaxial line since variations in the density will cause unwanted reflections. The method uses a fast rising voltage pulse which propagates through the coaxial line. At the discontinuity, the location where the soil sample causes the characteristic impedance of the coaxial line to change, the voltage pulse will be partially reflected. The voltage pulse will also reflect from the end of the coaxial line which is terminated in an open or short circuit. Hoekstra [50] uses the first reflected pulse whereas Topp [89] uses the reflection of the coaxial line termination.

An outline of Hoekstra's [50] method is given below. For a coaxial line filled with a dielectric, the characteristic impedance Z is a function of the characteristic impedance of an air-filled line Z_0 and the complex dielectric constant ε.

$$Z = Z_0/\sqrt{\varepsilon(\omega)} \tag{3.1}$$

$$Z_0 = 60\ln(b/a) \tag{3.2}$$

Where a and b are the radii of the inner and outer conductors, respectively, of the coaxial transmission line used.

At the discontinuity where the impedance changes from Z to Z_0, the resulting reflection coefficient ρ is given by

$$\rho(\omega) = (Z(\omega) - Z_0)/(Z(\omega) + Z_0) \tag{3.3}$$

Combining equation 3.1 and 3.3 and changing the subject of the formula gives

$$\varepsilon(\omega) = (1 + \rho(\omega))^2/(1 - \rho(\omega))^2 \tag{3.4}$$

For a dielectric sample, Z and ρ will be complex frequency-dependent quantities, and their frequency dependence will show in the differences between the time domain pulse shapes of the incident and reflected signals. The behaviour of the sample in the frequency domain can be found by calculating the ratio of the Fourier transform of the incident and reflected pulses. Thus $\rho(\omega)$, the complex reflection coefficient of the air-sample interface in the frequency domain, is related to the incident $f_i(t)$ and reflected $f_r(t)$ pulses in the time domain by

$$\rho(\omega) = \frac{\int_{-\infty}^{\infty} f_r(t) \exp(-j\omega t)\, dt}{\int_{-\infty}^{\infty} f_i(t) \exp(-j\omega t)\, dt}. \tag{3.5}$$

The complex dielectric constant can thus be determined at an air-sample interface.

Next, an outline of Topp's [89] method is given below. The soil sample is placed in a coaxial line of known length which is terminated on one side with a short circuit or open circuit. The propagation velocity V of an electromagnetic wave in the transmission line is given by

$$V = c/\left(\varepsilon' \frac{1 + (1 + \tan^2\delta)^{\frac{1}{2}}}{2}\right)^{\frac{1}{2}} \tag{3.6}$$

where c is the velocity of an electromagnetic wave in free-space, ε' is the real part of the complex dielectric constant and $\tan\delta$ is the loss tangent. If the loss is very low ($\tan\delta \ll 1$), then

$$V \approx c/(\varepsilon')^{\frac{1}{2}} \tag{3.7}$$

Thus for low-loss materials, ε' can be estimated from a measurement of the propagation velocity V.

3.2 Factors affecting the complex dielectric constant of soils

A knowledge of the soil parameters which affect the complex dielectric constant is needed to formulate a model which would account for the empirically observed effects of soil moisture, soil type, soil temperature, soil water salinity and soil density (or compaction) at all frequencies.

3.2.1 Soil moisture

The complex dielectric constant of soil has been found by many researchers to be highly sensitive to the moisture content of the soil. *In situ* measurements (Berlin [7], Farr [36], McCauley [67]) as well as laboratory measurements (Ansoult [3], Hallikainen [48], Hoekstra [50], Topp [89] and many others) prove empirically that moisture content significantly influences the complex dielectric constant and thus determines radar signal attenuation in soils.

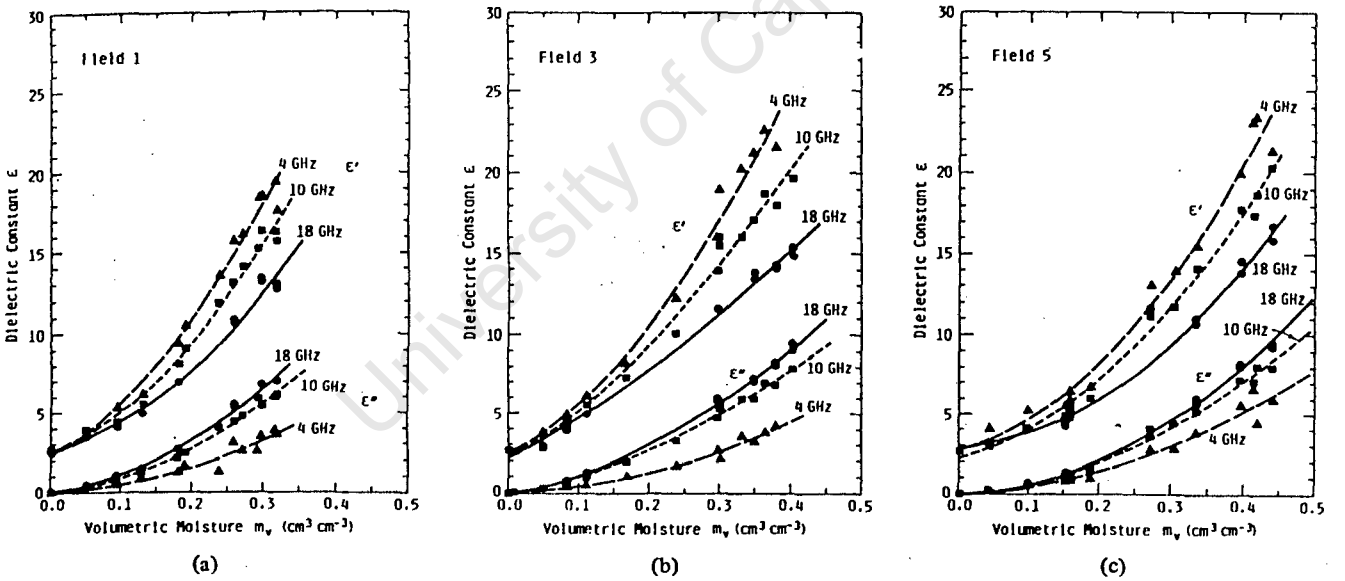

Figure 3.1: Graphs of measured complex dielectric constants as a function of volumetric water content at 4, 10, 18 GHz. Polynomial regression fits are also shown. (Hallikainen [48, p31])

The relative dielectric permittivity ε' of dry soil (sand and/or clay) ranges from 3 to 4, independent of frequency. As water is added, the relative dielectric permittivity increases rapidly as pure water has a value of approximately 80 (for

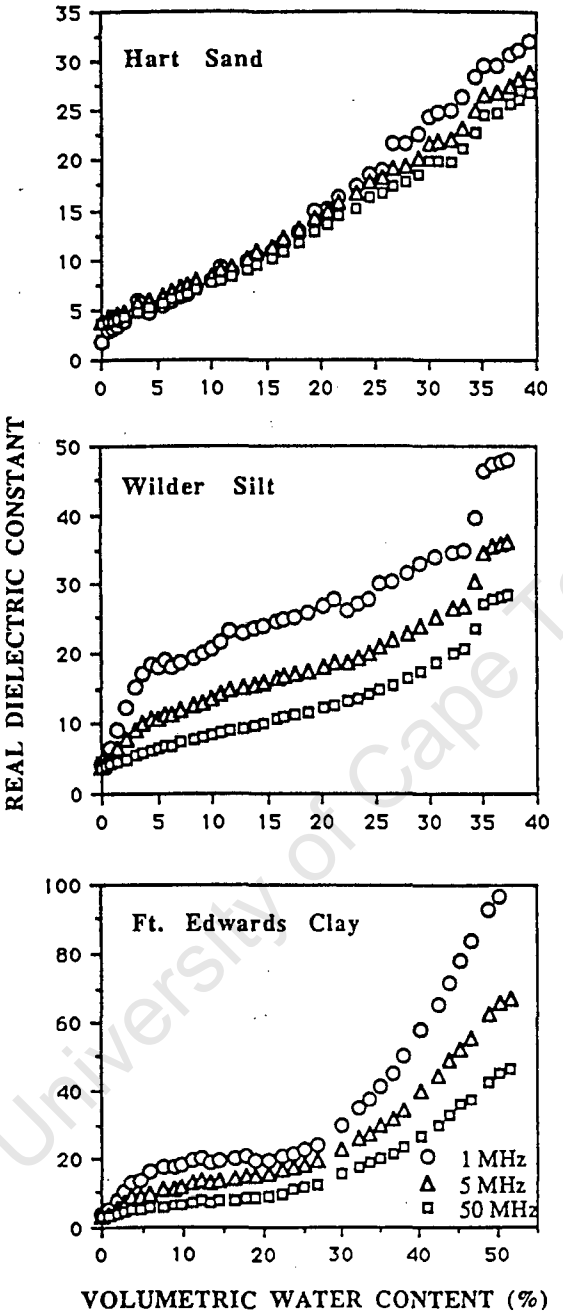

Figure 3.2: Graph of measured complex dielectric constants as a function of volumetric water content at 1, 5, 50 MHz. (Campbell [13, p335])

frequencies below 1 GHz). It is then obvious that the dielectric constant of a soil is greatly influenced by the volumetric water content. Since the dielectric properties of water are so important, an empirical model of the dielectric behaviour of pure water is discussed below.

Permittivity of pure water

The frequency dependence of the dielectric constant of pure water is given by the well-known Debye Equation [98, p2020] :

$$\varepsilon_w = \varepsilon_{w\infty} + \frac{\varepsilon_{w0} - \varepsilon_{w\infty}}{1 + j2\pi f \tau_w} \tag{3.8}$$

where

ε_{w0} = static dielectric constant of pure water, dimensionless
$\varepsilon_{w\infty}$ = high-frequency limit of ε_w, dimensionless
τ_w = *relaxation time* of pure water, seconds
f = electromagnetic frequency, Hz.

The real ε'_w and imaginary ε''_w part of the pure water dielectric constant can be obtained by rationalizing equation 3.8, giving

$$\varepsilon'_w = \varepsilon_{w\infty} + \frac{\varepsilon_{w0} - \varepsilon_{w\infty}}{1 + (2\pi f \tau_w)^2} \tag{3.9}$$

$$\varepsilon''_w = \frac{2\pi f \tau_w (\varepsilon_{w0} - \varepsilon_{w\infty})}{1 + (2\pi f \tau_w)^2} \tag{3.10}$$

The above equations are frequency and temperature dependent. The temperature dependency is implicit in $\varepsilon_{w\infty}$, ε_{w0} and τ_w. Ulaby [98, p2021] contains empirically derived third order polynomials for ε_{w0} and τ_w as functions of water temperature. The temperature dependence of $\varepsilon_{w\infty}$ is so weak that for computational purposes it is assumed to be a constant.

Permittivity of saline water

Saline water is water containing dissolved salts. The salinity of the water can be expressed either as the amount of dissolved salts (in parts per thousand on a weight basis) or ionic conductivity (in Siemens per metre). The frequency

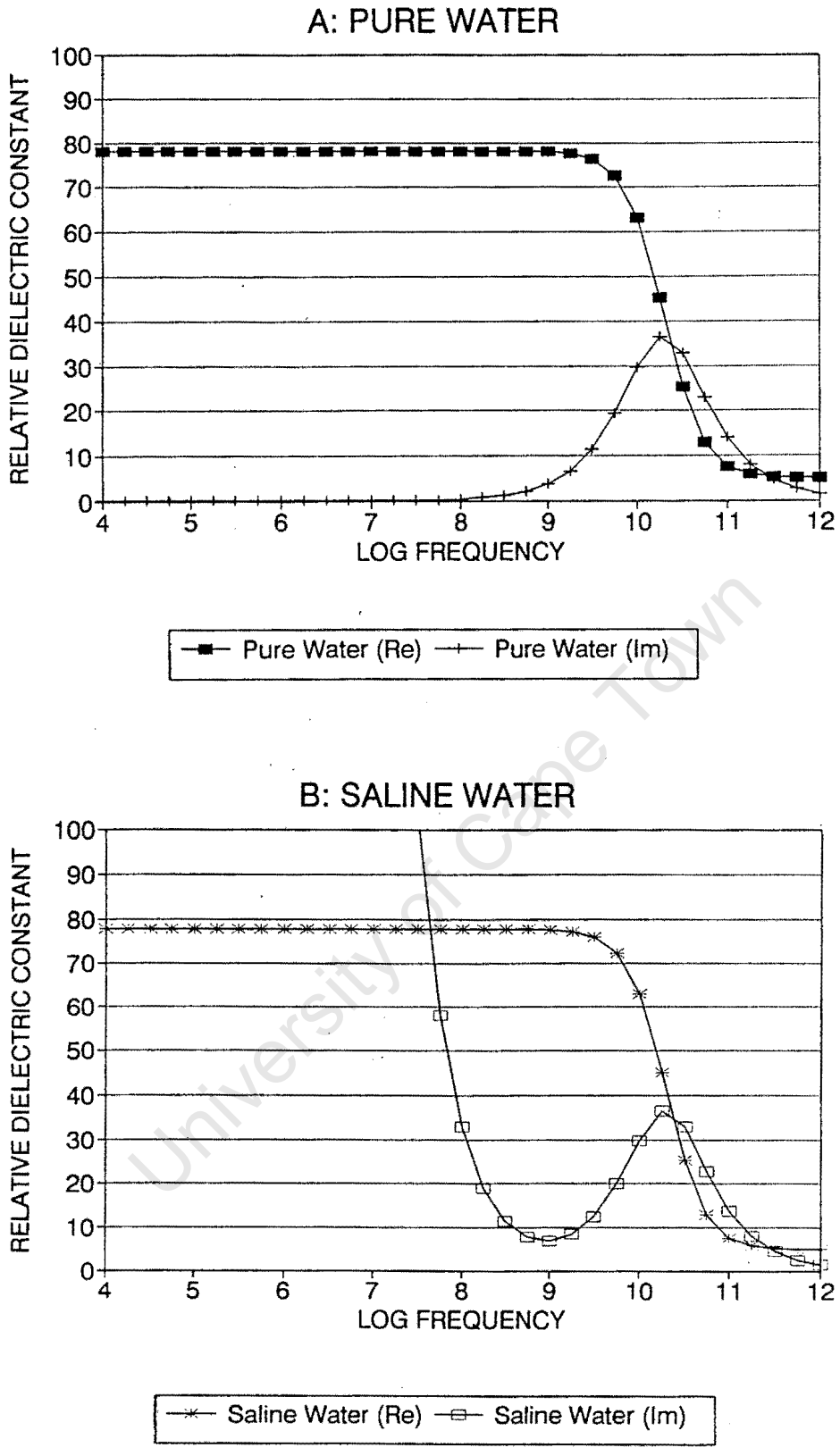

Figure 3.3: Permittivity of pure and saline water as a function of frequency. Note: Conductivity in saline water becomes more prominent at lower frequencies. The dielectric relaxation is clear in both graphs.

dependence of the dielectric constant of saline water is given by the modified Debye Equation [98, p2022]. The real ε'_{sw} and imaginary ε''_{sw} parts of the dielectric constant of a saline water are given by :

$$\varepsilon'_{sw} = \varepsilon_{sw\infty} + \frac{\varepsilon_{sw0} - \varepsilon_{sw\infty}}{1 + (2\pi f \tau_{sw})^2} \tag{3.11}$$

$$\varepsilon''_{sw} = \frac{2\pi f \tau_{sw}(\varepsilon_{sw0} - \varepsilon_{sw\infty})}{1 + (2\pi f \tau_{sw})^2} + \frac{\sigma_i}{2\pi \varepsilon_0 f} \tag{3.12}$$

where

ε_{sw0} = static dielectric constant of saline water, dimensionless
$\varepsilon_{sw\infty}$ = high-frequency limit of ε_w, dimensionless
τ_{sw} = *relaxation time* of saline water, seconds
σ_i = ionic conductivity of saline solution, S/m
ε_0 = permittivity of free space; $\varepsilon_0 = 8.854 \times 10^{-12}$ F/m
f = electromagnetic frequency, Hz.

As in the pure water case, ε_{sw0} and τ_{sw} can be calculated using expressions [98, p2024] which are functions of water salinity and temperature. It should be noted that ionic conductivity affects the imaginary part and *not* the real part of the complex permittivity.

Equations 3.9, 3.10, 3.11 and 3.12 were implemented on MathCAD (see Appendix D) resulting in Figure 3.3 which demonstrates the frequency dependence of the dielectric constant of pure and saline water.

Soil exhibits water dielectric properties

Returning to the subject of soil permittivity, Hoekstra [50] noticed the similarity between soil and bulk water dielectric behaviour in the microwave region. He modified the *Debye Equation* (3.8) in an attempt to explain his experimental findings. His data showed (see Figure 3.4) that soil also exhibits dielectric relaxation, but that the relaxation frequency of soils was lower than that of bulk water. The dielectric constant ε' decreases with increasing frequency and the dielectric loss factor ε'' also goes through a maximum. The frequency at which this maximum occurs is by definition the relaxation frequency. He attributed the observed dielectric behaviour to the presence of water in soils.

De Loor [63] contains a summary of the mechanisms which influence the dielectrics of a heterogeneous system containing water. At microwave frequencies,

soil. For a known volume V of the sample holder, $\rho_b = W_d/V$.

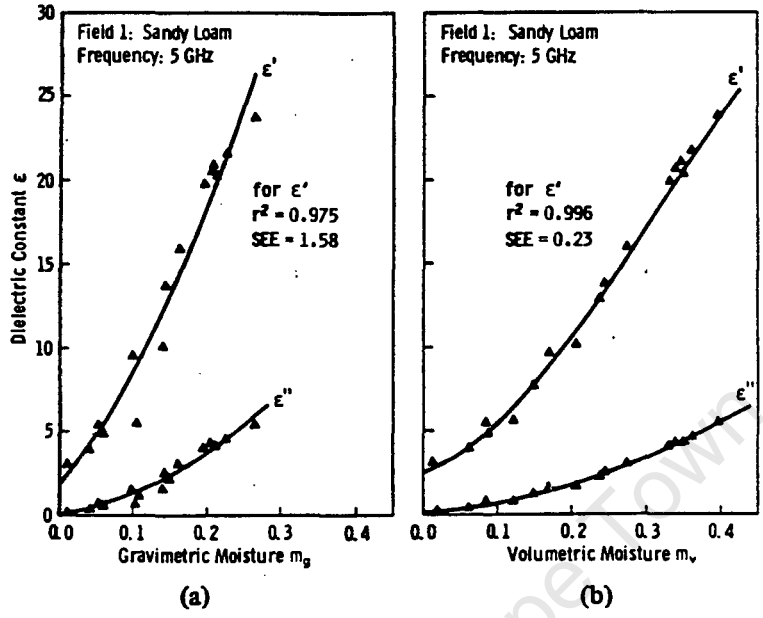

Figure 3.5: A comparison of soil dielectric constants plotted as a function of (a) gravimetric moisture and (b) volumetric moisture content. (Ulaby [98, p2090])

Electromagnetically, the volumetric measure is a better indication of the moisture content of the soil-water mixture. This preference is evident in the plots shown in Figure 3.5, in which a greater degree of scattering about the regression curve is apparent for plots of ε' and ε'' versus m_g, than for those plotted versus m_v.

3.2.2 Soil type

The complex dielectric constants ε' and ε'' are dependent on soil textural composition [13] [19] [48] [89] [106]. A definition of Soil Type / Soil Textural Composition is contained in Appendix A.

Wang [106] found that when water was added to dry soil, the dielectric constant initially increased slowly. Upon reaching a transition moisture value, the dielectric constant increased rapidly with moisture content. Wang also found that this transition moisture value varies with soil type or texture, being lower for sandy soils than for high-clay content soils. Wang attributed this effect to *bound* water which is determined by the soil-particle size distribution. Wang's view is supported by Dobson [19, 22] who suggests that the *bound* water surrounding the surface of a soil particle is unaffected by the microwave field and hence is characterized by a relatively low dielectric constant, which is higher than ice but lower

than pure water. He deduced that bound water exhibits a dielectric relaxation at a frequency lower than pure water.

Figure 3.6 depicts the variation of dielectric constants ε' and ε'' with volumetric moisture content m_v for five soil types at 1.4, 5, 10 and 18 GHz. At each frequency, all the curves for ε' and ε'' have approximately the same intercept at $m_v = 0$ and exhibit the same general shape but have different curvatures for different soil types. The different curvatures for different soil types can be explained by Wang's *bound* water hypothesis.

Hallikainen's [48] research shows that at any given moisture content and at microwave frequencies, ε' was found to be roughly proportional to sand content and inversely proportional to clay content. This relationship between ε' and soil texture occurred at all frequencies from 1.4 GHz to 18 GHz, however the magnitude of the effect was found to decrease with an increase in frequency. The behaviour of ε'' does not exhibit a simple dependency on soil textural components. This is caused by ionic conductivity which affects ε'' at frequencies less than 5 GHz. The affects of conductivity are discussed in section 3.2.4.

Topp [89] observed a weak soil type dependence of ε' in the frequency range 1 MHz to 1 GHz. He found that graphs of ε' versus m_v showed greater curvature for high-clay content soils than sandy soils. Topp attributed this phenomenon to the *bound* water hypothesis.

Campbell [13] researched the behaviour of ε' and ε'' in the frequency range 1 MHz to 50 MHz. The soil dependency is clearly visible in Figure 3.7. However, Campbell found that at these low frequencies, *bound* water cannot account for his findings. Instead, he used a complex dielectric constant model based on Looyenga's Equation to show that ionic conductivity dominates over the frequency range 1 to 50 MHz. The affects of conductivity are discussed in section 3.2.4.

3.2.3 Soil temperature

The dielectric properties of soil both real and imaginary show a clear but weak dependence on soil temperature. This is evident in graphs by Campbell [13] and Hallikainen [48].

At microwave frequencies, both ε' and ε'' increase with increasing temperature as can be seen in Figure 3.8. Hallikainen also studied the effects of temperatures below 0°C and observed the rapid drop expected from both ε' and ε'' since ice ($\varepsilon_{ice} = 3.15 - \jmath 0$) has a relatively low dielectric constant.

At frequencies between 1 MHz and 1 GHz, Topp [89] increased the temperature from 10°C to 36°C and was unable to detect a variation in ε' greater than the experimental error.

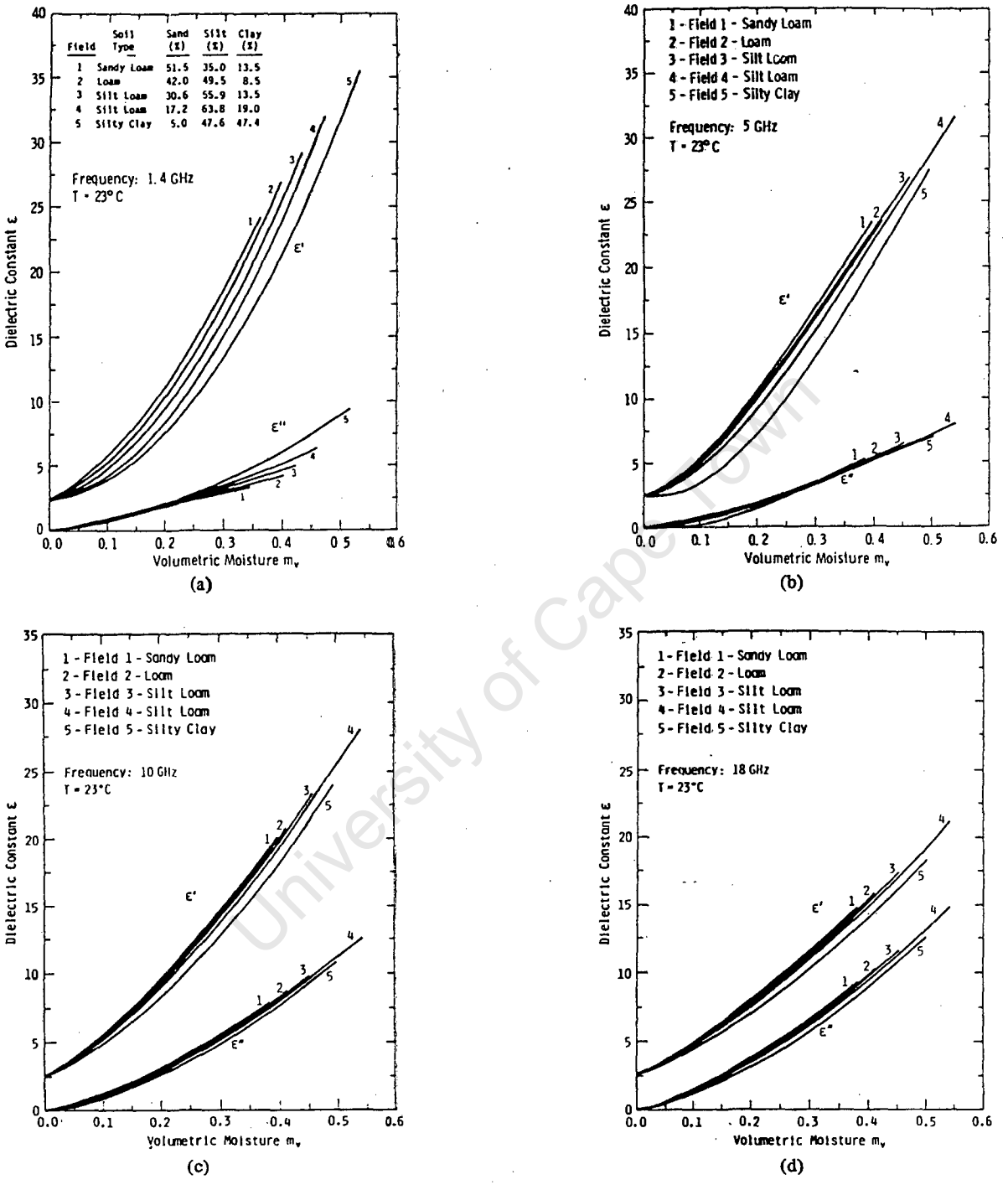

Figure 3.6: The real and imaginary dielectric constants for five soils at (a) 1.4 GHz, (b) 5 GHz, (c) 10 GHz, and (d) 18 GHz. (Hallikainen [48, p30])

At radio frequencies (1 to 50 MHz), the behaviour is more complicated as can be seen in Figure 3.9. Campbell used Manchester silt with a volumetric moisture content of 34.2% to observe the temperature effects from 0°C to 85°C. At 1 MHz, ε' at 0.5°C is 34.8 which increased to 42.0 at 84.5°C. At 2 MHz, very little temperature dependence is observed. At higher frequencies, ε' decreases with increasing temperature. For the radio frequencies observed, ε'' increased uniformly with temperature.

3.2.4 Soil Salinity

The salinity of soil exhibits the same effect as bulk saline water (discussed in Section 3.2.1). Saline water is water containing dissolved salts resulting in ionic conductivity which becomes dominant at lower frequencies. The salinity of soil water is usually expressed in Siemens per metre (S m^{-1}).

The real part of the complex dielectric constant of bulk water is unaffected by salt content. This is evident when comparing graphs of pure water and saline water (see Figure 3.3). Likewise, the real part of the complex dielectric constant of soil ε' is also unaffected by the salinity of the soil between 1 MHz and 1 GHz. Topp's [89] research, shown in Figure 3.10, proves that the presence of salt, NaCl and $CaSO_4$ in the liquid phase of the soil-water caused no measurable effect on ε'.

At frequencies below 5 GHz, the imaginary part of the complex dielectric constant of bulk saline water and soil is mainly controlled by the ionic conductivity of the water and soil water respectively. Topp [89] observed that the presence of salt in the soil water caused greater signal attenuation which is indicative of greater ε'' values since ε' is unaffected by salinity.

3.2.5 Soil compaction

Dry soil (sand and clay) has a relative dielectric constant ε' that is dominantly controlled by bulk density, ranging from 3 to 4 (independent of frequency) [72]. Once water is added to the dry soil, the permittivity of the water dominates and thus, the effects of density on soil dielectric properties are largely accounted for by expressing soil moisture on a volumetric basis.

3.3 Dielectric Models

In radar applications the electrical behaviour of soils is inferred from the complex dielectric constant of the soil medium. Thus, a simple method for predicting the

complex dielectric constant of soil is needed. The literature on dielectric models can generally be divided into two groups namely theoretical and empirical models.

3.3.1 Theoretical models

The theory on which theoretical dielectric models are based is complex and in spite of the research efforts of the last two decades is still not well understood. These models incorporate the physics and chemistry of the soil particles and soil-water mixtures. The permittivity literature contains numerous theoretical models [8] [63] [22] [50] [76] [82] [83] [106] [108], but very few of these models are truly applicable to the soil medium of interest or the intended radar application. The model by Sen [82] is intended for sedimentary rocks such as sandstone, but has been shown to work for water saturated sands such as marine sands [52]. The two component models such as that proposed by Birchak [8] is unrealistic because it ignores the air voids, bound water and ionic conductivity common in soils. The double relaxation frequency model of Hoekstra [50], later extended by Wang [104] is also unrealistic because there is no easy way of calculating the two Debye-type relaxation frequencies.

The best model is a four component model by Dobson [22] which incorporates many of the classic models and theories. The dielectric behaviour of the soil is described by the mixing of four components namely dry soil, bound water in the Stern layer, bulk water in the Gouy layers and air. The model is based on De Loor's formula [63, p364]

$$\varepsilon_m = \varepsilon_s + \sum_{i=1}^{3} \frac{V_i}{3}(\varepsilon_i - \varepsilon_s) \sum_{j=1}^{3} \frac{1}{1 + \left(\frac{\varepsilon_i}{\varepsilon^*} - 1\right) A_j} \tag{3.13}$$

where

ε_s = relative permittivity of soil solid,
ε_i = relative permittivity of the inclusions (air, bound water and free water),
ε^* = effective relative permittivity near the boundaries,
A_j = depolarization ellipsoid factors, and
V_i = volume fractions of the inclusions.

The value of ε^* has a potential range of $\varepsilon_s \leq \varepsilon^* \leq \varepsilon_m$, and is usually assumed to be equal to ε_s or ε_m. The dominant composition of the soil determines the value of A_j. For disc shaped inclusions like clay, $A_j = (0; 0; 1)$ and spherical inclusions like sand, $A_j = (1/3; 1/3; 1/3)$. Since the value of ε^* is uncertain, De Loor [63]

suggested that Equation 3.13 be used to determine the limits of ε_m. These limits are obtained by substituting in equation 3.13, $A_j = (0;0;1)$ with $\varepsilon^* = \varepsilon_m$, and $A_j = (1/3;1/3;1/3)$ with $\varepsilon^* = \varepsilon_s$. According to De Loor, the results of many commonly used models lie somewhere between these general limits.

Dobson [22] assumed $A_j = (0;0;1)$ and $\varepsilon^* = \varepsilon_m$ with inclusions of bound water, free water and air. Substituting this into equation 3.13 gives

$$\varepsilon_m = \frac{3\varepsilon_s + 2V_{fw}(\varepsilon_{fw} - \varepsilon_s) + 2V_{bw}(\varepsilon_{bw} - \varepsilon_s) + 2V_a(\varepsilon_a - \varepsilon_s)}{3 + V_{fw}(\frac{\varepsilon_s}{\varepsilon_{fw}} - 1)V_{bw}(\frac{\varepsilon_s}{\varepsilon_{bw}} - 1)V_a(\frac{\varepsilon_s}{\varepsilon_a} - 1)} \tag{3.14}$$

where the subscripts *fw*, *bw*, *a* and *s* refer to free Gouy-layer water, bound Stern-layer water, air and dry soil, respectively. The volume fractions V_{fw}, V_{bw} and V_a can be determine when the soil type, water content and bulk density of the soil is known. However, the calculation of volume fractions has very many assumptions and makes this model impractical. The relative permittivities $\varepsilon_a = 1$, and the expression for ε_s is

$$\varepsilon_s = (1.01 + 0.44\rho_s)^2 - 0.062 \tag{3.15}$$

which yields values expected for dry soil. Equation 3.15 is identical in form to a two component refractive model assuming a host medium of air with soil particles as inclusions.

The values of ε'_{fw} and ε''_{fw} are calculated using Equations 3.11 and 3.12 for bulk saline water. Lastly, a value for ε_{bw} is based on the assumption that bound water behaves more like ice than free water. The assumed value of bound water has less effect on sandy soils than high clay content soils.

According to Dobson [22] this model can predict the complex dielectric constant at microwave frequencies but fails at lower frequencies where the ionic conductivity dominates. There are no theoretical models for frequencies 1 MHz to 1 GHz which can account for the ionic conductivity losses.

Although some theoretical models correctly predict the dielectric constants, they are totally impractical. Instead, empirical models can be used since the parameters needed are easier to measure.

3.3.2 Empirical models

The theory presented in previous sections indicate that the most important parameters affecting soil permittivity are soil moisture, soil type and soil water salinity. Empirical models [13] [48] [89] use regression polynomials fitted to empirical data to obtain simple expressions for ε' as functions of soil moisture and

soil type. All empirical models found in the literature ignore the effect of the soil water salinity which limits the frequency range over which the imaginary part of the dielectric permittivity ε'' can be modelled. Thus, only at microwave frequencies, the frequency region where ionic conductivity is negligible can ε'' be modelled.

Frequency : 1 MHz to 50 MHz

The dependence of the real dielectric constant on water content is expressed in third-order polynomials fitted to the 1 MHz and 50 MHz data. The best third order polynomial fit to 1 MHz data gives [13]

$$\varepsilon_r' = 3.52 + 173m_v - 843m_v^2 + 1690m_v^3, \quad r^2 = 0.873 \tag{3.16}$$

and 50 MHz data

$$\varepsilon_r' = 3.27 + 48.8m_v - 121m_v^2 + 369m_v^3, \quad r^2 = 0.943 \tag{3.17}$$

where ε_r' is the real part of the relative dielectric permittivity and m_v is the volumetric water content of the soil. The polynomials were obtained from measurements of six different soils ranging from sand to clays.

The correlation coefficient (r^2) for the 50 MHz data is better than the 1 MHz data value which according to Campbell [13] is indicative of greater soil type dependence at lower frequencies. In spite of the soil type dependency, the third-order polynomials can be used to predict the real dielectric constant.

Frequency : 20 MHz to 1 GHz

The dependence of the real dielectric constant on water content is expressed in a third-order polynomial for four soil types ranging from sandy loam to clay. The expression [89] is

$$\varepsilon_r' = 3.03 + 9.3m_v + 146.0m_v^2 - 76.7m_v^3 \tag{3.18}$$

where ε_r' is the real part of the relative dielectric permittivity and m_v is the volumetric water content of the soil. This empirical relationship is independent of soil type, soil density, soil temperature and soluble salt content (ionic conductivity).

A second-order polynomial [104, p978] which combines the measurements of other researches ([49] [50] and others) at 0.3, 0.5 and 1.4 GHz gives

	Frequency, GHz	$c_c = (a_0 + a_1S + a_2C) + (b_0 + b_1S + b_2C)m_v + (c_0 + c_1S + c_2C)m_v^2$								
		a_0	a_1	a_2	b_0	b_1	b_2	c_0	c_1	c_2
Real Part, ε'	1.4	2.862	-0.012	0.001	3.803	0.462	-0.341	119.006	-0.500	0.633
	4	2.927	-0.012	-0.001	5.505	0.371	0.062	114.826	-0.389	-0.547
	6	1.993	0.002	0.015	38.086	-0.176	-0.633	10.720	1.256	1.522
	8	1.997	0.002	0.018	25.579	-0.017	-0.412	39.793	0.723	0.941
	10	2.502	-0.003	-0.003	10.101	0.221	-0.004	77.482	-0.061	-0.135
	12	2.200	-0.001	0.012	26.473	0.013	-0.523	34.333	0.284	1.062
	14	2.301	0.001	0.009	17.918	0.084	-0.282	50.149	0.012	0.387
	16	2.237	0.002	0.009	15.505	0.076	-0.217	48.260	0.168	0.289
	18	1.912	0.007	0.021	29.123	-0.190	-0.545	6.960	0.822	1.195
	All									
Imaginary Part, ε''	1.4	0.356	-0.003	-0.008	5.507	0.044	-0.002	17.753	-0.313	0.206
	4	0.004	0.001	0.002	0.951	0.005	-0.010	16.759	0.192	0.290
	6	-0.123	0.002	0.003	7.502	-0.058	-0.116	2.942	0.452	0.543
	8	-0.201	0.003	0.003	11.266	-0.085	-0.155	0.194	0.584	0.581
	10	-0.070	0.000	0.001	6.620	0.015	-0.081	21.578	0.293	0.332
	12	-0.142	0.001	0.003	11.868	-0.059	-0.225	7.817	0.570	0.801
	14	-0.096	0.001	0.002	8.583	-0.005	-0.153	28.707	0.297	0.357
	16	-0.027	-0.001	0.003	6.179	0.074	-0.086	34.126	0.143	0.206
	18	-0.071	0.000	0.003	6.938	0.029	-0.128	29.945	0.275	0.377
	All									

Table 3.1: Polynomial coefficients for an empirical model of dielectric constants as a function of soil type and soil moisture. (Hallikainen [48, p29])

$$\varepsilon_r' = 3.14 + 23.83m + 91.58m^2, \quad r^2 = 0.96 \tag{3.19}$$

where ε_r' is the real part of the relative dielectric permittivity and m is the water content of the soil.

Frequency : 1 GHz to 18 GHz

Hallikainen [48] generated polynomial expressions for ε' and ε'' as functions of m_v, S and C, where S and C are the sand and clay textural components of the soil in percent by weight. The coefficients of the polynomials are given in Table 3.1.

The general form of the polynomial is

$$\varepsilon = (a_0 + a_1S + a_2C) + (b_0 + b_1S + b_2C)m_v + (c_0 + c_1S + c_2C)m_v^2 \tag{3.20}$$

3.4 Conclusion

The theory presented in this chapter proves that the dielectric behaviour of soil is determined by the dielectric behaviour of water and that all other parameters,

such as temperature, density, salinity and soil type are secondary functions of water. The major parameters are water content, soil type and salinity, with the other parameters playing a minor role.

Summarizing the literature on ε' models reveal :

- The behaviour of ε' can be successfully modelled from about 1 MHz to 18 GHz.
- Above 1 GHz, ε' is a function of soil moisture and soil type.
- Below 1 GHz, ε' is a function of soil moisture only.
- The models do not include the effects of soil type dependence which emerge at frequencies below 50 MHz and results in modelling errors.

Summarizing the literature on ε'' models reveal :

- The behaviour of ε'' can *not* be successfully modelled from 1 MHz to 18 GHz.
- Above 1 GHz, ε'' is a function of soil moisture and soil type, and can be accurately modelled.
- Below 1 GHz, ε'' is a function of soil moisture and soil salinity. The empirical models found in the literature do not include the effect of the soil water salinity and thus cannot be used.

This chapter has shown that accurate modelling of soil dielectric constants is only partially successful since the imaginary part of the permittivity cannot easily be modelled. Also, several of the input variables required (soil moisture, soil water salinity, soil composition) is difficult to measure. Hence, it may be easier to measure the permittivity directly.

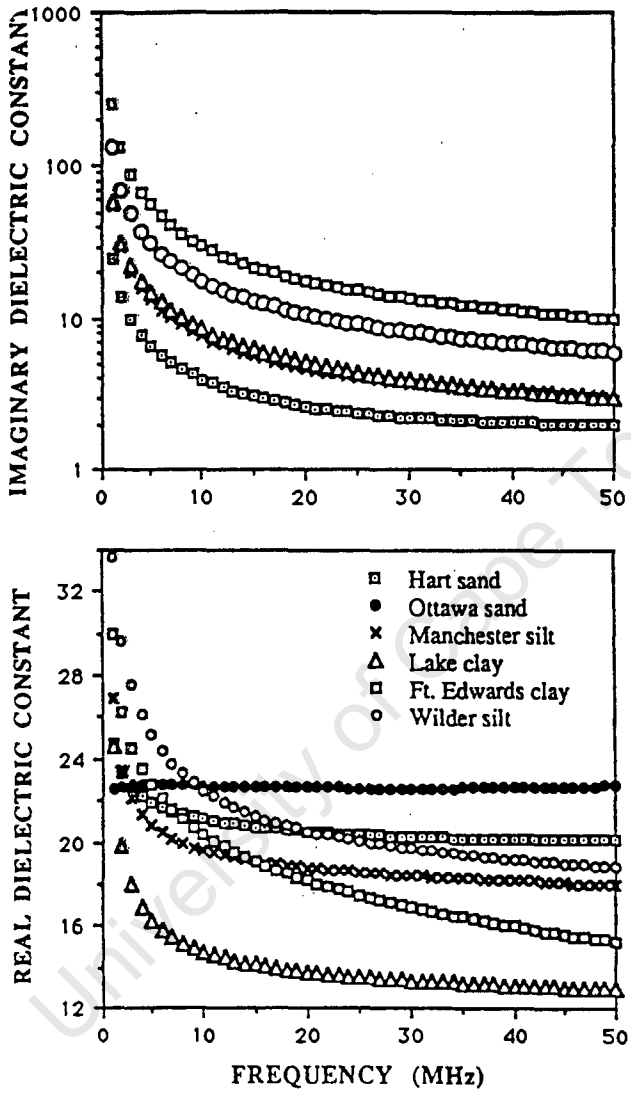

Figure 3.7: The real and imaginary dielectric constant versus frequency for six soils with 30% volumetric water content. (Campbell [13, p337])

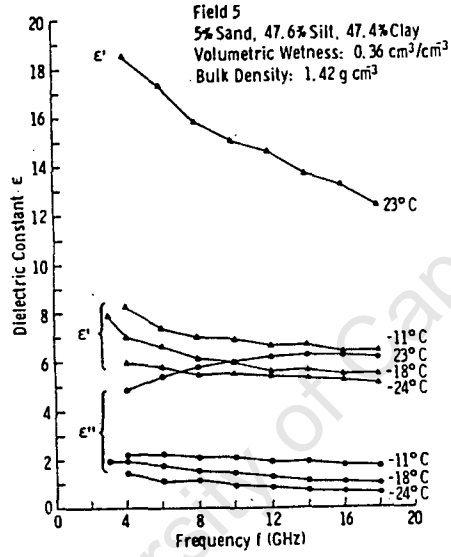

Figure 3.8: The real and imaginary dielectric constants versus frequency with temperatures of 23, -11, -18 and -24°C. (Hallikainen [48, p32])

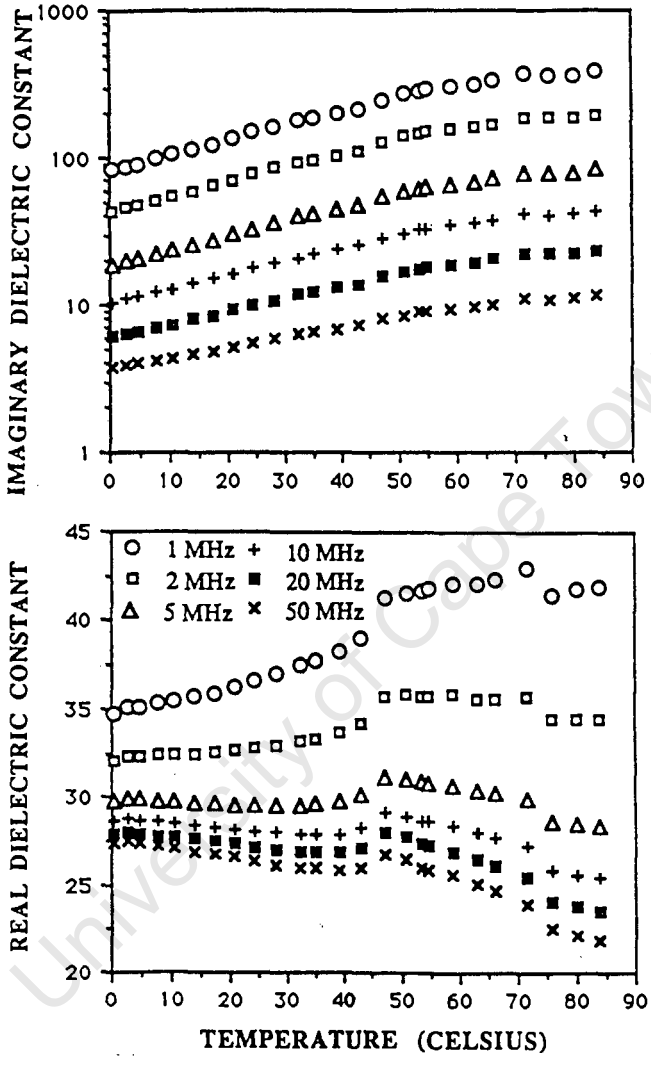

Figure 3.9: Data of the real and imaginary dielectric constants versus temperature at six frequencies with soil water content of 34.2%. (Campbell [13, p338])

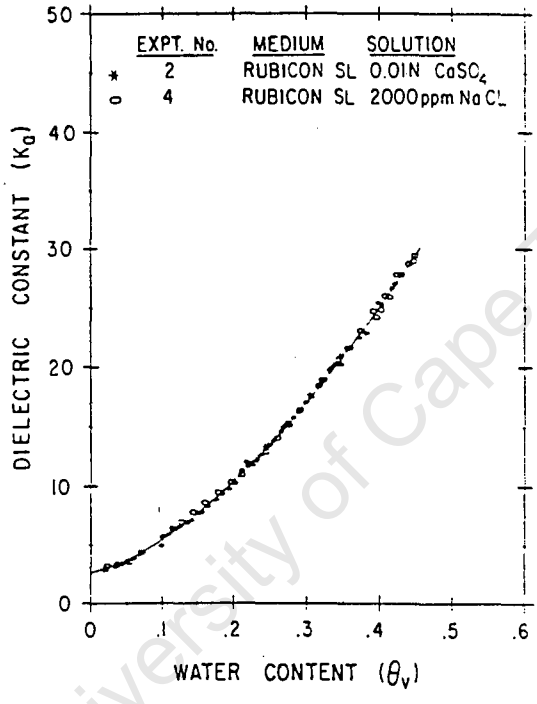

Figure 3.10: Empirical data of the real part of the dielectric constant plotted as a function of volumetric water content at two soil water salinity values. (Topp [89, p580])

Chapter 4

Polarimetry

The international remote sensing community's present interest in polarimetric radar imaging has motivated a special investigation into this relatively new field. This chapter sets out the results of that investigation.

Conventional imaging radars operate with a single, fixed-polarization antenna for both transmission and reception. Hence, a single scattering coefficient is measured, for a specific transmit and receive polarization combination, for each resolution element in the image. This implementation results in the scattered wave, a vector quantity, being measured as a scalar quantity which implies that the additional surface information contained in the vector is lost. In polarimetric radars the backscatter is measured relative to an orthogonal basis which implies that the vector nature of the backscatter response is preserved.

4.1 Definition of polarization

For a uniform plane wave travelling in the z-direction, the electric field vector E must lie in the xy-plane perpendicular to the z-axis. At any fixed point in space the electric field vector is a function of time. As time changes, the tip of the E vector traces a curve in the xy-plane. The most general form of this curve is an elliptical locus, called the *polarization ellipse*. Linear polarization and circular polarization are special cases of an ellipse with extreme eccentricity ($e = 1$) and no eccentricity ($e = 0$), respectively.

In the case of circular or elliptical polarization, the locus of the electric field tip may rotate either clockwise or counterclockwise. In accordance with the IEEE standard the polarization of a wave receding from an observer is denoted right-handed if the electric field vector appears to be rotating clockwise and left-handed if it appears to be rotating counterclockwise [103]. To distinguish between the

two, the wave is right-hand polarized when the right-hand thumb points in the direction of propagation while the other fingers point in the direction of the tip motion [98, p68]. Similarly, the description can be extended to a left-hand polarized wave.

4.2 The polarization ellipse

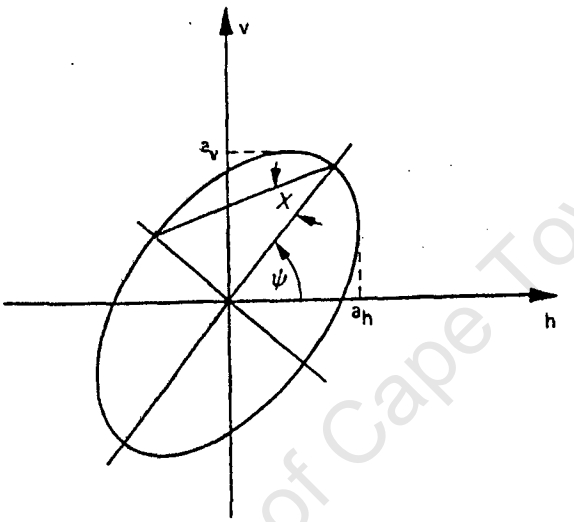

Figure 4.1: Polarization ellipse in the VH plane. (Van Zyl [103, p531])

The polarization properties of the a wave can be defined by the shape and orientation of the polarization ellipse which is completely described by two geometrical parameters namely, the *ellipticity angle* χ and the *ellipse orientation angle* ψ illustrated in Figure 4.1. The handedness of the polarization is indicated by the sign of the ellipticity angle, with negative values indicating right-handed polarizations. The ellipticity angle χ and ellipse orientation angle ψ for the special cases of horizontal, vertical and circular polarizations are given in Table 4.1. Also notice that values of χ between -45° and +45° and values of ψ between 0° and 180° are sufficient to represent all possible polarizations. The semimajor axis of the ellipse is proportional to the amplitude of the wave represented by the ellipse.

The polarization of a wave can also be displayed by mapping the polarization ellipse onto the Poincare sphere (Figure 4.2). An elliptical polarization with an ellipticity angle χ and orientation angle ψ can be uniquely identified with a point having longitude 2ψ and latitude 2χ on the sphere. The equator of the Poincare sphere thus represents linear polarization, the poles represent circular polarization, and the northern hemisphere represents left-handed polarization.

Table 4.1: The ellipticity and orientation angles for common polarizations. Note that horizontal and vertical polarizations are special cases of linear polarization differing only in orientation angle. In the case of circular polarization, the orientation angle has no meaning.

Polarization	Ellipticity χ	Orientation ψ
linear	0°	-
horizontal	0°	0° or 180°
vertical	0°	90°
circular	45°	-
right-handed	negative	-
left-handed	positive	-

A point on the poincare sphere can also be expressed in cartesian co-ordinates with the origin at the centre of the sphere. These co-ordinates are referred to as the Stokes parameters which in terms of the ellipticity χ and orientation ψ angles are expressed as [96, p11]

$$Q = I_0 \cos(2\psi)\cos(2\chi) \quad (4.1)$$
$$U = I_0 \sin(2\psi)\cos(2\chi) \quad (4.2)$$
$$V = I_0 \sin(2\chi) \quad (4.3)$$

where I_0 is the radius of the Poincare sphere and is proportional to the total power in the wave.

4.3 Polarization signatures

The radar polarization signature of an object permits better inferences of the physical scattering process than single polarization measurements through identification and characterization of the dominant scattering mechanism. The polarization signature of a scatterer is the radar cross section (or backscatter) of that scatterer at all possible combinations of transmit and receive polarizations. A note of caution: The word *signature* implies uniqueness, but the polarization response is not unique, as will be shown later in this chapter. This has led to the use of the term *polarization response* in preference to *polarization signature* [96].

A radar system capable of transmitting and receiving any arbitrary polarization is not feasible since the hardware must be modified for each observation [113].

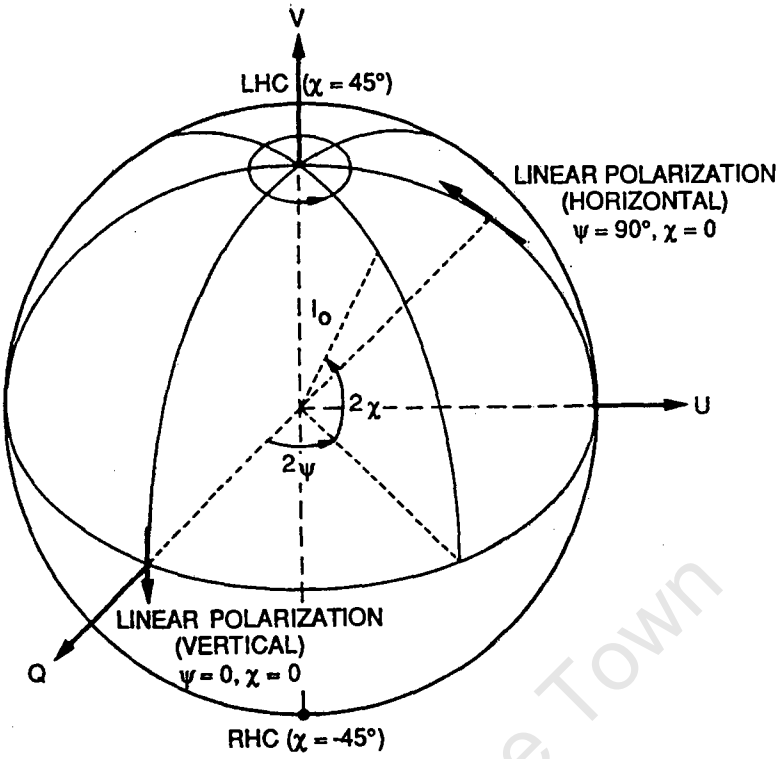

Figure 4.2: Poincare sphere with the Stokes parameters as axes. (Ulaby [96, p12])

However, the complete polarization signature can be synthesized by processing the backscatter measured simultaneously at orthogonal polarizations (HH, HV, VH and VV). Van Zyl [103] termed this processing *polarization synthesis*. This important technique is what gives polarimetry its great advantage over conventional fixed-polarization radars.

4.3.1 Polarization synthesis

Knowledge of the scattering matrix $[S]$ permits the synthesis of the polarization signature. Firstly, the 2×2 *scattering matrix* is obtained by transmitting a wave with horizontal polarization and simultaneously receiving both horizontal and vertical polarizations giving rise to the backscatter coefficients S_{hh} and S_{hv}, respectively. Similarly, the backscatter coefficients S_{vh} and S_{vv} are obtained by transmitting a wave with vertical polarization and simultaneously receiving both horizontal and vertical polarizations.

The scattering matrix has the form

$$[S] = \begin{pmatrix} S_{hh} & S_{hv} \\ S_{vh} & S_{vv} \end{pmatrix}. \tag{4.4}$$

The scattering coefficients are complex numbers as both the amplitude and absolute phase of the electric field is measured. An analogous real 4×4 matrix may be derived that relates the Stokes parameters of the scattered wave to the Stokes parameters of the illuminating wave. Thus, the scatterer can be characterized in terms of the *Stokes scattering operator* $[M]$ which is derived from the scattering matrix $[S]$.

$$\begin{pmatrix} I_0 \\ Q \\ U \\ V \end{pmatrix}^{sc} = [R]\ [\tilde{R}]\ [M] \begin{pmatrix} I_0 \\ Q \\ U \\ V \end{pmatrix}^{ill} \tag{4.5}$$

where

$$[R] = \begin{pmatrix} 1 & 1 & 0 & 0 \\ 1 & -1 & 0 & 0 \\ 0 & 0 & 1 & 1 \\ 0 & 0 & -\jmath & \jmath \end{pmatrix} \tag{4.6}$$

and $[\tilde{R}]$ is the transpose of the matrix $[R]$.

The Stokes scattering operator is given by

$$[M] = [\tilde{R}]^{-1}\ [W]\ [R]^{-1} \tag{4.7}$$

where

$$[W] = \begin{pmatrix} S_{hh}S_{hh}^* & S_{hv}S_{hv}^* & S_{hh}S_{hv}^* & S_{hv}S_{hh}^* \\ S_{vh}S_{vh}^* & S_{vv}S_{vv}^* & S_{vh}S_{vv}^* & S_{vv}S_{vh}^* \\ S_{hh}S_{vh}^* & S_{hv}S_{vv}^* & S_{hh}S_{vv}^* & S_{hv}S_{vh}^* \\ S_{vh}S_{hh}^* & S_{vv}S_{hv}^* & S_{vh}S_{hv}^* & S_{vv}S_{hh}^* \end{pmatrix}. \tag{4.8}$$

The Stokes scattering operator $[M]$ should not be confused with the Mueller matrix $[\mathcal{M}]$ which also relates the scattered Stokes vector to the incident Stokes vector. Unfortunately, both $[\mathcal{M}]$ and $[M]$ have in the past been called the Stokes matrix. The difference between the two matrices is discussed by Ulaby [96].

The average Stokes parameters of the wave scattered by an object that varies statistically, either in time or in space, are related to the Stokes parameters of the illuminating wave through an average Stokes scattering operator [103]. The average Stokes scattering operator $[M]_{ave}$ is calculated by averaging the elements of $[M]$. Thus,

$$[M]_{ave} = \sum_{n=1}^{N} [M]^{(n)} \tag{4.9}$$

where $[M]^{(n)}$ is the Stokes scattering operator of the nth measurement.

Finally, the scattering cross section σ is calculated for all possible transmit and receiving antenna polarizations. The polarization synthesis equation is given by [103, p536]

$$\sigma(\chi_i, \psi_i, \chi_j, \psi_j) = \frac{4\pi}{k^2} \begin{pmatrix} 1 \\ \cos(2\chi_i)\cos(2\psi_i) \\ \cos(2\chi_i)\sin(2\psi_i) \\ \sin(2\chi_i) \end{pmatrix} \left(\sum_{n=1}^{N} [M]^{(n)} \right) \begin{pmatrix} 1 \\ \cos(2\chi_j)\cos(2\psi_j) \\ \cos(2\chi_j)\sin(2\psi_j) \\ \sin(2\chi_j) \end{pmatrix} \tag{4.10}$$

where

k = wave number of transmitted signal,
χ_i = ellipticity angle for the receiving antenna,
ψ_i = ellipse orientation angle for the receiving antenna,
χ_j = ellipticity angle for the transmitting antenna,
ψ_j = ellipse orientation angle for the transmitting antenna.

The function $\sigma(\chi_i, \psi_i, \chi_j, \psi_j)$ as described by equation 4.10 is refer to as the *polarization signature* of an ensemble of scatterers. A complete discussion of polarization synthesis methods in contained in Ulaby [96, p27].

4.3.2 Polarization signature of typical targets

Since the polarization signature is a function of four quantities, representation of the most general signature is awkward. For simplicity, the polarization signatures presented is for the case of identical transmit and receive antenna polarizations. In this case the signature is referred to as the *copolarization signature* of the scatterer.

To illustrate how the copolarization signatures can be used to identify the scatterer, four special cases will be discussed namely, the signature of a large smooth dielectric, the signature of a dihedral corner reflector, the signature of a trihedral corner reflector, and the signature of a rough dielectric surface.

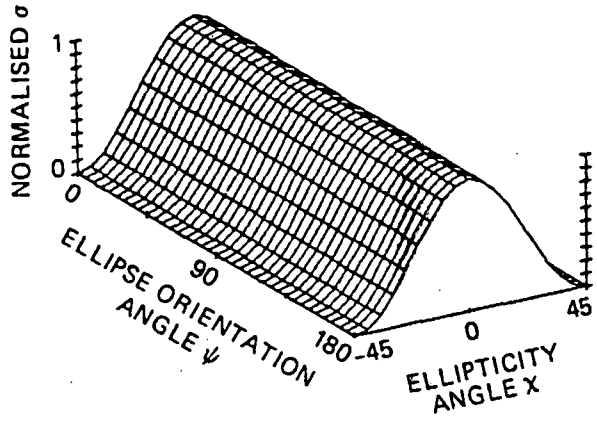

Figure 4.3: Copolarization signature of a smooth dielectric surface with $\varepsilon = 6$ at normal incidence. (Van Zyl [103, p537])

Theoretical signature of a smooth dielectric surface

The scattering matrix for an infinitely large, smooth dielectric is given by [103]

$$[S] = \frac{1-\sqrt{\varepsilon}}{1+\sqrt{\varepsilon}} \begin{pmatrix} 1 & 0 \\ 0 & 1 \end{pmatrix} \tag{4.11}$$

where ε is the dielectric constant of the surface.

The copolarization signature of such a surface is shown in Figure 4.3. From this signature it can be deduced that any linear polarization ($\chi = 0$) provides the maximum backscatter cross section and that the backscatter cross section is independent of polarization orientation angle. This kind of signature can be expected in regions of an image where specular reflection has occurred.

Theoretical signature of a dihedral corner reflector

The scattering matrix for a dihedral corner reflector is given by [103]

$$[S] = \begin{pmatrix} R_h(\varepsilon_1, \theta_{i1}) R_h(\varepsilon_2, \theta_{i2}) & 0 \\ 0 & -R_v(\varepsilon_1, \theta_{i1}) R_v(\varepsilon_2, \theta_{i2}) \end{pmatrix} \tag{4.12}$$

where ε_1 and ε_2 are the dielectric permittivities of the two surfaces comprising the corner, and $R_h(\varepsilon, \theta)$ and $R_v(\varepsilon, \theta)$ are the Fresnel reflection coefficients for

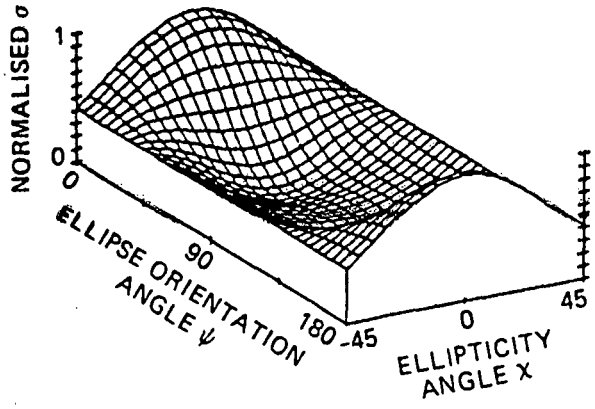

Figure 4.4: Copolarization signature of a dihedral corner reflector with $\varepsilon_1 = \varepsilon_2 = 6$ incidence angle 45°. (Van Zyl [103, p538])

horizontal and vertical polarizations, respectively.

The copolarization signature for a dihedral corner reflector with $\varepsilon_1 = \varepsilon_2 = 6$ and incidence angles 45° is shown in Figure 4.4. Note that the copolarization signature has a maximum for horizontal polarization and two minima for linear polarizations with orientation angles of 62° and 118°. Theoretically these minima are nulls which indicate that the transmitted electric field is orthogonal to the received electric field.

Theoretical signature of a trihedral corner reflector

The scattering matrix for a trihedral corner reflector, when illuminated along its boresight, is given by [96, p38]

$$[S] = \frac{kl^2}{\sqrt{12}\pi} \begin{pmatrix} 1 & 0 \\ 0 & 1 \end{pmatrix} \tag{4.13}$$

where k is the wave number and l is the dimension of the corner reflector.

The polarization signature of a trihedral corner reflector is identical to the signature of a large smooth dielectric as shown in Figure 4.3. The signature shows that the backscatter from the reflector is independent of the ellipse orientation angle which further implies that the polarization response is not sensitive to rotations of the trihedral reflector. Hence, trihedral corner reflectors are used for radiometric calibration of radar images [21] [38] [43].

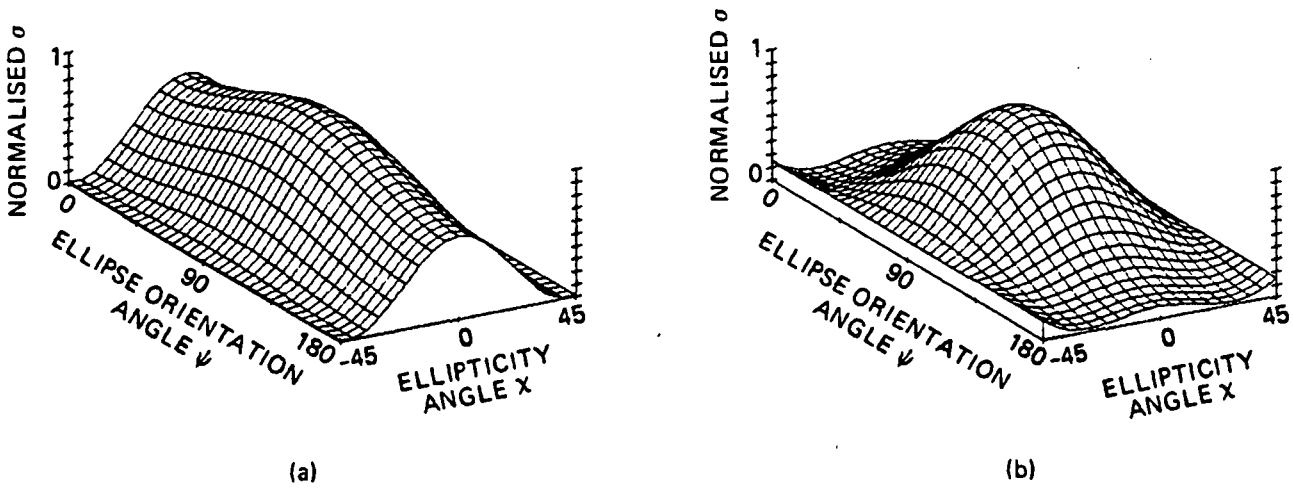

Figure 4.5: Theoretical copolarization signature for rough surface scattering at incidence angles of (a) 20° and (b) 50°. The surface is characterised by $kh = 0.1$, rms slopes 5°, and $\varepsilon = 81$. (Van Zyl [103, p539])

Theoretical signature of a rough dielectric surface

The scattering of electromagnetic waves from rough surfaces is discussed in Chapter 2. However, the theory presented in Chapter 2 (Sections 2.3.2 and 2.3.3) is not adequate since a second-order model is needed for polarimetry. Van Zyl [103] used an extension of the small perturbation model to obtain the copolarization signature of a rough dielectric surfaces (see Figure 4.5). The theoretical copolarization signature is calculated for an incidence angle (20°) at which specular reflection dominates, and for an incidence angle (50°) at which Bragg scattering dominates. Note the similarity between the copolarization signatures obtained for a large smooth dielectric surface (Figure 4.3) and a rough dielectric illuminated at an incidence angle of 20° (Figure 4.5a).

At an incidence angle of 50°, the copolarization signature has a maximum at vertical polarization and two nulls at elliptical polarizations.

4.4 Coefficient of variation

The polarization signature of a resolution cell is the average of the polarization signatures of individual measurements within that cell. If the resolution cell is so large that more than one scattering mechanism contributes significantly to the total backscattered power, the maximum and minimum values of the average polarization signature are decreased and increased, respectively. That is, the relative change of the backscatter cross section with varying polarization becomes smaller. The more the individual signatures differ from each other, the less is the

expected difference between the maximum and minimum values. This difference between the maximum and minimum values is expressed in the *coefficient of variation*, defined as [103]

$$v = \frac{\sigma_{min}(\chi_i, \psi_i, \chi_j, \psi_j)}{\sigma_{max}(\chi_i, \psi_i, \chi_j, \psi_j)}. \tag{4.14}$$

The smaller the v, the more the backscatter cross section changes with a change in polarization. Thus, v is an indication of the degree to which polarization can be used to enhance or suppress the backscatter from a collection of scatterers. A relatively large v suggests that changing the polarization will *not* change the measured backscatter. For example, the coefficient of variation of vegetated areas is large which indicates that HH, VV or any arbitrary combination of transmit and receive antenna polarization will not affect the measured backscatter. Whereas, a relatively small v indicates that the backscatter is highly polarized. Highly polarized backscatter can be suppressed by using a transmit and receive antenna polarization corresponding to the minimum (or null) of the polarization signature. Similarly, highly polarized backscatter can also be enhance by using a transmit and receive antenna polarization corresponding to the maximum value of the polarization signature. An application using the coefficient of variation is discussed in Chapter 6.

4.5 Summary and Conclusion

In this chapter the theoretical basis of polarimetry is examined. Below is a brief outline of the procedure required for obtaining the polarization signature of terrain.

- The imaging radar must have a polarimetric capability so that the scattering matrix $[S]$ can be formed. The scattering matrix is formed by transmitting with horizontal polarization and receiving both horizontal and vertical polarizations. This is interleaved with pulses vertically polarized, again receiving both horizontal and vertical polarizations.
- The Scattering matrix $[S]$ is converted to the Stokes scattering operator $[M]$, several of which are then averaged to form $[M]_{ave}$ for the region of interest.
- Finally, the scattering cross section can be calculated via the polarization synthesis equation for any arbitrary combination of transmit and receive antenna polarizations. This information is used to form the polarization signature.

The polarization signature is used, where possible, to identify the dominant scattering mechanism. As an example, the dihedral corner reflector signature can be used to identify buildings in an image, or a large smooth dielectric surface signature indicates the locations of clear-cut areas in an image of forest vegetation.

The coefficient of variation indicates the degree to which the backscatter is polarized and is used to determine which transmit and receive antenna polarizations will enhance or suppress an image feature.

Examples of polarimetric uses are discussed in the chapters dealing with remote sensing applications.

Chapter 5

Geological Applications of SAR

The aim of this chapter is to report on the results of an investigation into the uses of radar in remotely sensing geology. In recent years the imaging techniques applied to geology have developed rapidly. Most of this development has been in radar remote sensing with polarimetric and multifrequency Synthetic Aperture Radars (SAR) becoming popular.

There are numerous geological applications of SAR which generally fall into one of two groups, namely surface and subsurface applications. The latter, which is a unique feature of radar imaging, will be discussed first. In this section, microwave penetration of a medium (sand) is discussed with particular emphasis on the maximum penetration depth and the radar parameters at which this maximum depth can be obtained. This theory is then backed with examples of subsurface imaging successes. This section is concluded with the optimum radar parameters for subsurface work.

The next section is on surface mapping and discusses the past and present mapping techniques. The methods used to interpret and enhance conventional radar images are discussed first. This is followed by a discussion on multifrequency and multipolarization radar imaging with the emphasis on the additional information that can be extracted from an image using this relatively new technology.

5.1 Subsurface mapping

Low loss material, such as dry sand, which covers most of the surface of arid regions can easily be penetrated with low frequency radar. Thus, the images formed will reveal the subsurface geology. Firstly, the factors affecting microwave penetration depth in soil is discussed with a view to determining which radar and soil parameters maximize soil penetration depth. This is followed by case studies

of successful subsurface mapping where the radar and soil parameters are given for comparison with the optimum parameters.

5.1.1 Factors affecting the microwave penetration depth in soil

A plane wave incident on a surface will in general be partially absorbed and partially reflected. The surface scattering strength is proportional to the relative complex dielectric constant of the surface and the angular scattering pattern is governed by the surface roughness.

The part of the microwave energy absorbed will be attenuated due to two loss mechanisms which prevent the energy from propagating indefinitely. Firstly, the mechanism of volume scattering causes a redistribution of the energy in the transmitted wave into other directions. This results in a loss from the transmitted wave. Also, a wave propagating inside a physical medium experiences a loss due to conduction. The total loss which is the sum of scattering and conduction losses is usually referred to as extinction. The extinction per unit length is called the extinction coefficient.

Scattering loss

The scattering loss is usually negligible compared to the conduction loss. The theory in this section is included as proof that the above assumption is valid. Roth [78] showed that for a finite range of frequencies and/or particle size the scattering loss can be of a similar order of magnitude as the conduction loss. In this expression, r_0 is the average size of the particles which constitute the medium and λ is the wavelength of the transmitted signal.

$$0.1 < \frac{r_0}{\lambda} < 100 \tag{5.1}$$

In subsurface imaging of arid regions, the medium obscuring the underlying geology is usually sand with an average particle size of approximately $1mm$ (see Appendix A). Thus, for wavelengths longer than 1 cm (or frequencies below 30 GHz), the scattering loss is negligible. This condition is easily satisfied for all known SAR imaging radars.

Conduction loss

The main loss mechanism in microwave propagation is the conduction loss, since scattering loss is negligible for the medium and frequencies used. The conduction

loss is automatically included in the solution to Maxwell's equations when a lossy medium is assumed.

This loss is expressed in the field attenuation coefficient which is given by (Chapter 2)

$$\alpha = \frac{2\pi}{\lambda_0}\left\{\frac{\mu_r\varepsilon_r'}{2}\left[\left(1+\left(\frac{\varepsilon_r''}{\varepsilon_r'}\right)^2\right)^{0.5}-1\right]\right\}^{0.5} \tag{5.2}$$

where λ_0 is the wavelength in free space, ε' and ε'' are the real and imaginary parts of the dielectric permittivity, and μ_r is the relative permeability of the medium which is approximately 1 for most natural materials.

The field attenuation coefficient α is an indication of the radar signal attenuation in the medium. Thus, the skin depth δ_s which is defined as the inverse of α, is an indication of the depth to which the microwave energy can penetrate. However, the skin depth does not indicate the subsurface depth to which the radar can successfully image since the skin depth is determined by the medium only, whereas the imaging depth is determined by the medium through which the radar signal is propagating as well as the roughness and permittivity of the subsurface layer from which the radar signal must reflect. To further complicate matters, the roughness and permittivity of the subsurface layers are functions of frequency. The imaging depth is usually a fraction of the skin depth value.

Factors affecting the dielectric constants

The previous section showed that the complex dielectric constant of the soil largely determines the field attenuation coefficient, which in turn determines the depth of microwave penetration. Although it can be shown that accurate prediction of permittivity based on easily obtainable soil information is not practical, a knowledge of the parameters that affect permittivity is important in recognising potential subsurface imaging environments. Empirical observations show that soil moisture, soil type, soil temperature, soil water salinity and soil density (or compaction) affect soil permittivity. These influences on soil permittivity are discussed in Chapter 3. The three most important soil parameters are discussed below.

Soil moisture The complex dielectric constant of soil has been found by many researchers to be highly sensitive to the moisture content of the soil. *In situ* measurements (Berlin [7], Farr [36], McCauley [67]) as well as laboratory measurements (Ansoult [3], Hallikainen [48], Hoekstra [50], Topp [89] and many oth-

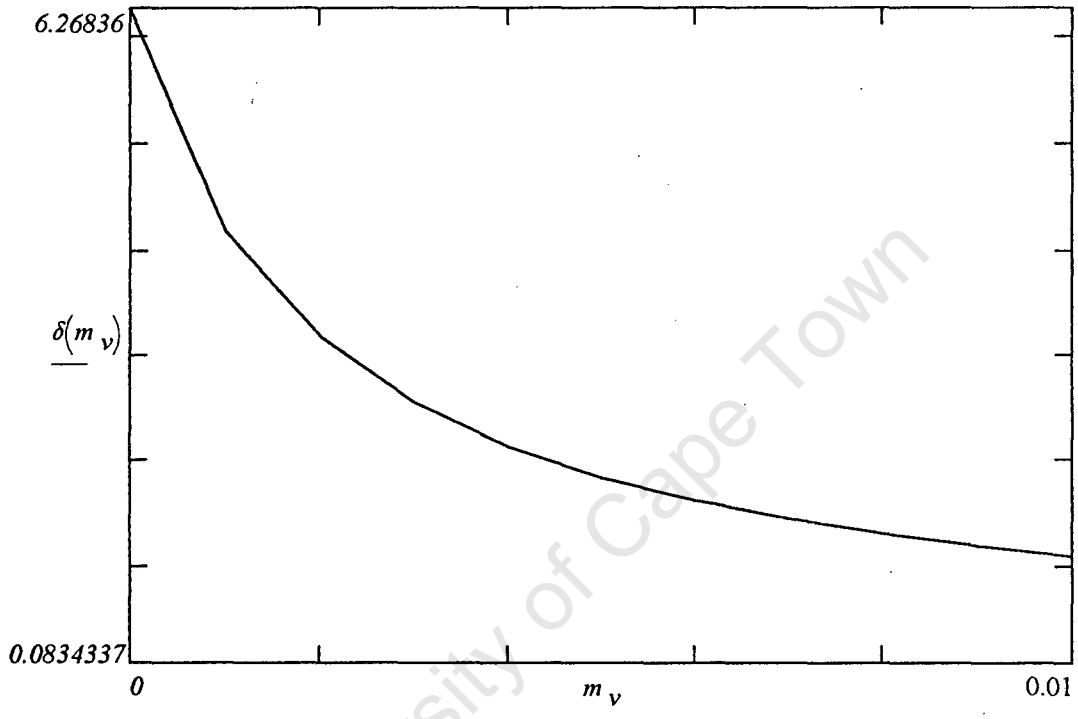

Figure 5.1: Simulation of skin depth in metres as a function of volumetric soil moisture for soil with a textural composition of 60% Sand, 20% Clay, at a frequency of 1.4 GHz. The simulation is based on the empirical dielectric model of Hallikainen [48] (see Appendix D).

ers) prove empirically that moisture content significantly influences the complex dielectric constant and thus determines radar signal attenuation in soils.

The relative dielectric permittivity ε' of dry soil (sand and/or clay) ranges from 3 to 4, independent of frequency. As water is added, the relative dielectric permittivity increases rapidly as pure water has a value of approximately 80 (for frequencies below 1 GHz). It is then obvious that the dielectric constant of a soil is greatly influenced by the volumetric water content. This is evident in the simulation results (Figure 5.1) which show the effect of soil moisture on the skin depth value.

Soil type The complex dielectric constants ε' and ε'' are dependent on soil textural composition [13], [20], [48], [89], [106]. The textural composition of soil is defined in terms of the percentages by weight of Sand, Silt and Clay in the sample (see Appendix A).

Hallikainen's [48] research shows that at any given moisture content and at microwave frequencies, ε' was found to be roughly proportional to sand content and inversely proportional to clay content. This relationship between ε' and soil texture occurred at all frequencies from 1.4 GHz to 18 GHz, however the magnitude of the effect was found to decrease with an increase in frequency. The behaviour of ε'' does not exhibit a simple dependency on soil textural components. Campbell [13] researched the behaviour of ε' and ε'' in the frequency range 1 MHz to 50 MHz and observed a similar soil type dependency.

Soil Salinity The real part of the complex dielectric constant of soil ε' is unaffected by the salinity of the soil between 1 MHz and 1 GHz. Topp's [89] research proves that the presence of salt, NaCl and $CaSO_4$ in the liquid phase of the soil-water caused no measurable effect on ε'.

At frequencies below 5 GHz, the imaginary part of the complex dielectric constant of saline soil is predominantly controlled by the ionic conductivity of the soil water. Topp [89] observed that the presence of salt in the soil water caused greater signal attenuation which is indicative of greater ε'' values since ε' is unaffected by salinity.

Conclusion

Subsurface imaging is feasible in sandy arid environments. This was deduced by evaluating Equation 5.2 using empirical permittivity values gleaned from published data [13] [72] and dielectric models [48].

The field attenuation coefficient α is minimized when the soil composition is predominantly sand. Thus, for a given frequency and soil moisture content, sand consistently has the lowest attenuation. However, the greatest influence on microwave attenuation is the moisture content of the soil. Greater microwave penetration is observed for soils with lower moisture content.

The feasibility of subsurface imaging in sandy arid environments is evident when analysing the environments of the regions which have been successfully imaged.

5.1.2 Past achievements of remote sensing of subsurface geology

The case studies contained in this section reiterate the conclusions reached in the previous section. Firstly, the penetration depth is highly sensitive to the moisture content of the soil. Next, the preferred medium for microwave penetration is sand. And lastly, better microwave penetration is obtained at lower frequencies.

The ability of SAR to penetrate arid soil was first discovered by the Shuttle Imaging Radar A (SIR-A) experiment in 1981. The images in Figure 5.2 show the difference between the surface image and the subsurface image. The drainage channels barely visible in the Landsat image are sharply defined in a SIR-A radar image of the same area.

The ability of SAR to penetrate arid soil was investigated further with the Shuttle Imaging Radar B (SIR-B) mission experiment of 1984. Since the microwave penetration was expected in certain regions, greater effort was made to quantitatively record the details of the area imaged. The areas where microwave penetration was expected are discussed below. Note that SIR-A and B operated at 1.3 GHz which is *not* optimum but nevertheless gave good results because the areas imaged were extremely dry.

Nevada Desert

Farr [36] used the SIR-B radar signals to measure the microwave attenuation as a function of soil moisture in natural soils at two sites in the Nevada desert. The area has an arid climate averaging about 250 mm of precipitation per annum. The rainfall figures for June to September 1984 averaged 11 mm per month. The last rainfall recorded in the area was 1 mm on 19 September 1984. Thus, microwave penetration of the sand was expected.

The area is sparsely vegetated, covering about 15 percent of the surface. The surface was also covered with limestone pebbles of a few centimeters in size.

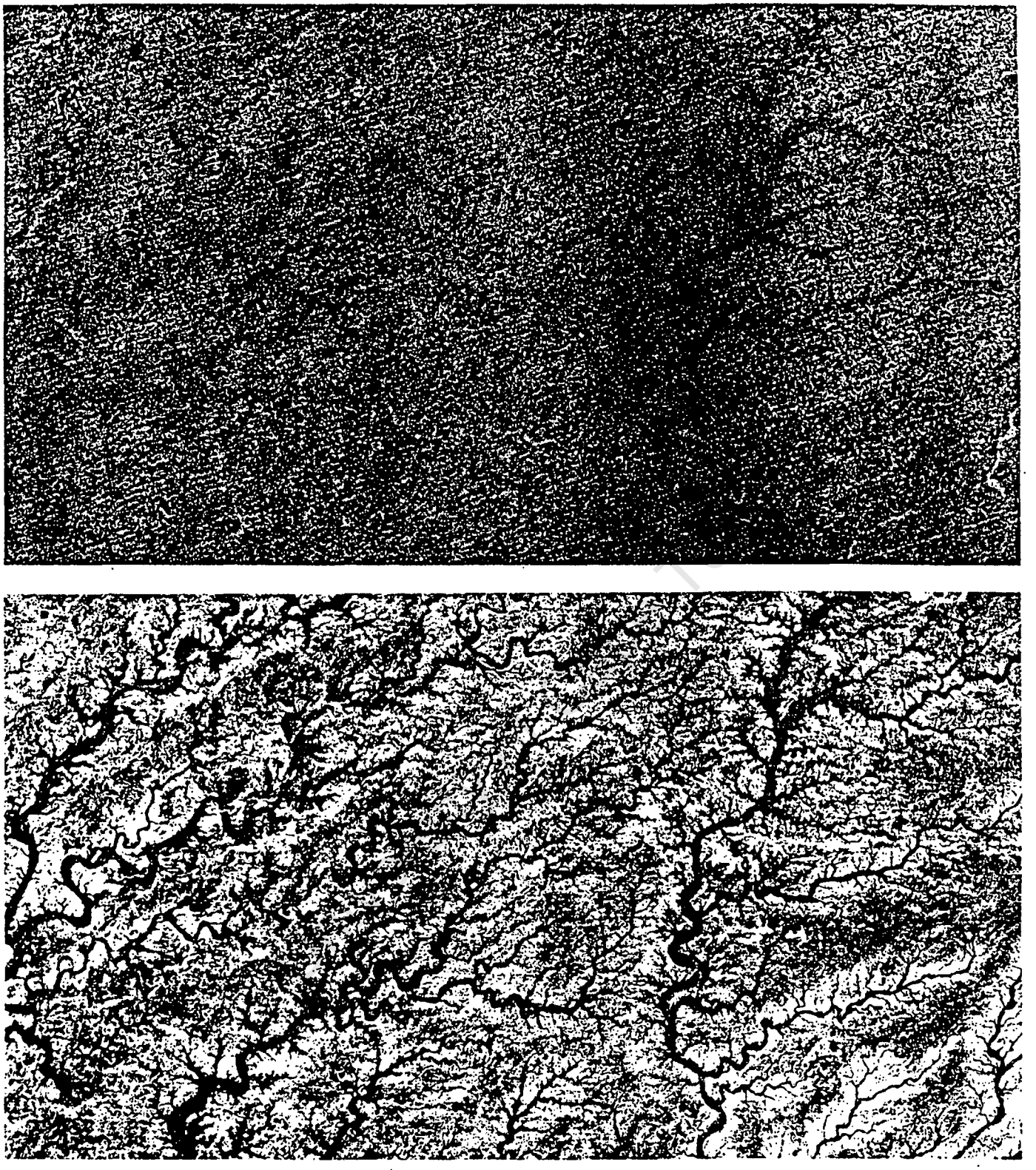

Figure 5.2: Landsat image (top) and SIR-A radar image (bottom) of an area on the border of Iraq and Saudi Arabia. (Elachi [26, p50])

The subsurface contained layers of fine and course rounded pebbles and cobbles, mostly less than 5 cm with some cobbles up to 15 cm (Farr [36, p591]).

The two receivers were buried so that the microwave power that penetrated the surface could be measured. The output of the receivers was sampled in 100 ms increments for about 2.5 min. The difference between the power observed at the two receivers can be used to calculate the microwave attenuation since the path length between the two receivers is known. If the scattering of microwave energy in the soil volume is negligible when compared to attenuation of the energy, then the power loss can be used to calculate the skin depth.

Table 5.1: Microwave attenuation, soil moisture and skin depth measured at two sites in the Nevada Desert. (Farr [36, p592])

site	attenuation dB/m	moisture % weight	moisture % volume	skin depth m
A	11.8	2.8	4.2	1.7
A	16.3	2.8	4.2	1.2
B	36.2	4.6	6.9	0.56
B	28.9	4.6	6.9	0.70

The Table 5.1 shows the moisture content as a percentage of the weight and as a percentage of the volume of the sample. However, it is more common and better to use moisture content expressed as a percentage of the volume. To convert weight percent to volume percent, the average density of the unconsolidated soils (1.5 g/cm^3) is used.

Al Labbah Plateau

Berlin [7] also used SIR-B images to investigate the microwave penetration of the sand sheet of the Al Labbah Plateau in Saudi Arabia. At the time of the shuttle overpass, Berlin and his team collected soil samples so that the gravimetric moisture and complex dielectric properties could be measured in the laboratory.

Excavations in the area show that the subsurface imaging depth is between 1.24 m and 3.1 m. Laboratory analysis of the surface samples indicate that the aeolian sand is predominantly composed of quartz grains ($>$ 98 %) with minor amounts of potassium feldspar, dolomite and heavy minerals. The sands are fine- to medium-grained and are moderately sorted. Nearly all the quartz grains are rounded and pitted.

The microwave energy is reflected from the Aruma Formation. This bedrock forms the subsurface layer. Excavations of the sand covering the subsurface layer

revealed no paleosoil layers or calcified root tubes. The exposed surface of the Aruma Formation is covered with rock fragments ranging in size from pebbles to cobbles, with varying concentrations of boulders. Berlin [7] assumes that the microrelief of the exposed Aruma Formation is similar to that which underlies the sand cover.

The mean annual rainfall is 65 mm measured at the meteorological station closest to the study area. No precipitation was recorded from April 1984 to the time of the Space Shuttle overpass in October 1984. Thus, the sand was very dry at the time of the Shuttle overpass. Laboratory analysis of the sand samples collected at the surface show that the moisture content averaged 0.21 percent of the sample weight. Corresponding to this low moisture content, the dielectric constant (ε) and loss tangent (tan δ) values for the same sand samples averaged 2.503 and 0.0066 respectively (Berlin [7, p600]).

Eastern Sahara

Schaber [80] investigated the SIR-A radar images of the Eastern Sahara. He found that the microwave energy from the radar had penetrated the thin sand sheets and illuminated the underlying geology.

The Eastern Sahara is a hyperarid region with an annual precipitation of less than 1.0 mm. Most of the region is covered with a thin layer of windblown quartz sand which almost completely obscures the underlying geology. The sand sheet of the sediment blanket is centimetres to metres thick. Barchan dune trains, many tens of kilometres long, override the sand sheet. The dunes and sand sheet deposits unconformably overlie a wide variety of materials, including bedrock and alluvium which contains medium to course sand, and small pebbles.

McCauley [67] used SIR-A and SIR-B images to map the paleodrainages of the Eastern Sahara. He found the dune sand to be well sorted, mostly fine-to-medium sand with a mean grain size of 0.25 mm. This fine-grained, extremely homogeneous material is transparent to the SIR signal except where the dune height is greater than about 3 m. Field investigations by McCauley [67] indicate that the radar imaging depth is approximately 1.6 m in the sediment blanket.

Schaber [80] found that the depth to which the SIR-A signals penetrated and returned backscatter to the antenna has been documented in the field to be a maximum of 1.5 m, or 0.25 of the calculated skin depth. This is referred to as the radar imaging depth and is different to the penetration depth and skin depth. The radar imaging depth for the sand dunes overlying the sand sheet is between 2 and 3 m.

Simpson Desert

The Simpson Desert is an arid region in Central Australia. The expected microwave penetration of the sand in the Amadeus Basin area of the Simpson Desert did not occur [64]. The rainfall in the area is extremely erratic with an average of 140 mm to 180 mm per year. However, heavy rainfall occurred immediately prior to the SIR-B overpass. This heavy rainfall saturated the surface sands and greatly limited the ability of the radar's microwave energy to penetrate the surface cover. Thus, no subsurface imaging was recorded in this area.

Mojave Desert

As a result of SIR-A and SIR-B success in subsurface imaging, SEASAT images of semi-arid regions were re-evaluated. Blom [10] detected subsurface features in a SEASAT radar image of Means Valley in the Mojave Desert, California. Although the SAR image was taken in August 1978, the subsurface ability of the radar was only discovered in 1984.

SEASAT, like SIR-A and SIR-B operated in L-Band with a 20 m resolution. The SAR image of the area showed the presence of a subsurface lineament which investigations revealed to be a dyke intruding into the host bedrock. Seismic-reflection data in the vicinity of the lineament indicate a depth to bedrock ranging from 0.6 m to 2.7 m, with an average of 1.6 m [10, p347]. The material covering the bedrock is predominantly fine-grained sand and silt. The soil moisture is estimated using the rainfall measurements of residents who live 8 km to the south of the study area. Soil moisture measurements taken in 1982 have an average of 0.74 weight-percent which is considered higher than the 1978 soil moisture values because of heavy rainfall in 1982.

Karakum Desert

The Russian airborne SAR produced images of the Karakum desert in Turkmenia which is situated east of the Caspian Sea and south of the Aral Sea. The SAR which is mounted on a TU-134 operates at two frequencies, namely at X-Band (4.0 cm) and VHF (250.0 cm). The X-Band frequency is used to map surface structures whereas the VHF signal penetrates the sandy soil which covers most of the region and thus provides subsurface information. This section discusses methods employed to enhance the low frequency image provided by the Russians. In particular, methods for highlighting the water containing areas of the images were investigated.

There are two mechanisms which act on incident radar signals which would enable the water-areas in the radar image to be identified. Both these mechanisms cause

Figure 5.3: X-Band SAR image of the sand covered Karakum desert of Turkmenia.

Figure 5.4: VHF SAR image of the sand covered Karakum desert of Turkmenia.

the water containing areas to have low pixel values which are represented by dark shades in the grey-scale image. The mechanisms are :

- REFLECTION : This occurs when the dielectric interface between relatively dry soil and soil containing large amounts of water is radar smooth. As a result of the radar smooth interface, the incident signal specularly reflects at the interface and does not reach the receiver.
- ATTENUATION : This occurs when there is no clear interface between dry soil and soil containing water. The incident signal is thus attenuated in relatively moist soil and does not reach the receiver.

The images used for the investigation (see Figure 5.3 and 5.4) were obtained by scanning a hardcopy of the VHF and X-Band images brought from Russia by Prof. Inggs. Geological maps of the imaged area were also provided and used as a "ground truth" reference. If the map information is correct, then the subsurface water is at a depth of approximately 20 m below the barchan dune surface. This is consistent with Olhoeft's [73] findings that show penetration of about 30 m through clay-free sand is possible for a ground penetrating radar operating at approximately 100 MHz.

Low pixel value (dark) areas of an image are usually indicative of water bearing soils. To test this hypothesis, a pixel threshold algorithm was implemented on the scanned image (Figure 5.4) to produce an image (Figure 5.5) of only two shades in which the dark areas represent subsurface water.

In a grey-scale image the pixel values are in the range 0 to 255 where 0 and 255 represent black and white respectively. The pixel threshold algorithm converts the 256 shades of grey to just black or white based on whether the original pixel value is less than or greater than the threshold value. In the image shown in Figure 5.5, the threshold value was set to 70.

There are two important criterion in determining an appropriate pixel threshold value. Firstly, if we assume that the dark areas are caused by reflection of the radar signal from the water saturated soil, then a pixel value of zero will indicate water. However, this ideal situation does not exist because the radar system noise could erroneously produce pixel values greater than zero. Secondly, the previous assumption is not necessarily true as both reflection and attenuation mechanisms can be identified on the image. Thus, the pixel threshold value was adjusted so that the water containing areas highlighted by this method coincided with the geological map.

The geological map differentiated between two soil water types, namely relatively high water content soils and low water content soils. Using a pixel threshold value of 70 produced reasonably good agreement with the high water areas indicated

Figure 5.5: VHF SAR image of the sand covered Karakum desert of Turkmenia which was modified by the pixel threshold (70) and median filter (7×7) technique.

on the map. When increasing the threshold value, some water features remain unchanged whereas other features become larger. The latter features occur where high and low water areas are adjacent to each other and the boundary is not well defined. However, there are dark areas of the image which do not correspond to water and cannot as yet be explained.

5.1.3 Optimum radar parameters

Frequency

The choice of optimum radar frequency for subsurface imaging is based on two criteria. The frequency is chosen to maximize the penetration depth of the radar signal in the obsuring medium (sand). Unfortunately, maximizing the penetration depth can result in the subsurface layer appearing radar smooth which implies specular reflection. This limits the amount of information that can be extracted from a radar image. The frequency eventually used is a compromise between these two criteria.

The influence of the radar frequency on penetration depth was discussed in Section 5.1.1. The relationship between frequency and attenuation is given in Equation 5.2. Minimum attenuation (or maximum penetration) for any medium is obtained with the lowest possible radar frequency. This is evident in the graph (Figure 5.6) of attenuation versus frequency. Although the frequency scale in Figure 5.6 ranges from 1 MHz to 1 GHz, present-day SARs are limited to frequencies greater than 20 MHz [46]. Thus, the maximum penetration depth is limited by radar hardware constraints.

The second limiting factor is the roughness of the surface and subsurface layers. The air-sand interface should be radar smooth to reflect the microwave energy that does not penetrate the sand away from the radar, but the sand-bedrock interface should be radar rough to reflect some of the microwave energy back to the receiving radar antenna. Radar roughness as defined by the Rayleigh criterion is a function of radar frequency (or wavelength). A surface is considered radar rough if the average micro-height variation h satisfies

$$h > \frac{\lambda}{8\cos\theta} \tag{5.3}$$

where λ is the wavelength in the medium and θ is the incidence angle of the wave illuminating the surface. However, before any criterion can be used, the wavelength in the sand medium λ' as well as the incidence angle of the wave illuminating the subsurface layer θ' must be calculated.

The wavelength in the sand medium is given by

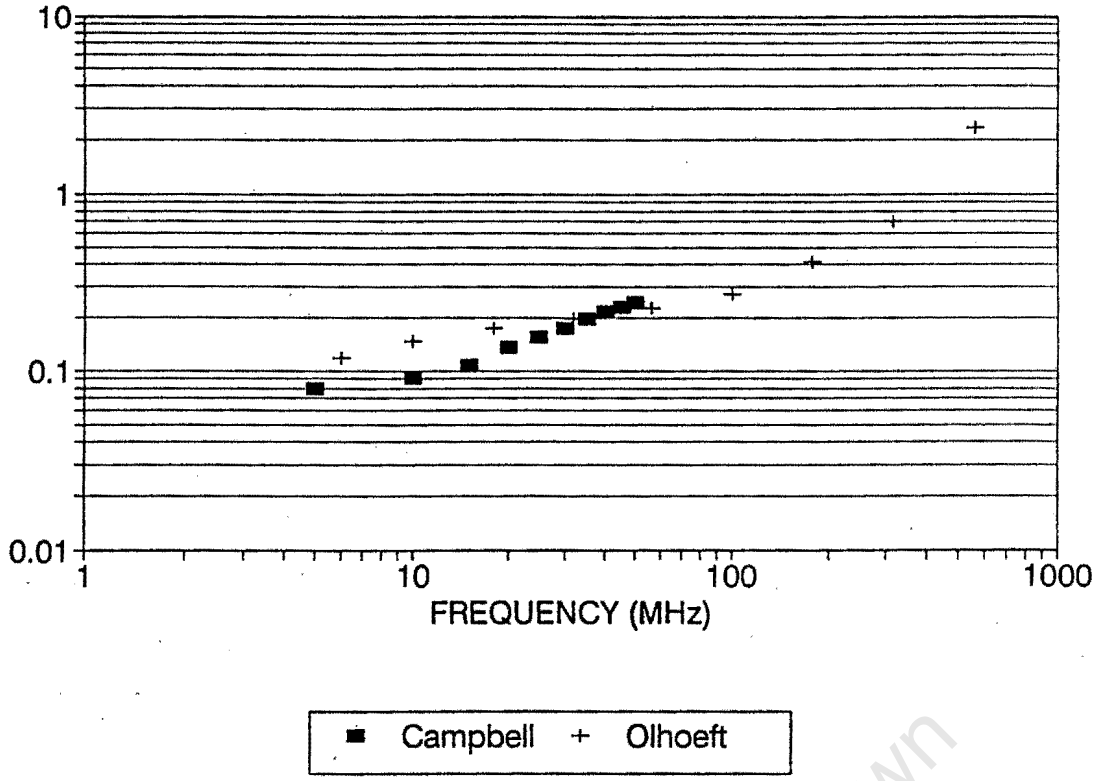

Figure 5.6: Attenuation coefficient plotted as a function of frequency. The graph was obtained by evaluating Equation 5.2 using empirical permittivity values from Campbell [13] and Olhoeft [72]. The volumetric moisture content of Campbell's data is 30% whereas Olhoeft's data is 16.4% by sample weight.

$$\lambda' = \frac{\lambda}{\sqrt{\varepsilon}} \tag{5.4}$$

where ε is the complex permittivity of the medium (sand).

Using Snell's Law of Refraction, the incidence angle in the sand medium is given by

$$\theta' = \arcsin(\sin\theta/\sqrt{\varepsilon}) \tag{5.5}$$

where θ is the incidence angle at the surface and ε is the complex permittivity of the medium (sand).

Thus, the Rayleigh criterion for the micro-height variation of the buried subsurface layer is given by

$$h' > \frac{\lambda'}{8\cos\theta'} \tag{5.6}$$

The graph (Figure 5.7) shows the results of a simulation in which the required subsurface roughness (according to the Rayleigh criterion) is evaluated as a function of frequency. Thus, for the permittivity and incidence angles used in the

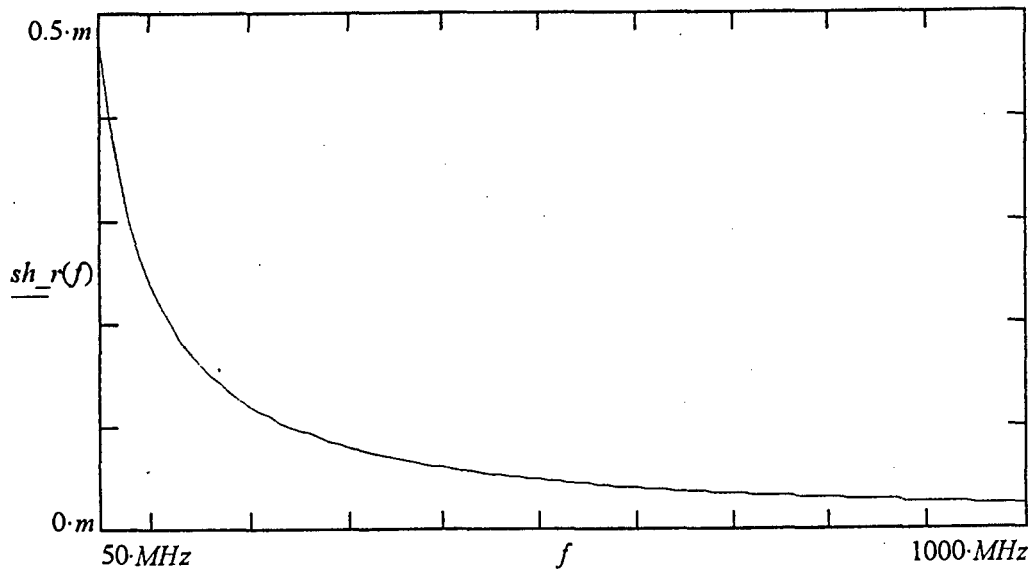

Figure 5.7: A simulation of the Rayleigh criterion showing the required subsurface roughness as a function of frequency. The simulation uses the relative permittivity of dry sand ($\varepsilon_r = 2.5$) and an incidence angle of 10° (see Appendix D).

simulation, the average variation of the subsurface can be determined at any frequency. As an example, the average subsurface variation at 50 MHz must be greater than 0.5 m to be detectable using an imaging radar. Therefore, when choosing a frequency which would enable the detection of a gravel horizon covered by sand, the size of the gravel (boulders, cobbles or pebbles) is important.

Incidence angles

The optimum incidence angle for subsurface imaging is a compromise between minimizing the path length in the sand medium and avoiding incidence angles at which specular reflections at the air-sand interface dominates the radar backscatter.

Blom [1, 9] investigated the optimum radar geometry for imaging sand dunes and found that unvegetated sand dunes behaved as quasi-specular reflectors returning energy to the imaging system only when a dune face several wavelengths on a side was nearly perpendicular to the radar beam. The interaction of radar imaging geometry and dune geometry results in a radar image of dunes only being formed if the incidence angle is less than or equal to the steepest dune slopes ($\approx$ 34°) [9, p7878]. If there are no dune slopes near perpendicular to the radar beam either due to the incidence angle being to large or due to the dune trend being at oblique angles to the radar, no mapping of dunes will be possible. Without the surface

clutter, the image formed reveals the subsurface geology.

From the above discussion it would appear that large incidence angles are best however, the path length in the sand medium should be minimized which implies the use of small incidence angles. Since the path length has less of an effect on the subsurface image than surface specular reflection, preference is given to avoiding the latter. In addition, an incidence angle equal to the angle of repose for dry sand (34°) is a worst case scenario since this can only occur in hyper-arid regions such as the Sahara and Namib deserts. Also, in areas such as the southwestern Kalahari which is dominated by linear dunes (see Appendix B), incidence angles as small as 10° can be used provided that the linear dunes are imaged obliquely (i.e. greater than 60° from perpendicular to the linear dune) [1]. Thus the optimum incidence angle for subsurface applications is between 10° and 20°.

Surface scattering models, both theoretical and empirical show that the backscattered power decreases rapidly as the incidence angle is increased (see Chapter 2). However, refraction at the air-sand interface reduces the incidence angle at the sand-bedrock interface. Thus, refraction causes the backscatter from a surface covered by very dry sand to be greater than the backscatter from the same surface without the sand cover [29]. Since, refraction has a greater effect at large incidence angles, these large angles appear to be optimum for subsurface applications. Unfortunately, the loss in backscattered power at such large incidence angles offsets any gains caused by refraction.

Polarization

The choice of optimum polarization is based on the theoretical models and empirical surface scattering data. Empirical surface scattering graphs [95] show on average that HH polarization is marginally better than VV polarization with both these polarizations being considerably better than cross-polarizations (HV and VH). The cross-polarization backscatter is on average 10 dBs below the co-polarization backscatter. Although these graphs are for surface scattering, their results can be extended to subsurface scattering and, in certain cases, the medium (sand) being penetrated enhances the scattering from the subsurface layer [29].

Elachi [29] simulated the influence of the sand medium on the subsurface backscatter and found that under certain conditions the backscatter from the subsurface is enhanced. This enhancement which is expressed as the ratio of the backscatter from a surface covered by sand to the backscatter of the same surface without any sand covering, is consistently greatest at HH polarization irrespective of incidence angles and permittivities of the sand and subsurface mediums. To investigate the enhancement further, Elachi's [29] simulation was repeated (see Appendix D)

with different sand and bedrock permittivities, and depth to bedrock values. Again, HH polarization was superior to both VV and cross polarizations.

The above discussion is only relevant if the SAR operates at a single transmit and receive polarization in which case the optimum polarization appears to be HH (ie transmit and receive horizontally). However, polarimetric SAR has made the choice of an optimum polarization obsolete since a polarimetric SAR measures the complete scattering matrix. Any arbitrary polarization can be synthesized from the scattering matrix which allows the user to determine the optimum polarization from the data set.

5.2 Surface mapping

This section covers the principles and techniques used to interpret, enhance and extract geological information from radar images. The topics covered include information extraction techniques for conventional SAR, multifrequency SAR and multipolarization SAR. Although this section is called surface imaging, the techniques can be extended to subsurfaces.

5.2.1 Conventional radar images

A conventional radar image is formed by a radar which operates at a single frequency and single polarization. A radar image combines the attributes of tone, texture, pattern, shape and scale in much the same way as do grey-tone images of shorter-wavelength radiation. They differ in the way in which these interpretable attributes are produced, but the same photogeological principles apply [24, p173]. This is particularly true of high frequency (Ku-band) radar images which are used extensively as quasi optical images for geological mapping of regions with perpetual cloud cover.

SAR images uniquely accentuate surface topography because the amount of energy backscattered to the radar antenna is largely dependent on the attitude of the surface slopes. Slopes approximately normal to the direction of wave propagation appear bright in images whereas slopes facing away from the radar appear dark in images. This shading of slopes helps the eye to perceive topography because of the pseudo-stereoscopic effect [24, p174]. Topographic emphasis is important for interpretation of the geological structures underlying destructional landforms. Topographic features with sharp angular boundaries behave like corner reflectors and thus return substantially more power than the surrounding surface making detection of small faults or dykes possible [24, p175] [10].

To improve the ability of conventional SAR to differentiate between different rock types, Blom [2] experimented with digital enhancement techniques. These techniques use the image tone (or brightness level) as well as the localized texture to discriminate between different rock types. For example, it is common knowledge that sandstones have a coarser textured drainage pattern than shales which are easily discriminable on air photographs. Thus even though sandstones and shales might have the same image tone, they might be discriminated by their texture. In an effort to quantify image texture automatically, Blom [2] experimented with Variance Pictures, HSI Split Spectrum Processing and Bandpass Texture Classification.

Variance Pictures

Since image texture is a spatial variation of image tone, the variance (standard deviation squared) of image tone over a local area is an indication of the image texture for that local area. The variance will reach a maximum when the area over which it is computed is sufficiently large to encompass the tonal variations characteristic of the texture of the sampled surface. To make a variance picture one computes the variance of a given area, say 3 pixels by 3 pixels and replaces the value of the centre pixel with the computed variance. The computing window is then moved one pixel and the process repeated until the entire image has been processed.

Blom [2] found that the classification accuracy of the thirteen rock types used in the training data set increased by 14% over the analysis done without using the variance information. For his application the most useful variance window sizes were relatively large. The window sizes listed in order of preference are: 31×31, 61×61 and 15×15.

No satisfactory pictures have been produced yet because of the problem associated with computing the variance in areas of rugged topography. Specular reflection corrupts the variance data of rugged areas and thus interferes with the display of the various rock types. The problem can be overcome by applying the variance method to areas of relatively gentle topography or using a more favourable SAR viewing geometry (ie larger incidence angles reduced specular reflections).

HSI Split Spectrum Processing

In HSI Split Spectrum Processing false colour is introduced to aid in geological interpretation of the image. This technique exploits the fact that tone variation in radar images are driven by two distinct physical mechanisms with different characteristic scales. Large scale (low-spatial frequency) features are dominated by surface variations such as vegetation and rock type whereas, high-spatial frequencies are heavily modulated by local slope effects. To separate these two mechanisms the image is filtered into high-pass (HP) and low-pass (LP) images. Colour is implemented by using the LP image to encode hue-saturation and the HP image to modulate intensity.

In conventional radar images the subtle low-frequency tone variations associated with rock and vegetation are swamped heavily modulated high-frequency returns from gullies. In contrast, the HSI split spectrum picture expresses the geologic structures in colour while retaining details such as drainages and lineaments.

Bandpass Texture Classification

This method consists of computing the two-dimensional Fourier transform of an image, and bandpass filtering the result into roughly ten channels. The output of each channel is then used to generate an image which represents the intensity of the frequency band chosen. Finally, these images are used at input to standard classification algorithms such as variance pictures. Unfortunately, the method has had only limited success.

5.2.2 Multifrequency radar imaging

The most powerful means of discriminating between surfaces with different degrees of roughness is to exploit the wavelength dependence of the Rayleigh criterion. In this way roughnesses can be used to aid in the mapping of different lithologies and superficial deposits in terrain that is bare of vegetation.

Weathering and depositional processes in deserts often cause surfaces to smooth with age while erosional processes cause a roughening. The scales of these processes are different and their rates vary with climate, rock type, and geological structure; however, their effects can be used to relatively date surfaces for studies of climate change and tectonic history. Evans [34] showed that the age of lava flows in the Cima volcanic field of the Mojave Desert of California can be deduced from the surface roughness (or microtopography) derived from multifrequency SAR data.

Sayles [79] noted that the power spectra of topography usually exhibit the relation $P = bk^m$ where the slope m of the spectrum in log-log space lies between -2 and -3. It was however the offset $\log(b)$ in log-log space, termed the "roughness amplitude" that Evans [34] showed is proportional to the surface roughness with larger roughness amplitude values indicating greater surface roughness. For the Cima lava flow surfaces, the youngest flow (0.016 million years before present) had the largest roughness amplitude.

Recently, Van Zyl [102] showed that the surface roughness amplitude could be estimated directly from multifrequency SAR data by inversion of the small perturbation model (see Chapter 2). The roughness amplitude can be related to the rms height of the surface if a form of the surface autocorrelation function is assumed when inverting the small perturbation model. However, this is not required for estimation of lava flow ages.

5.2.3 Multipolarization radar imaging

A polarimetric SAR (single frequency, multi-polarization) produces radar image data simultaneously in four linear polarizations (HH, VV, VH, HV) which has enabled surface properties such as scatterer geometry and surface roughness to be measured more accurately.

Evans [33] generated a colour composite using three polarizations (HH=red, VV=green, VH=blue) to display the information content of polarimetric images. The colour of a local area in the composite image indicates which polarization (HH, VV or VH) is dominant in that area. For example, white indicates strong backscatter at all polarizations whereas bright pink indicates a slightly higher relative return at HH. Evans [33] used this technique for mapping surficial deposits and sedimentary rocks.

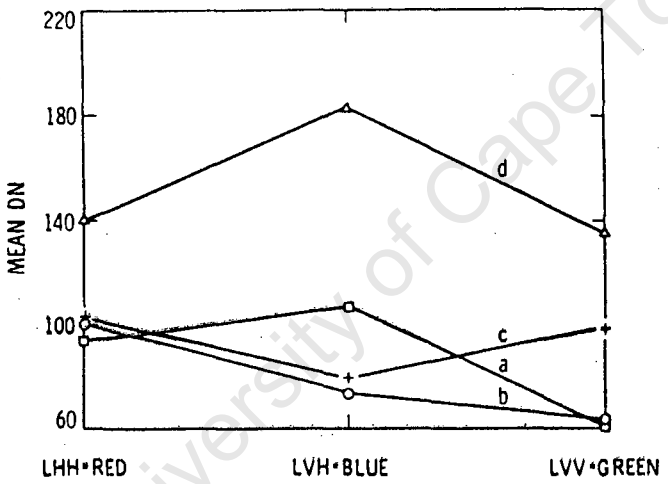

Figure 5.8: Curves showing the colour mapping of a polarimetric L-band image for four features in Death Valley California. *Curve a:* Vegetation on Furnace Creek fan. *Curve b:* Funeral fanglomerate. *Curve c:* smooth salt unit. *Curve d:* rough salt unit. (Evans [33, p251])

Figure 5.8 shows the different backscatter values (expressed in mean image Digital Number) of four surficial deposit features in Death Valley, California at three different polarizations (HH, VH and VV). Note that each of the curves is unique and will thus map to a unique colour in the composite image thus making possible the identification of a feature. As an example, blue or purple in the colour composite indicate areas where the cross-polarization backscatter is relatively strong, suggesting multiple scattering which is associated with vegetation or very

rough surfaces (*curve a* of Figure 5.8). Similarly, the halite deposits are divided into rough and smooth facies which have distinctly different responses to cross-polarized illumination. Thus curves *c* and *d* of Figure 5.8 appear blue-white and greenish-orange in the colour composite, respectively.

The polarization signature which is synthesized by processing the polarimetric radar data of a region in the image has recently been shown to provide considerably more surface information than conventional radar images [103]. Polarization signatures have been used for relative age determination of volcanic surfaces [35]. The method is based on the premise that surface roughness changes with time. This is caused mainly by rubbling of flow projections and by filling in the flow depressions with wind blown silt. The signatures obtained for these areas were almost identical, however the pedestal (minimum value of the normalized polarization signature) appeared in general to decrease with flow age which is consistent with decreasing roughness with age.

5.2.4 Multisensor classification of sedimentary rocks

Conventional SAR (single frequency, signal polarization) has a limited classification ability since surface roughness is not unique to any particular rock type. However, SAR used in conjunction with other sensors such as Landsat Thematic Mapper (TM) and Thermal Infrared Multispectral Scanner (TIMS) can greatly improve rock type classification. Evans [31] and Blom [2] showed empirically that classification of a variety of rock types can be improved using multisensor data sets that are sensitive to different characteristics such as mineralogy and surface roughness.

5.2.5 Optimum radar parameters

The optimum radar parameters are difficult to estimate because drawing comparisons between radar images which were imaged with different sensors is only possible for calibrated SARs. (However, calibrated SARs are rapidly becoming the norm. In calibrated SAR images the image pixel number is related to the radar backscatter or radar cross section σ° via look-up tables.) In the absence of readily available calibrated SAR data, the optimum SAR parameters can only be determined if the same area is imaged by the same imaging radar, which implies that the imaging radar must operate at more than one frequency, polarization, or incidence angle. Such a state-of-the-art radar has only recently become available hence the lack of data on which to base the choice of optimum parameters.

However, Blom [11] used multifrequency and multipolarization scatterometer data to determine the best frequency, polarization and incidence angles for lava

flow and sedimentary rock discrimination. The data were acquired at four frequencies (P-, L-, C- and Ku-band), four polarizations (HH, HV, VV, VH) and incidence angles at 5° increments. Unfortunately, the P-band data was not used which limits the usefulness of the results. The method used to determine the optimum parameters is a statistical procedure called linear discriminant analysis. The procedure is a supervised classification algorithm in which the user provides training data sets for the groups that are analysed for their separability by the sequential addition of variables.

For separation of lava flows, shorter wavelengths, smaller incidence angles and horizontal polarization are best. For sedimentary rock discrimination, longer wavelengths, larger incidence angles and vertical polarization are best.

Chapter 6

Soil moisture and vegetation mapping

This chapter reports on the results of an investigation into the use of Synthetic Aperture Radar (SAR) for remote sensing of near-surface soil moisture and vegetation type discrimination.

Firstly, the principles of remote sensing of non-vegetated near-surface soil moisture is discussed. Also discussed are the techniques used to minimize the effect of the "confusion factors" namely, vegetation canopies, random roughness and periodic surface roughness. It will be shown that the effects of these factors are minimized by careful choice of the imaging radar parameters. This section is concluded with a discussion of the optimum radar parameters for soil moisture retrieval.

The next section discusses past and present-day techniques, as well as the optimum radar parameters for vegetation type discrimination in radar images. As in many other applications, polarimetry is becoming increasingly popular. Thus, this section also includes polarimetric techniques for the unsupervised classification of vegetation. Lastly, a model for the prediction of vegetation backscatter is discussed.

6.1 Near-surface soil moisture mapping

The ability to measure soil moisture content remotely has been shown by many researchers (Beaudoin [6], Dobson [18, 19, 20], Oh [71], Ulaby [92, 93, 94] and Wang [105]) to be feasible. Soil moisture is inferred from one of several factors which influence radar backscatter. Hence, successful soil moisture measurement depends on two criteria namely, the relationship between soil moisture and radar

backscatter be known, and the effect on radar backscatter of "confusion factors" (vegetation canopies, local terrain slope, random surface roughness and periodic surface patterns) be minimized.

6.1.1 Principles of operation

Radar backscatter is influenced by physical parameters (surface roughness and surface permittivity) and radar parameters (local incidence angle, frequency and polarization). Soil moisture is inferred from the surface permittivity (see Chapter 3) which is in turn deduced from the measured radar backscatter (see Chapter 2).

Theoretically, the maximum power difference that can be caused by soil moisture is 11 dB [19]. This is obtained by calculating the power reflection coefficient of a smooth surface at nadir (0° incidence angle). The power reflection coefficient is given by

$$\Gamma = \left| \frac{\sqrt{\varepsilon} - 1}{\sqrt{\varepsilon} + 1} \right|^2 \tag{6.1}$$

where $\varepsilon = \varepsilon' - j\,\varepsilon''$. Γ was found to range between 0.04 for dry soil and 0.52 for water saturated soil, which corresponds to a difference of 11 dB. This value is slightly lower than the 12 to 15 dB dynamic range obtained using both truck mounted and airborne scatterometers. There are two possible explanations for the discrepancy namely, the existence of subsurface effects and an impedance-matching layer at the surface [19].

Ulaby [92, 94] investigated the correlation between radar backscatter and the soil moisture at subsurface depths ranging from 0 to 15 cm. He found that it was not possible to determine the effective depth of the layer responsible for the observed scattering coefficient.

Ulaby [92] statistically evaluated the correlation between σ° and m_x where m_x is the average moisture in the 0-x cm layer. Figure 6.1a and 6.1b shows the correlation coefficient $\rho(\sigma^\circ, m_x)$ plotted as a function of x at three frequencies for smooth and rough surface fields. As can be seen, $\rho(\sigma^\circ, m_x)$ is independent of frequency and depth x for both fields. Similar results were obtained for vegetated soil with the only difference being in the depth at which the correlation coefficient was highest. For the bare soil case [92], $\rho(\sigma^\circ, m_x)$ was maximum at the 0-1 cm layer. However, for the vegetated soil case [94], $\rho(\sigma^\circ, m_x)$ was maximum at the 0-9 cm layer for corn (ρ=0.92) and 0-5 cm layer for milo (ρ=0.92). The differences in $\rho(\sigma^\circ, m_x)$ are thought to be caused by variations in the natural soil moisture profiles of the corn and milo (grain sorghum) fields.

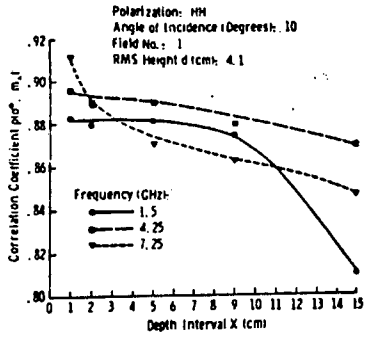

(a)

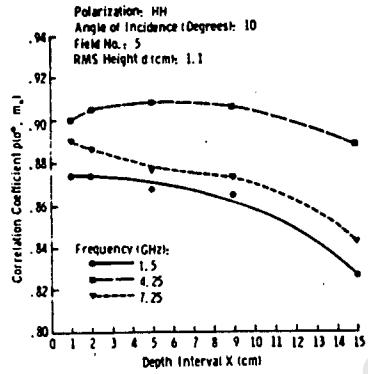

(b)

Figure 6.1: Correlation coefficient between radar backscatter $\sigma°$ and volumetric soil moisture m_x as a function of subsurface depth x for (a) a rough surface field and (b) a smooth surface field. (Ulaby [92, p292])

Returning to the discrepancy between the calculated and observed dynamic range, the difference appears to be the result of an impedance-matching layer at the surface. Since the upper millimetres of a soil are considerably drier on a volumetric basis than the average upper centimetres, a transition zone is formed which matches the intrinsic impedance of the air to that of the deeper moist soil [19]. Thus, the radar backscatter is proportional to the soil moisture content at an unknown subsurface depth. But the exact subsurface depth does not have to be known since the moisture at different depths is statistically related (i.e. the moisture content at depth x is statistically dependent on the moisture content at depth $(x + 1)$).

Empirical measurements by Dobson [19] and Ulaby [92, 94] using truck mounted scatterometers observed that radar backscatter from non-vegetated soils was linearly dependent on the volumetric water m_v in the upper 2 to 5 cm of soil.

$$\sigma°(dB) = A + Bm_v \tag{6.2}$$

For a given sensor combination of frequency, polarization and angle of incidence, the empirically derived regression coefficients A and B were found to be depen-

dent upon soil surface roughness and soil texture, wherein A is primarily controlled by surface roughness, and B is primarily controlled by soil texture [19]. The effect of the surface roughness on the offset A can be seen in Figure 6.2. In addition, the sensitivity term B (i.e. the first derivative of Equation 6.2) was observed to be dependent on both frequency and angle of incidence (see Figure 6.3). Linear regression is restricted to non-saturated soils since saturated soils yield lower backscatter at off-nadir angles than non-saturated (but wet) soils.

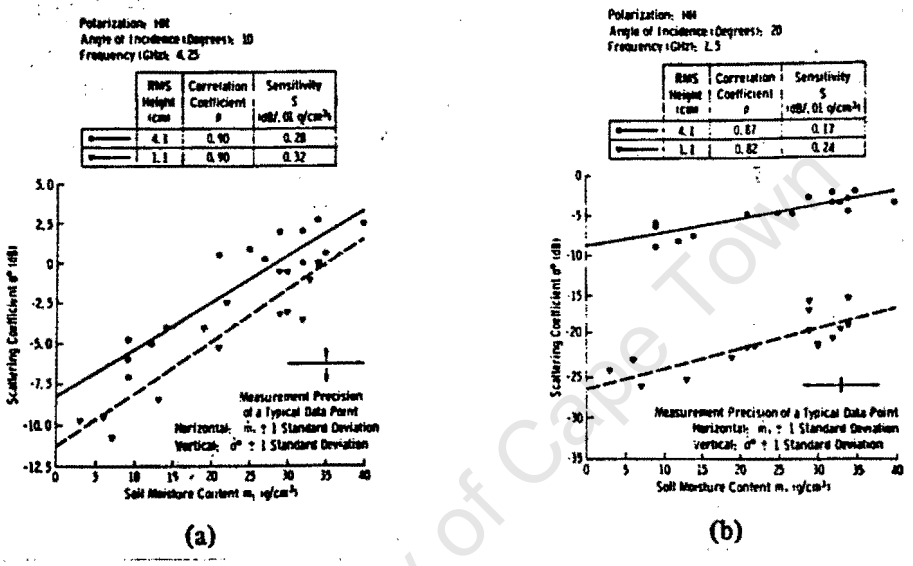

Figure 6.2: A comparison of the backscatter response σ° to volumetric moisture m_1 (i.e. moisture at a depth of 1 cm) for a smooth and rough surface at (a) $\theta = 10°$, $f = 4.25$ GHz and (b) $\theta = 20°$, $f = 1.5$ GHz. (Ulaby [92, p291])

To determine soil moisture theoretically, the backscatter measured by the radar is used to infer, via the surface scattering models (see Chapter 2), the dielectric constant which is in turn a measure of the soil water content. It has been shown (see Chapter 3) that soil moisture content is one of several factors (soil type, soil density and soil temperature) which influence the soil dielectric constant. Fortunately, soil moisture is by far the dominant factor. Ulaby [92] investigated the effect of soil type on radar backscatter and found that the sensitivity (first derivative of Equation 6.2) was higher for silt loam ($0.33\ dB/0.01g/cm^3$) than clay ($0.22\ dB/0.01g/cm^3$). The effects of soil density are largely accounted for by expressing the moisture on a volumetric basis.

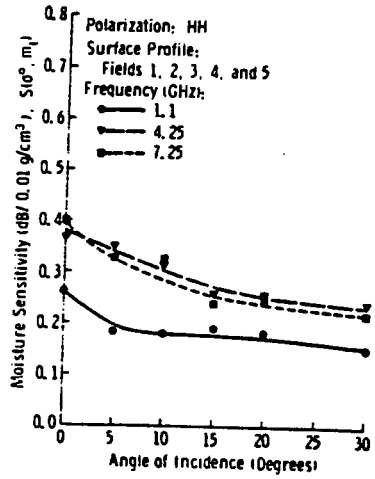

Figure 6.3: A graph showing the variation of moisture sensitivity $S(\sigma^\circ, m_1)$ as a function of incidence angle θ at three frequencies. (Ulaby [92, p293])

6.1.2 Local terrain slope effects

Since radar backscatter is influenced by the local angle of incidence, the local terrain slope is a possible source of error. Note the difference between the *angle of incidence* and the *local angle of incidence*. The incidence angle (also called look angle) is defined as the angle between the radar beam boresight direction and nadir. Whereas the local incidence angle is defined as the angle between the surface normal vector and the look vector which is the vector pointing from the ground towards the radar platform. The local incidence angle at any point in the image is equal to the incidence angle if and only if the ground is perfectly horizontal. Thus, a sloping terrain would modulate the radar backscatter which, if not corrected for, cause errors in the soil moisture retrieval. In principle, digital elevation models (see Chapter 8) can be used to determine the terrain slope and enable correction of the measured backscatter values prior to moisture retrieval. However, no such application could be found in the literature.

The effect of a variable local angle of incidence can be inferred from Figure 6.4 which shows the angular behaviour of backscatter σ° for five non-vegetated soil surfaces. The variation of σ° with incidence angle is greatest for smooth surfaces and this variation decreases as the surfaces become rougher. Thus, the moisture measurement uncertainty introduced by unknown topographic relief is larger for smooth surfaces than rough soil surfaces. Since roughness is a function of frequency, any surface can be made rougher by increasing the frequency. Thus, the influence of unknown topographic relief can be minimized by using higher frequencies. The effects of unknown topographic relief can also be minimized by cross-polarization since the angular dependence of the cross-polarized return is far less than that for like-polarization.

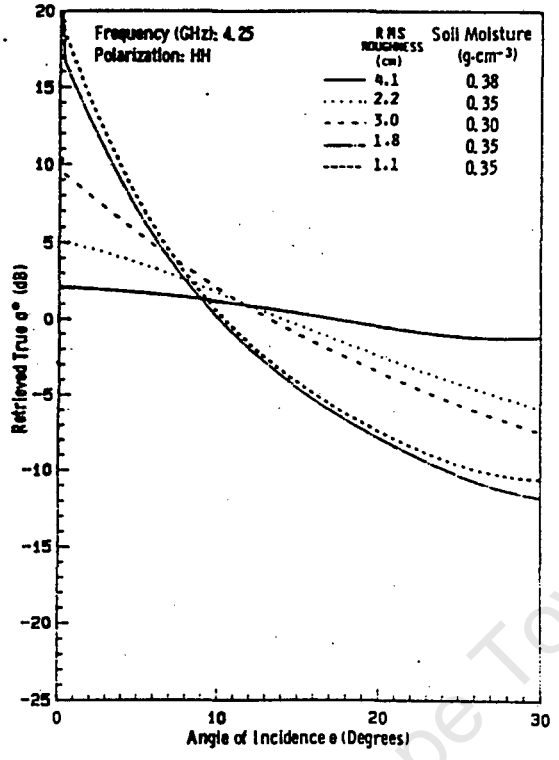

Figure 6.4: A graph showing the variation of radar backscatter $\sigma°$ as a function of incidence angle for five soil surfaces with rms ranging from 1.1 to 4.1 cm. (Dobson [19, p28])

6.1.3 Random surface roughness effects

To relate radar backscatter to soil permittivity and hence soil moisture requires the effect of the surface roughness to be minimized. The influence of random surface roughness is minimized by careful choice of the radar incidence angle. This is evident in Figures 6.4 and 6.5 which clearly show that at approximately 10° the roughness induced backscatter variation is minimized. A similar conclusion is reached using surface scattering models [6, 19].

Beaudoin [6] obtained good agreement when modelling the variation of $\sigma°$ as a function of rms height and incidence angle. For slightly rough surfaces (σ = 0.5 cm), the backscatter difference between 45° and 65° is 10 dB, whereas for rough surfaces (σ = 3.5 cm), the difference is 3 dB. The minimum backscatter variation of 2 dB which occurs at the optimum incidence angle is relatively large. Thus, even within the optimum angular range (5° to 15°), the roughness effects can be a significant source of error.

As shown above, minimizing the roughness effect by operating at the optimum imaging geometry is only partially successful. Using an imaging radar capable

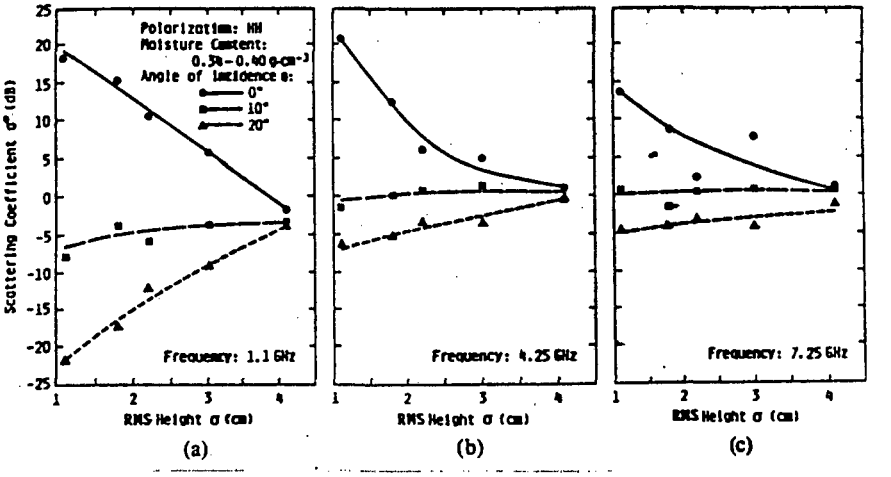

Figure 6.5: A graph showing the variation of radar backscatter $\sigma°$ as a function of surface rms σ for three incidence angles (0°, 10° and 20°) and frequencies (1.1, 4.25 and 7.25 GHz). (Dobson [19, p29])

of multipolarization or multifrequency operation, the roughness and permittivity (and hence soil moisture) can be simultaneously measured [19]. Since radar roughness is dependent on the transmitted frequency, changing the frequency will change the amount of backscatter measured by the radar. Hence, when transmitting at two frequencies, the scattering models (see Chapter 2) reduce to two equations in two unknowns, which can be solved. Similarly, using the same frequency transmitted at two polarizations (HH and VV), the surface roughness and the desired soil moisture content can be simultaneously determined. The success of the method depends on the accuracy with which the radar backscatter can be modelled. The inversion of an empirical model [71] has been used to retrieve the soil moisture content and surface roughness of bare soil from multipolarized radar observations.

The soil moisture can also be estimated via a change-detection approach because the surface roughness varies slowly with time for agricultural fields in the absence of tillage operations.

6.1.4 Periodic row and directional effects

Agricultural crops are generally planted in parallel rows which result in the air-soil interface exhibiting the same periodic structure. This periodic row structure (ridge/furrow) influences the radar backscatter and must be compensated for when inferring soil moisture. This problem can be overcome if the dimensions of the drainage and/or tillage patterns are known. This was demonstrated by

Beaudoin [6] and Ulaby [97] who derived formulas to account for these effects.

Firstly, a formula (Equation 6.3) is needed to calculate the local incidence angle θ_l which is a function of the row structure induced slopes $R'(y)$, incidence angle θ and radar look angle β. When the radar illuminates a field perpendicular to the field row direction, then $\beta = 90°$. The local incidence angle is given by [6, p890]

$$\cos\theta_l(y) = \frac{R'(y)\sin\theta\sin\beta + \cos\theta}{\sqrt{1 + R'(y)^2}} \tag{6.3}$$

where $R(y)$ is the function used to describe the row structure, $R'(y)$ is the first derivative of $R(y)$, and y is the distance along the image range direction. The backscatter from each differential segment dy is computed with the appropriate basic scattering model. Since the backscatter coefficient $\sigma°$ of a resolution cell is equal to the radar cross section of the cell σ normalized by the physical cross-sectional area of the cell A, the backscatter $\sigma°$ can be determined by integrating across one spatial period T instead of the whole resolution cell dimension. The surface backscatter is given by [6, p890]

$$\sigma°(\theta) = \frac{1}{T}\int_0^T \sigma°(\theta_l)\sec(\alpha)\, dy \tag{6.4}$$

where

$$\alpha(y) = \arctan(R'(y)). \tag{6.5}$$

The above equations predict the backscatter when the radar look angle β is known and is constant for a particular field. However, contour farming and some irrigation practices (such as centre-pivot irrigation systems) result in a variable radar look angle. In such cases, the radar parameters (incidence angle and frequency) are chosen to minimize the effect of periodic row structure. To investigate the effects of periodic row structure on $\sigma°$, the look direction modulation function $M(dB)$ is used. The modulation function is given by

$$M(dB) = \sigma°_{\parallel}(dB) - \sigma°_{\perp}(dB) \tag{6.6}$$

where $\sigma°_{\parallel}$ and $\sigma°_{\perp}$ is the backscatter observed parallel and perpendicular to the row direction, respectively.

$M(dB)$ behaves as follows :

1. $M(dB)$ is greatest for fields having the least random roughness and decreases rapidly as the surface becomes radar rough. For like-polarized configuration (HH and VV), $M(dB)$ decreases with frequency from as high as 10 dB at 1.1 GHz to near 0 dB at 4 GHz, and remains near 0 dB for further frequency increases [94].

2. $M(dB)$ has a local maximum for local incidence angles approaching 0°. Such small local incidence angles cause specular reflection from the furrow slopes. The radar incidence angle at which this occurs is determined by the tillage practices. Typically, the local maximum occurs for incidence angles ranging from 25° to 40° [6, 19].

3. The cross-polarized scattering coefficient is independent of look direction at all angles and frequencies [94]. Row direction effects are typically found to be smaller than 2 dB [19]. Although the cross-polarized configuration appears superior because of its row-direction independence, cross-polarized backscatter is usually 10 to 20 dB lower than the like-polarized configuration.

6.1.5 Optimum parameters

The optimum soil moisture mapping parameters (frequency, polarization and angle of incidence) are chosen to maximize the sensitivity to soil moisture and simultaneously minimize the effects of random surface roughness, periodic row effects and vegetation canopies.

To determine the optimum parameters, the correlation coefficient $\rho(\sigma^\circ, m_1)$ was used as an indication of moisture retrieval accuracy. Figure 6.6 shows the correlation coefficient $\rho(\sigma^\circ, m_1)$ as a function of incidence angle for three frequencies (1.1 GHz, 4.25 GHz and 7.25 GHz). The correlation function has a local maximum for incidence angles ranging from approximately 7° to 17° for both HH and HV polarization configurations. In addition, Figure 6.6 also shows the optimum frequency to be 4.25 GHz ($\theta = 10°$).

The optimum parameters for maximizing the sensitivity to soil moisture can be inferred from Figure 6.3. The sensitivity is maximum at nadir and decreases with increasing incidence angle θ. Since the spatial resolution of a side-looking imaging radar (utilizing pulse width to attain high resolution in the range dimension) degrades rapidly as θ approaches nadir, the lowest θ is limited by the radar hardware but is typically greater than 5°. Superimposing the maximum sensitivity requirement on the maximum correlation coefficient requirement (discussed above), the optimum θ ranges from approximately 7° to 15°. Also, the sensitivity is consistently greatest at 4.25 GHz which is also the frequency at which the correlation coefficient (discussed above) is highest.

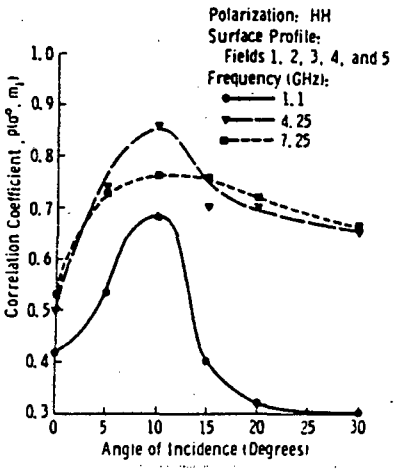

Figure 6.6: A graph showing the correlation coefficient $\rho(\sigma^\circ, m_1)$ as a function of incidence angle θ for three frequencies (1.1, 4.25 and 7.25 GHz). (Ulaby [92, p293])

Ulaby [94] showed that moisture sensitivity in the presence of vegetation (corn, soyabeans and milo) decreased rapidly with increase in frequency and incidence angle. Therefore, to maintain a reasonable level of sensitivity, the frequency should be less than 6 GHz, and incidence angles less than 20°.

The optimum parameters for minimizing the effects of random and periodic roughness is discussed in Section 6.1.3 and 6.1.4, respectively. The random roughness effect is minimized by an incidence angle of approximately 10° whereas the periodic roughness and row directional effects are maximized by incidence angles between 25° and 40°.

Although cross-polarization is far less sensitive to crop directional effects than like-polarization, the backscatter power difference ($\approx$ 15 dB) makes cross-polarization impractical.

In conclusion, the optimum radar parameters for near-surface soil moisture estimation is :

- incidence angle : 10°,
- frequency : 4 GHz, and
- polarization : HH or VV.

6.2 Vegetation type discrimination

The section contains the results of an investigation into the feasibility of vegetation type discrimination, particularly for crop type distribution mapping.

6.2.1 Principles of operation

To distinguish between two crops in a radar image requires that the backscatter from these crops differ in intensity. This backscatter intensity is influenced by vegetation parameters such as the canopy density (i.e. the number of trees/plants per square metre), the tree/plant dimensions (i.e. height, branch diameter, branch geometry) and the moisture content of leaves and branches. Unfortunately, the measured backscatter is also greatly influenced by the soil moisture and roughness. Thus, successful vegetation mapping depends on the degree to which the effect of the soil moisture can be minimized. As in other applications, the imaging parameters are manipulated to minimize the undesired effects.

Empirical observations [20] have shown that the average backscatter of an agricultural field can be used to identify the vegetation type. This is evident in Figure 6.7 which shows a histogram as a function of the average backscatter for 400 agricultural fields within a 20 km $\times$ 20 km test site in Illinois, USA. In spite of the variety of vegetation grown in the test site region, three backscatter distribution emerged with only two distributions namely, corn and short vegetation being well separated. This result is in no way surprising since the vegetation of the short vegetation group (soyabeans, cut soyabeans, alfalfa, clover and grass) would appear identical at the SIR-B operating frequency (1.2 GHz). At this frequency, the microwave attenuation of the short vegetation canopy is relatively low which implies that the observed backscatter is largely determine by the moisture and roughness of the soil.

Although the average backscatter of the corn crop shown in Figure 6.7 is approximately -8 dB, experimentation [19] has shown that this value is dependent on the development stage of the crop. The backscatter dependence on crop development can be inferred from Figure 6.8 which shows the attenuation of three crops (wheat, corn and soyabeans) over the period from crop emergence to crop harvest. Note the frequency induced differences in magnitude and curve shape between Figures 6.8a and 6.8b. Higher frequencies result in greater volume scattering loss in the crop canopy which reduces the effect of soil on the total backscatter.

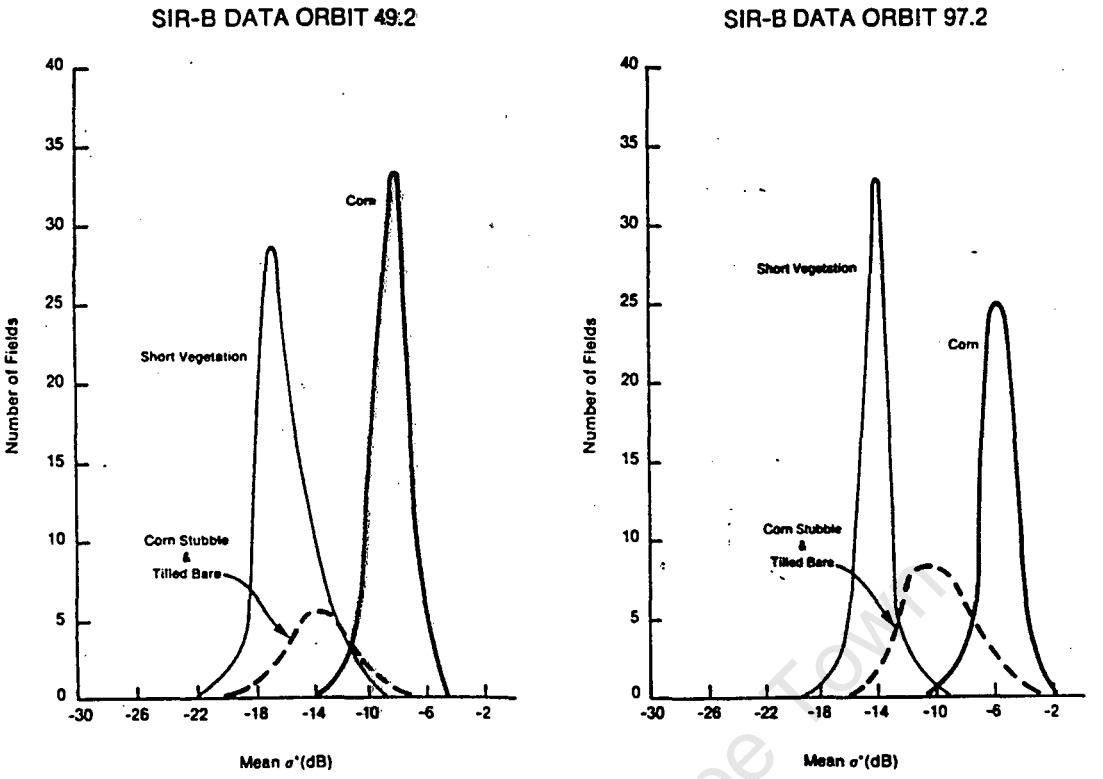

Figure 6.7: Distribution of average SIR-B backscatter response to agricultural fields at an incidence angle of 30°. The short vegetation group includes: soyabeans, cut soyabeans, alfalfa, clover and grass. (Dobson [20, p521])

6.2.2 Optimum parameters

The optimum radar parameters for vegetation mapping are chosen to minimize the influence of soil moisture. Ulaby [91] show that the soil moisture influence is minimized by using larger incidence angles and higher frequencies. This is evident in Figure 6.9 which shows the backscatter as a function of frequency for two incidence angles (0° and 30°) and two soil moisture values (8.3% and 26.8%). Comparison of the frequency response at 0° and 30° incidence indicates that the backscatter is less sensitive to soil moisture at the larger incidence angle. Also, the difference between the backscatter at low and high soil moisture conditions decrease as the frequency is increased. At 7.8 GHz, the backscatter at both incidence angles is identical which implies complete insensitivity to soil moisture.

The choice of optimum polarization (HH, HV, VH or VV) is not clear. Work by Ulaby [91] suggests that VV and cross-polarization components (HV and VH) exhibit greater sensitivity to crop type than HH. However, the choice of optimum polarization has become obsolete since polarimetric SAR is rapidly becoming the norm. A polarimetric SAR (single frequency, multi-polarization) produces radar image data simultaneously in four linear polarizations (HH, VV, VH, HV) which

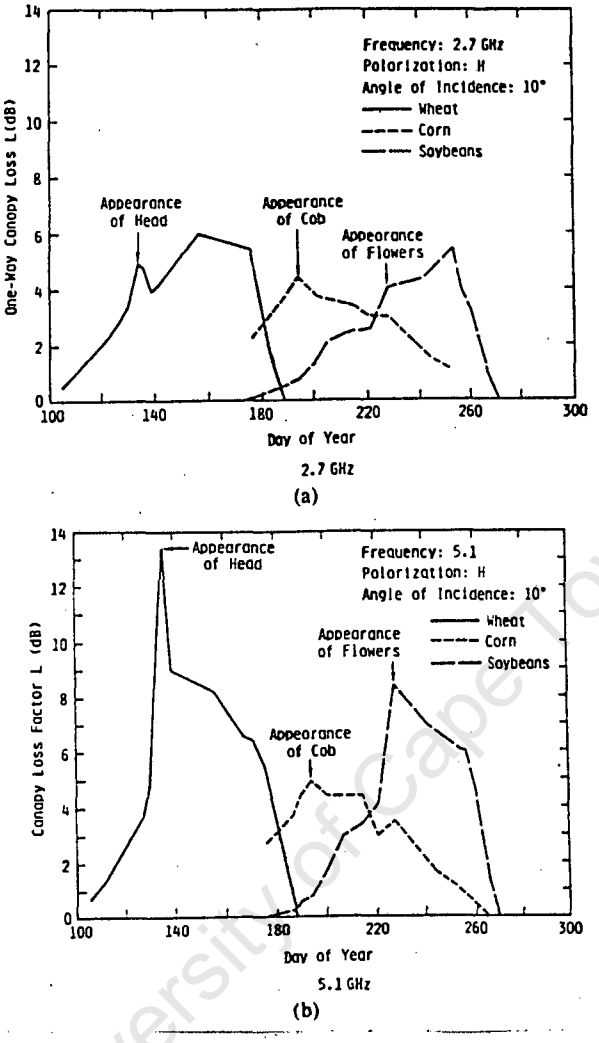

Figure 6.8: Comparison of crop attenuation for Wheat, Corn and soyabeans at (a) 2.7 GHz and (b) 5.1 GHz. (Dobson [19, p32])

has enabled more information to be extracted from the radar image.

Evans [33] generated a colour composite using three polarizations (HH = red, VV = green, VH = blue) to display the information content of polarimetric images. The colour of a local area in the composite image indicates which polarization (HH, VV or VH) is dominant in that area. For example, white indicates strong backscatter at all polarizations whereas bright pink indicates a slightly higher relative return at HH. Evans [33] used this technique for mapping vegetation types of a forested area in South Carolina, USA. The forest cover characteristics are discriminated by polarization responses that reflect the density and structure of the canopy, and the presence or absence of standing water beneath the canopy.

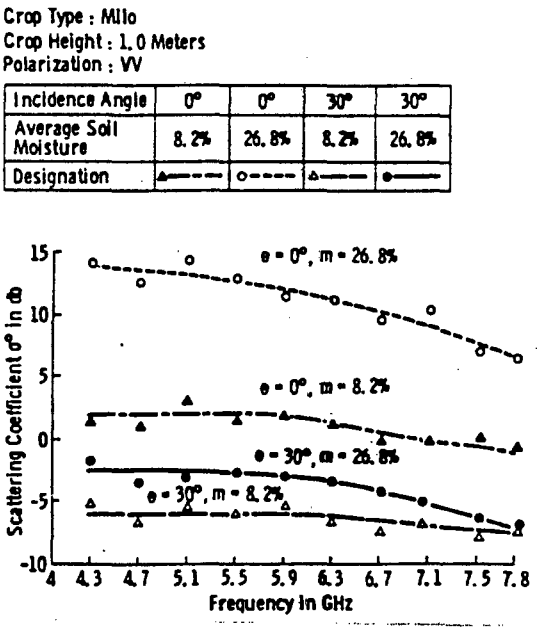

Figure 6.9: The spectral response (4-8 GHz) of milo at 0° and 30° for low and high soil moisture conditions. (Ulaby [91, p40])

Figure 6.10 shows the different backscatter values (expressed in mean image Digital Number) of four forest units at three different polarizations (HH, VH and VV). Note that each of the curves is unique and will thus map to a unique colour in the composite image thus making possible the identification of the forest unit. As an example, the Savannah River swamp area is denoted by a pale yellow colour in the composite image which indicates relatively high backscatter at all polarizations with the cross-polarization backscatter being slightly less than like-polarization backscatter values. The polarization signature (*Curve a*) of the Savannah River swamp is illustrated graphically in Figure 6.10. Similarly, the polarization signature of dense pine plantations (*Curve c*) is denoted by blue tones in the composite image because of the relatively strong VH backscatter.

Van Zyl [101] implemented an unsupervised classification algorithm for polarimetric SAR data. The backscatter of each pixel in the image is classified as being caused by an odd, even or diffuse number of reflections which are determined by examination of the Stokes scattering operator (see Chapter 4). The algorithm was applied to a forested area near Moosehead Lake, Maine, USA. This area consists of forests managed by a timber company, thus clear-cut areas of various regrowth ages are found in close proximity to unharvested tree stands. The results show that clear-cut areas are classified as odd number of reflections, while the forested areas are generally classified as a combination even number of reflections and areas with a large amount of diffuse scattering. The tree trunks and ground of forested areas form corner reflectors which cause double bounce

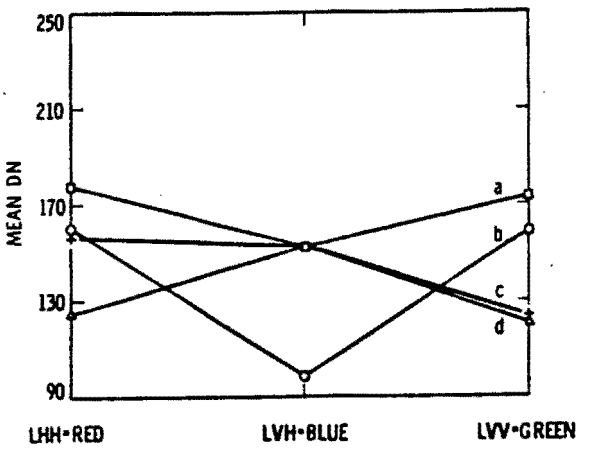

Figure 6.10: Curves showing the colour mapping of a polarimetric image for forest units in the Savannah River Plant area, USA. *Curve a:* Savannah River Swamp. *Curve b:* Pen Branch Delta. *Curve c:* Dense pine forest. *Curve d:* Open pine plantations with grassy understory. (Evans [33, p256])

(or an even number of reflections), whereas in the clear-cut areas, the vegetation is mostly shrub like which give rise to single bounce (or an odd number of reflections).

Using a technique known as polarization synthesis (see Chapter 4), Evans [35] showed that the polarization can be chosen to maximize the contrast between the forested areas and clear-cut areas in a polarimetric image of Moosehead Lake, Maine, USA. Since the forested areas have high coefficients of variation (see Chapter 4), most of the backscattered energy is unpolarized whereas for clear-cut areas, the coefficient of variation is relatively low indicating that only a small fraction of the backscattered energy is unpolarized. Therefore, to emphasize the contrast between forested and clear-cut areas, the unpolarized part of the backscatter should be used. Evans [35] showed that a polarization with ellipticity angle 0° and ellipse orientation angle 80° maximizes the contrast between forested and clear-cut areas.

6.2.3 Vegetation backscatter modelling

Predicting the backscatter from vegetation has always been difficult due mainly to the great diversity in vegetation cover. In addition, the backscatter from a vegetation canopy usually includes contributions due to volume scattering in the canopy itself, surface scattering from the underlying ground surface and multiple interactions involving both the canopy volume and the ground surface. Thus, an accurate backscatter model has taken many years to develop.

The Michigan Microwave Canopy Scattering model (MIMICS) [99] is based on a first-order solution to the radiative-transfer equation for a tree canopy comprising a crown layer, a trunk layer and a rough-surface ground boundary. Although the model is reported to work well [18], the model requires very many input parameters, some of which are difficult to determine. Listed in Table 6.1 are some of the required parameters.

Table 6.1: Input parameters of the MIMICS vegetation backscatter model. (Ulaby [99, 1228])

parameter	units
canopy density	tree m^{-2}
crown thickness	m
leaf density	m^{-3}
leaf moisture	g cm^{-3}
leaf diameter	cm
leaf thickness	cm
soil r.m.s. height	cm
soil correlation length	cm
soil moisture	cm^3 cm^{-3}
soil type	e.g. silty clay
trunk height	m
trunk diameter	cm
trunk moisture	g cm^{-3}
branch density	m^{-3}
branch length	m
branch diameter	cm
branch moisture	g cm^{-3}

In addition to the input parameters listed in Table 6.1, the branch geometry needs to be determined. This involves finding the average angle between vertical (z) and the branch axis as well as the average angle between the vertical (z) and trunk axis. Although this model agrees with experimental data to within 1 dB, it is difficult to use, it is computationally expensive and only works for continuous canopies.

Chapter 7

Sea surface imaging

The aim of this chapter is to highlight the sea surface imaging capability of Synthetic Aperture Radars (SAR). This imaging capability is demonstrated with two applications namely, detection and monitoring of oil spills on the sea surface, and detection of fish shoals.

The chapter starts with a discussion on Bragg scattering as this phenomenon is able to account for the backscatter dependence on sea surface characteristics. This is followed by a discussion of oil spill monitoring and fish shoal detection. Lastly, the optimum parameters for both applications are discussed.

7.1 Bragg scattering

Bragg scattering or Bragg resonance is a theory which accounts for the relatively high backscatter at incidence angles greater than 30°. In this theory, the backscatter is primarily influenced by resonant components in the sea surface roughness spectrum. Put simply, the backscatter is determined by the wavelength of the ocean waves and/or surface ripples. The relationship between surface wavelength L and radar wavelength λ is given by

$$\frac{2L}{\lambda}\sin\theta = n \tag{7.1}$$

where n is a positive integer and θ is the incidence angle measured from nadir. Thus, the Bragg resonance condition predicts that an X- and L-band SAR imaging the ocean at 45° incidence angle responds to ocean waves that are 2.2 cm and 17 cm in wavelength, respectively.

Analysis of the roughness spectrum of the ocean surface shows that at imaging radars frequencies, the predominant backscatter mechanism at incidence angles

larger than 20° is Bragg scattering from short gravity waves and capillary waves (wavelength in the range from 1 to 40 cm). These waves are strongly dependent on the local wind speed and direction since they are generated as a result of resonant coupling between the turbulent fluctuations in the air and water surface. As the wind speed is increased, the first waves that are generated by the coupling mechanism are the 1.7 cm waves [28]. This coupling mechanism is influenced by the surface tension thus, objects on the ocean surface which modify the surface tension are, in principle, detectable. This is the basis of the two applications discussed in this chapter.

7.2 Pollution monitoring

Detecting, monitoring and mapping of oil spills on the sea surface was shown by Rawson [77] to be feasible. As a result of Bragg scattering, imaging radars are very sensitive to the amplitude of ocean capillary waves. The presence of oil on the ocean surface significantly reduces the amplitude of capillary waves which in turn significantly reduces the radar backscatter from that surface. Thus, oil on the sea surface corresponds to dark patches, an example of which is shown in Figure 7.1.

Discriminating between oil and open ocean is not always easy. Since capillary waves are wind generated, oil on the sea surface can only be mapped in the presence of wind. (The correlation between wind speed and backscatter is sufficiently high for wind speed to be determined from scatterometers measurements.) For example, the absence of wind (which implies the absence of capillary waves) can create localized "wind slicks" whose lack of backscatter can result in dark areas resembling oil slicks [25]. On the other hand, emulsified oil (which is a byproduct of chemical dispersent) can have the opposite effect on the radar image during low wind conditions. Under such conditions, the emulsified oil appears as bright as the unpolluted sea surface [25, 77].

7.3 Fish monitoring

The ability of Side-Looking Airborne Radar (SLAR) to detect fish schools, particularly tuna, has been known for several years. However, the use of Synthetic Aperture Radar (SAR) for the surveillance of fish schools is relatively new. Since SAR has a finer resolution than SLAR, the possible applications can be extended beyond fish school monitoring. It will be shown that detection of fishing nets is also possible. The information contained in this section was obtained in a publication by Petit [74].

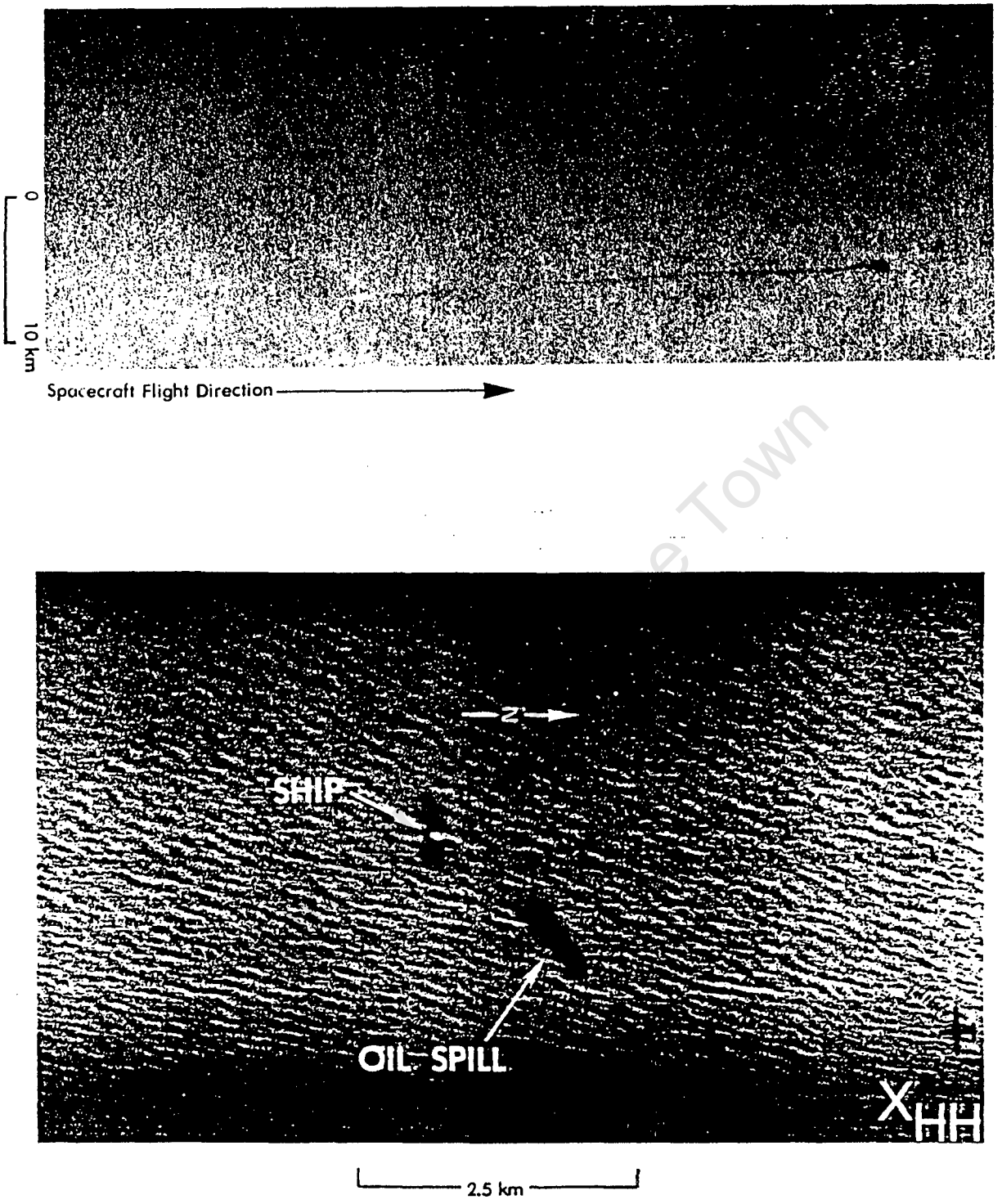

Figure 7.1: Seasat SAR image (top) of a ship-generated oil slick taken in August 1978 and ERIM/CCRS airborne X-band SAR image (bottom) of an oil spill off the east coast of the United States. (Kasischke [54, p3-38])

The feasibility of tuna monitoring was demonstrated by Petit [74] using E-SAR images of the Mediterranean sea. (E-SAR is a high resolution radar made by the German aerospace agency, DRL.) As in the previous sea surface imaging application, the radar backscatter is proportional to the sea surface roughness at scales predicted by the Bragg scattering phenomenon. For example, an X-band SAR is sensitive to roughness with a wavelength of approximately 3 cm.

Unlike marine mammals that constantly break the sea surface, tuna can usually be found just beneath the surface. When these tuna schools are reasonably compact, they cause a flattening of the surface. However, certain species such as the bluefin tuna break the water surface by repeatedly jumping out of the water. This behaviour, which is associated with feeding, produces a rough surface which results in greater backscatter and thus appears as a bright feature in the radar image. Similarly, net floats cause a roughening of the surface which enables the location of the nets to be mapped. This application is made possible by the fine resolution (2m $\times$ 2m) of the E-SAR sensor.

7.4 Optimum radar parameters

The optimum parameters for sea surface imaging applications are difficult to determine because of insufficient data on the subject. Nevertheless, an estimate of the optimum parameters (frequency and incidence angle) are gleaned from the limited literature on the topic.

Rawson [77] investigated the backscatter reduction caused by oil on the ocean surface at X- and L-band frequencies. He showed that the radar backscatter decreased by approximately 50% at X-band over the oil slick area, while the backscatter for the L-band data decreased approximately 25% over the same oil slick area. The reason for this difference is attributed to oil dampening the shorter X-band Bragg waves more than it did the L-band Bragg waves. Thus, higher frequencies appear to maximize the contrast between oil surfaces and open ocean.

The optimum incidence angle for oil mapping and fish school monitoring is not clear. Rawson [77] detected oil at incidence angles ranging from 36° to 43°. Similarly, Petit [74] monitored tuna shoals at an incidence angle of 35°. Unfortunately, both researchers did not investigate other incidence angles so an optimum incidence angle can not be inferred from their work.

Bragg resonance which is crucial to oil spill monitoring and fish detection, only works for incidence angles larger than about 30° [98]. Also, the backscattered power decreases as the incidence angle is increased which sets an upper limit on the incidence angle that can be used. Therefore, the optimum incidence angle is estimated to be larger than 30° and smaller than 45°.

The optimum polarization could not be determined as no literature could be found on this topic. The examples of oil spill imaging shown in Figure 7.1 were obtained using horizontal (HH) polarization whereas the tuna monitoring application used vertical (VV) polarization. Since no comparative measurements were taken, the optimum polarization could not be determined from these empirical results. However, polarization synthesis (see Chapter 4) not only proves that ocean backscatter exhibits Bragg resonance, but also shows that the ocean backscatter is maximum at vertical (VV) polarization [103, 113]. Thus, both HH and VV can be used but VV polarization is probably optimum.

Chapter 8

Digital Elevation Models

The aim of this chapter is to report on the results of an investigation into the uses of radar in remotely sensing topography. The ability to generate Digital Elevation Models (DEM) by extracting topographic information from Synthetic Aperture Radar (SAR) data is demonstrated by three methods namely, Shape-from-shading, Stereoscopic imaging and Interferometric SAR.

All three methods are discussed separately since the principles of operation and the optimum parameters are different for each case.

8.1 Shape-From-Shading

8.1.1 Principles of operation

Shape-from-shading (SFS) is a technique used to extract topographic information from radar images by inferring the terrain slope from the image pixel shades (grey tones). In general, radar backscatter is influenced by physical parameters (surface roughness and surface permittivity) and radar parameters (incidence angle, frequency and polarization). In SFS, the radar backscatter is assumed to be proportional to the local incidence angle which is a function of the terrain slope and incidence angle. Since the incidence angle is fixed by the sensor hardware, the slope of the terrain can be inferred from the backscatter. The DEM is then constructed from the terrain slope information.

The relationship between *incidence angle*, *local incidence angle* and *terrain slope* is graphically illustrated in Figure 8.1. The incidence angle θ (also known as the look angle) is defined as the angle between the radar beam boresight direction and nadir. Whereas, the local incidence angle θ_l is defined as the angle between

the surface Normal Vector N and the Look Vector L which is the vector pointing from the ground towards the radar platform.

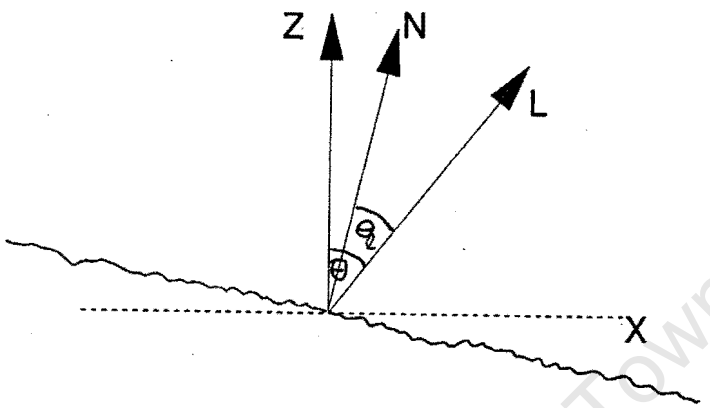

Figure 8.1: Schematic diagram illustrating the relationship between the incidence angle θ, local incidence angle θ_l and terrain slope

Since the incidence angle is fixed by the radar hardware, and the backscatter intensity is read from the pixel values of the radar image, the slope of the terrain corresponding to the pixel location can be determined provided an accurate model of radar backscatter σ° as a function of local incidence angle θ_l exists. Such models, both theoretical and empirical, are discussed in Chapter 2. However, the theoretical models require input parameters (surface roughness, surface correlation length and surface permittivity) which are not easily obtainable. In addition, the empirical models discussed in Chapter 2 lack the accuracy required in SFS applications. Therefore, locations (a few pixels in extent) of known slope which are also identifiable in the radar image, are used to obtain a function relating σ° to θ_l for the entire image [45]. This method, known as Radiometric Tie Point (RTP) calibration, yields the best backscatter model because unknown parameters such as surface roughness and permittivity are automatically included in the model.

Although radar backscatter is sensitive to local incidence angle, it should be noted that the local incidence angle θ_l consists of a range component θ_{lr} and azimuth component θ_{la}. Guindon [45] investigated these angles and found that the correlation coefficients ρ obtained by regression analysis of the image grey levels as a function of θ_l and θ_{lr} ranged from 0.61 to 0.74 and 0.83 to 0.84, respectively. Thus, the backscatter is most sensitive to the range component of

incidence angle which implies that adjacent range lines are independent of each other. This greatly simplifies the process of extracting the height information from the radar image. The sensitivity to the range component θ_{lr} arises from the imaging geometry of SARs.

Once the terrain slope information has been extracted from the radar image, the terrain elevation is obtained by some iterative method. Most techniques for DEM construction from terrain slope information starts with a point in the image of known height [45, 107] or a contour such as a lake or sea shore [12, 37]. From these points or contours of known height, the elevation of the entire image is calculated by an iterative method.

The method only works well in areas where the radar surface is homogeneous: In other words, the reflectivity does not change due to a change in surface roughness, only due to changes in local angle of incidence. These conditions apply for heavily vegetated areas such as forests, but not for barren regions. In the latter case, the dynamic range of the radar image is too limited for the very steep calibration curve.

8.1.2 Optimum parameters

This section discusses the choice of optimum parameters (frequency and incidence angle) for the extraction of Digital Elevation Models (DEM) from radar imagery using the shape-from-shading (SFS) technique.

Frequency

The accuracy of the SFS technique is largely determined by the accuracy of the model which relates backscatter σ° to local incidence angle θ_l. Figure 8.2 shows the variation of backscatter as a function of incidence angle for five surfaces ranging from smooth to rough. The backscatter response for the smooth surface initially drops very rapidly for small increases in the local incidence angle and soon reaches a minimum value which does not change substantially for large increases in incidence angle. This is typical of specular reflection which is associated with smooth surfaces. Therefore in SFS, inferring θ_l from σ° for smooth terrain is prone to error. However, for rough surfaces (see Figure 8.2) the relationship between backscatter (in dBs) and local incidence angle is approximately linear which is far less prone to error than backscatter responses for smooth surfaces. Since roughness is frequency dependent, using higher frequencies will yield better results. An exact frequency can only be determine if the surface roughness is known but C-band frequencies will probably be high enough.

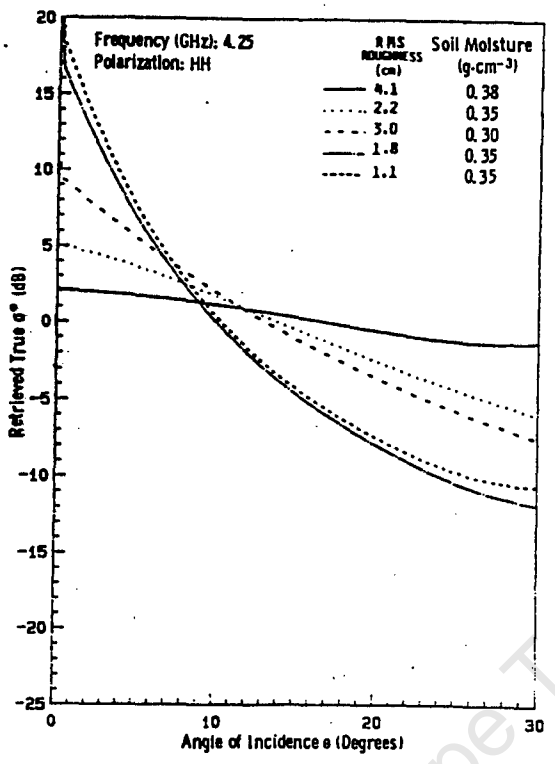

Figure 8.2: A graph showing the variation of radar backscatter σ° as a function of incidence angle for five surfaces with rms roughness ranging from 1.1 to 4.1 cm. (Dobson [19, p28])

Incidence Angle

In SFS, a combination of the imaging geometry and terrain slope results in a condition known as *layover*. Layover is the result of the terrain slope exceeding the maximum allowable slope. This is best illustrated with a diagram. Figure 8.3a shows the geometry of a radar with an incidence angle of 20° illuminating terrain with a forward slope (i.e. facing the radar) of 10°. The local incidence angle θ_l (i.e. the angle between the normal N and look L vectors) is 10°. If the forward slope of the terrain increases to 20°, the N and L vectors will coincide which implies θ_l is 0°. This is the maximum allowable terrain slope. Any further increase in terrain slope will result in layover. This is illustrated in Figure 8.3b which shows the geometry of a radar with an incidence angle of 20° illuminating terrain with a forward slope of 30° which results in a θ_l of 10°. Thus, a radar with an incidence angle of 20° is unable to distinguish between a forward terrain slope of 10° or 30°. This results in height estimation errors since the layover condition cannot be identified without *a priori* knowledge of the topography.

Increasing the incidence angle reduces the likelihood of layover but also increases the likelihood of shadowing and vice versa. For an incidence angle of 45°, layover

and shadowing are equally likely to occur. Thus, without *a priori* knowledge of the topography, the optimum incidence angle is 45°.

8.2 Stereoscopic imaging

8.2.1 Principles of operation

Stereoscopy is a technique whereby topographic information can be extracted from two overlapping images. The method is based on the apparent movement or parallax of features in the stereo image pair. The elevation of a feature is proportional to the observed parallax of the feature. The method requires two images of similar image quality, tone and texture, but different imaging geometry to present parallaxes for the height perception.

Radar stereo arrangements

There are in general two possible arrangements for obtaining the two images (stereo pair) required in stereoscopy namely, *same-side* and *opposite-side* geometry [59]. The latter is characterised by large intersection angles whereas the same-side geometry is characterised by small intersection angles. The intersection angle Ω is by definition the difference between the incidence angles of the stereo pair. In photographic stereo, larger intersection angles are usually associated with higher accuracy. However, large intersection angles cause problems, discussed in Section 8.2.2 which are unique to radar stereo imaging.

The two stereo pair arrangements shown in Figure 8.4 assumed that the two swaths comprising the stereo pair are parallel to each other. However, stereo pairs can be formed from non-parallel (crossing) swaths. Such an arrangement, known as *convergent* geometry, frequently occurs with satellite sensors as a result of the orbital mechanics. The SIR-A experiment demonstrated that DEMs could be extracted from stereo pairs with a convergence angle of 34° [59, p336].

Parallax detection

The same-side or opposite-side arrangements discussed above guarantees the existence of parallax in the stereo pair. This section discusses the methods used for measuring or detecting parallaxes from which the elevation is inferred. However, before detecting parallaxes in the stereo pair, the two images must be matched. Image matching is defined as the process by which corresponding points are found

in two overlapping images. These points or features are used as references when measuring the terrain induced parallax of other features.

Given a stereo pair, it is possible to use traditional manual interpretation techniques to obtain elevation. There are two general approaches namely, the *contour* method and the *profile* method. With the contour method, the stereo pair is adjusted in a viewer such that only objects at a given height will overlay perfectly. The interpreter then traces the path of perfect overlap. In the profile method, the spacing between the two images is adjusted until a given object overlaps perfectly. The height of the object is then obtained as a function of the spacing [75].

To avoid tedious manual parallax detection, several automatic detection techniques have been developed. Several of these techniques, as well as their suitability to computer implementation are discussed by Ramapriyan [75]. According to Leberl [59], the process of matching consists of first selecting a window of data (reference window) in the reference image and a large search area (search window) in the second image. A match function is computed for every possible offset of the reference window within the search window. Some match function criteria, typically the maximum or minimum value is used to determine which part of the search window is most similar to the reference window. Using large reference windows degrade the resolution of the DEM and is computationally expensive. Whereas, small reference windows use less information to find a match and is therefore more susceptible to noise problems.

Ramapriyan [75] used a method called Hierarchical Warp Stereo which overcomes the problems associated with reference window size selection. Initially, a large reference window (which implies low resolution) is used to obtain a rough estimate of the parallax. The reference window size is then decreased resulting in a better estimate of the parallax. The process is repeated until the desired resolution is reached.

8.2.2 Optimum parameters

The optimum stereo geometry is a compromise between two equally important criteria. Firstly, the two images forming the stereo pair must be very similar in image quality, terrain illumination, tone and texture so that the stereo pairs correlate well. The extent to which stereo images correlate is referred to as *stereo viewability* [59]. Secondly, the two images forming the stereo pair must be sufficiently different in geometry to present parallaxes for height perception. Since radar actively illuminates the terrain, significant differences in viewing geometry also imply illumination differences. Thus, good stereo from a geometric point of view contradicts good viewability.

The optimum stereo geometry (incidence angles and intersection angle) was in-

vestigated by Kaupp [55] and Leberl [60, 61]. Due to the lack of stereo pair images, Kaupp's [55] investigation used computer simulated radar imagery. His results indicate that the best stereo imaging is obtained with pairs created from different incidence angles having the same look-direction (i.e. same-side stereo pair arrangement). Generally, acceptable stereo was obtained for any pair having an intersection angle greater than about 15°.

Kaupp's [55] simulations also showed that optimum incidence angles were dependent on the relative terrain relief of the imaged scene. For moderately rough and mountainous terrain, an intersection angle of 30° formed by incidence angles of 70°/40° or 75°/45° produced the best results. For relatively flat terrain, an intersection angle of 40° formed by incidence angles of 60°/20° produced the best results. The use of opposite-side stereo was marginally acceptable for relatively flat terrain and unacceptable for moderate and high relief terrain.

Although opposite-side stereo provides superior intersection angles, the poor viewability resulting from very different illumination directions makes manual parallax detection difficult, and automatic parallax detection virtually impossible. The poor viewability of opposite-side stereo is evident in Figure 8.5. Differences in the illumination direction also causes problems in same-side stereo but the effects are considerably smaller than opposite-side stereo. Leberl [59] showed that the same-side geometry produced usable stereo pairs, even with intersection angles of up to 60°. Difficulties exist only when excessive layover (at 10° incidence angle) is combined with shadows (at 80° incidence angle).

Leberl [60, 61] used four overlapping SIR-B radar images to investigate the effect of intersection angle on accuracy. The incidence angles of the four overlapping images were 56°, 51°, 43° and 33° which formed six stereo pairs with intersection angles 5°, 8°, 10°, 13°, 18° and 23°. The results do *not* support the expectation that larger intersection angles translate into higher height accuracy. An analysis of the DEM accuracies obtained with SIR-B, led Leberl to conclude that as illumination angles differ more, the quality of the stereo fusion deteriorates and thereby sets off any gains achieved by better stereo geometry. An analysis of accuracies achieved with SAR sensors shows that the accuracies usually range from two to five times the range resolution [59, p401]. However, this has *not* been proved.

Domik (see Leberl [59, p335]) investigated the effect of squint angle on stereo viewability and found that the 'best' subjective stereo impressions, obtained in experiments with a number of test persons, were for incidence angles of 50°/70°, which corresponds to an intersection angle of 20°. Domik found that extracting DEMs from stereo pairs was feasible using images with squint angles less than 30°, assuming the 'best' 50°/70° stereo pair data.

To conclude: Only same-side stereo is feasible for extracting DEMs of a wide

range of terrain relief types. The optimum incidence angles and intersection angle are also dependent on the terrain relief. For relatively flat terrain, the incidence angles should range from about 20° to 60° with an intersection angle greater than about 30°. For relatively high relief terrain, the incidence angles should range from 40° to 70° with intersection angles ranging from 15° to 30°. Although not conclusively proved, higher DEM accuracy is obtained with higher SAR range resolution.

8.3 Interferometric SAR

8.3.1 Principles of operation

Interferometric SAR is a technique whereby topographic information can be extracted from SAR data. Unlike shape-from-shading and radar stereoscopy which use processed SAR data (i.e. images) for obtaining DEMs, Interferometric SAR (InSAR) extracts topographic information directly from raw SAR data. The interferometric technique can be implemented using one of two InSAR arrangements namely, one antenna on a platform known as Repeat-Pass interferometry [41, 62], or two antennas on a single platform [65, 111, 112]. The latter, which is better suited to airborne SAR implementation, is discussed first.

InSAR with two antennas

The geometry of a two-antenna-one-sensor interferometric SAR is shown in Figure 8.6. The two antennas, A_1 and A_2, separated by baseline distance B, are mounted on the same aircraft. Only one antenna, A_1 transmits but both antennas A_1 and A_2 receive the backscattered power. The phase difference between the received signals at A_1 and A_2 is used to determine the path length difference $(\rho - \rho')$ modulo the transmitted signal wavelength. Zebker [111] showed that the path length difference to the target $(\rho - \rho')$ and the range to the target ρ, given the baseline B and aircraft roll angle θ, is sufficient to calculate the height of the aircraft above the target. Since the height of the aircraft (above an absolute reference such as sea level) is known from onboard GPS equipment, the absolute target height is easily calculated.

A paper by Zebker [112] reports on modifications made to the NASA SAR to implement interferometric processing. This P-, L- and C-Band SAR can operate in polarimetric mode, but to implement TOPSAR, the C Band transceiver has been modified to receive from a spatially displaced antenna with the receiver normally used to receive the co-polar signal. The system has been measured to

produce statistical errors of the order of 2-4m, with systematic errors of 10-20m due to aircraft motion.

Since the height is measured modulo the radar wavelength, other inputs are required to determine whether the features under observation are upward or downward bulging. Most commonly, the interferometric image is overlaid with the normal intensity image to assist with this inference. This effectively results in an image very similar to a contour plot.

Repeat-Pass InSAR

In repeat-pass interferometry (also known as differential interferometry) the phase difference needed for extracting topographic information is obtained from two SAR swaths of the same scene, but imaged on separate occasions with similar (not identical) viewing geometry. The backscatter of the scene should not change significantly between the SAR passes since this would introduce errors in height estimation. Assuming that the above conditions are met, the phase difference between the complex images, C_1 and C_2 from two separate passes is not random but is related to the change in radar range from the antenna to the target [41].

The 'image' formed by the product of image C_1 and the complex conjugate of image C_2 is also a complex image referred to as an interferogram, which has a phase equal to the difference between those of the original images. In an interferogram, a 2π change in phase is referred to as a *fringe* which forms contour lines with a vertical separation of the order of the radar wavelength. The use of repeat-pass interferometry is limited by the problems associated with motion compensation and maintaining the desired baseline.

8.3.2 Optimum parameters

Zebker [112] investigated the effect of radar parameters on the accuracy of the DEM extracted from the radar data. He derived formulas (see Equation 8.1) which suggests that the height accuracy is optimized through minimization of phase errors, wavelength, and slant range and maximization of the baseline distance. However, the level of phase noise in the system increases with increasing baseline distance up to a critical baseline distance (see Equation 8.2) where the signals are no longer correlated and the effective signal to noise ratio is zero. Zebker [112] found that the optimum baseline distance is fairly broad, ranging from 0.2 to 0.8 of the critical baseline distance.

The error in height estimation σ_h is given by

$$\sigma_h = \frac{\lambda\rho}{2\pi B}[\sin\alpha - \cos\alpha\tan(\alpha-\theta)]\sigma_\phi \tag{8.1}$$

and the critical baseline B_c is given by

$$B_c = \frac{\lambda\rho}{R_y}\tan\theta \tag{8.2}$$

where

σ_h = standard deviation of the height,
σ_ϕ = standard deviation of the phase,
λ = radar wavelength,
ρ = slant range (distance) to the target,
B = baseline (i.e. the distance between the two antennas),
α = baseline angle,
θ = look angle (also known as the incidence angle), and
R_y = slant range resolution.

In InSAR, the choice of frequency is critical only when both antennas are mounted on the same platform. Since an aircraft wingspan is limited, the maximum baseline distance is also limited. Thus, under such circumstances, the frequency (wavelength) is chosen so that the optimum baseline requirements are satisfied. But, in repeat-pass InSAR, the flight paths are chosen so that the optimum baseline requirements are satisfied. However, a very high frequency may necessitate a very small baseline which could be impractical in terms of flight path control. The Canada Centre for Remote Sensing (CCRS) developed a interferometer which operates at C- and X-band. This repeat-pass interferometer requires a horizontal baseline of 40 m which, according to Gray [41], is extremely difficult *but not* impossible to implement under favourable conditions. Thus, the navigational equipment determines the upper frequency limit. For example, an aircraft using only conventional GPS will be restricted to a baseline of approximately 100 m, which implies an upper frequency limit of 3 GHz given an incidence angle of 45°, a target range of 10 km, and a slant range resolution of 10 m.

In addition to the radar parameters discussed above, the terrain type also affects the accuracy of the DEM extracted from the radar data. Hagberg [47] showed that the terrain slope is a major source of error in elevation retrieval since terrain with too large a slope causes phase aliasing which distorts the measurement. This effect increases when the baseline increases. When the terrain slope is so large that layover or shadowing occurs, the phase is either ambiguous or completely lost. Hagberg [47] developed formulas to determine the optimum baseline using

both radar and terrain parameters. However, determining the terrain parameters such as slope angle distribution, could be difficult. Thus, Zebker's formula (see Equation 8.2) should be used.

The incidence angle determines the slant range ρ which also influences the optimum baseline. However, incidence angle should be set so as to limit layover and shadowing, and the frequency set so as to optimize the baseline distance.

In conclusion: The frequency is chosen so that the baseline distance is optimum. Baseline distances are limited by aircraft dimensions when both antennas are mounted on the same platform, or navigational equipment accuracy when repeat-pass InSAR techniques are used.

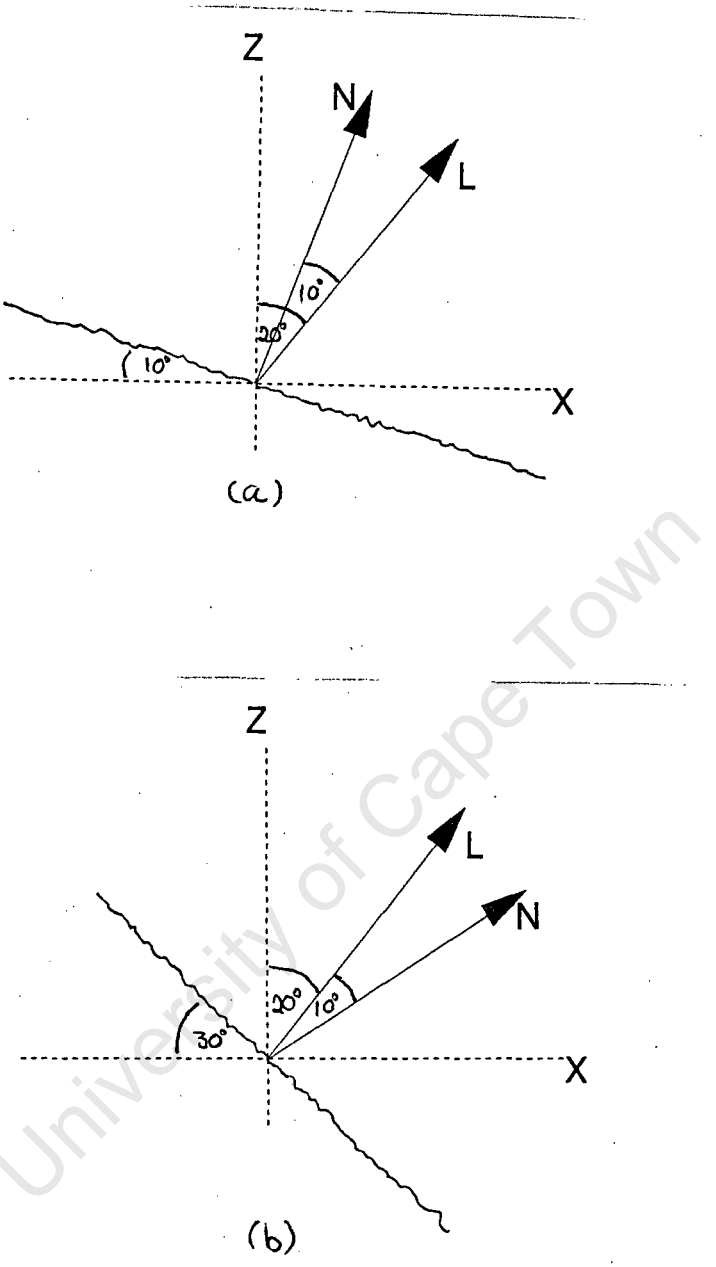

Figure 8.3: An illustration of (a) non-layover and (b) layover. Note that both terrain slopes of (a) 10° and (b) 30° result in the angle between the N and L vectors (i.e. local incidence angle) being 10°.

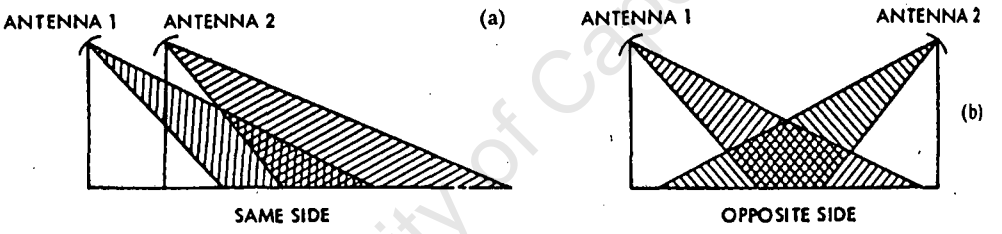

Figure 8.4: An illustration of (a) same-side and (b) opposite side radar stereo arrangements. (Leberl [59, p324])

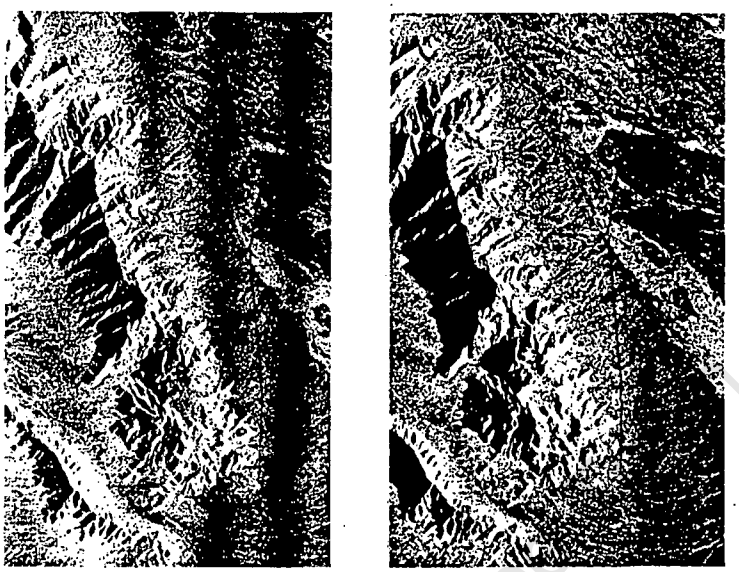

Aircraft radar, same-side stereo.

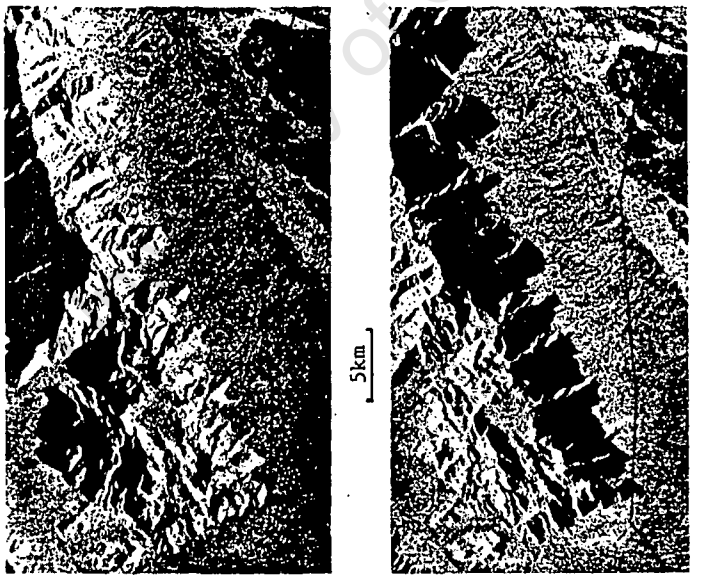

Aircraft radar, opposite-side stereo.

Figure 8.5: An example of same-side and opposite-side stereo pairs. (Leberl [59, p326])

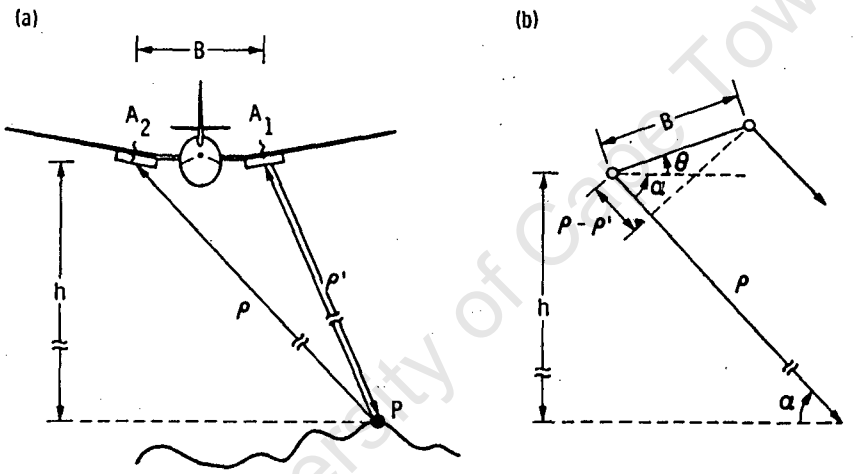

Figure 8.6: Schematic showing the observational geometry of a two-antenna-one-sensor interferometric SAR. (Zebker [111, p4994])

Chapter 9

Summary and Conclusions

The results of the investigation into imaging radar applications are intended as a reference for the proposed airborne Synthetic Aperture Radar campaign envisaged for 1994/5. The feasibility of each intended application has been established using theoretical models, simulations, and case studies reported in the literature. Since the emphasis is on planning an airborne campaign for South Africa, the investigation focussed on identifying optimum radar parameters for each application. A more detailed conclusion for each application is contained in the relevant chapter. This conclusion discusses some of the compromises made when selecting the imaging parameters for the proposed campaign.

Ideally, one radar sensor could be configured to have frequency and incidence angle ranges that would contain the optimum parameters for all the envisaged applications. In addition, this ideal radar sensor should be capable of multifrequency and multipolarized modes of operation. Unfortunately, a combination of financial and technical limitations made this ideal imaging radar unrealistic. Hence, some compromises had to be made which automatically implied implementing some applications with less than optimum imaging parameters. Listed below is a very brief summary of the optimum imaging parameters.

Applications favouring small incidence angles (i.e. $\theta <\approx 30°$) are :

- subsurface geological applications,
- soil moisture mapping, and
- lava flow mapping.

Applications favouring large incidence angles (i.e. $\theta >\approx 30°$) are :

- sedimentary rock type mapping,

- vegetation or crop type mapping,
- sea surface applications such as oil pollution monitoring, and
- digital elevation modelling, whether implemented using shape-from-shading, radar stereoscopy or interferometric SAR.

The optimum frequencies are :

- subsurface geological applications require very low frequencies (VHF-band) to minimize attenuation and maximize penetration depth,
- sedimentary rock type mapping requires L-band (possibly lower) frequencies,
- soil moisture mapping requires low C-band (4 GHz) frequencies,
- vegetation and crop type discrimination requires high C-band (8 GHz) frequencies, and
- sea surface mapping applications such as oil pollution monitoring requires X-band frequencies, and
- lava flow mapping requires Ku-band frequencies.

As for the optimum polarization, most applications use either horizontal transmit and receive (HH), or vertical transmit and receive (VV) polarizations. However, multipolarized imagery is far superior to any single polarized imagery as is demonstrated by Evans [33] and Van Zyl [103] (see Chapters 4, 5 and 6).

Unfortunately, the optimum parameters vary widely from application to application which makes choosing the parameters which will eventually be flown extremely difficult. An imaging radar that would be optimum for all of the applications previously listed is not feasible. For example, mounting antennas for VHF, L-, C-, X- and Ku-band operation is not feasible since the radiation patterns will interfere. In addition, a VHF antenna is physically large which limits the space for mounting other antennas. Hence only two frequencies will be implemented namely, VHF and X-band. For technical reasons the incidence angle will be restricted to angles larger than 40°. The proposed radar has a multipolarization capability which is in keeping with the present international trend of polarimetric imagery. Since the on-board navigational equipment has not yet been finalized, the repeat-pass interferometric capability of the proposed sensor could not be determined.

It is envisaged that imagery from the proposed campaign will enhance and not compete with existing satellite imagery. Since satellites presently in operation

use L-band (JERS-1) and C-band (ERS-1) frequencies, the VHF and X-band imagery is expected to complement existing systems. Also, VHF radars cannot be implemented from satellite platforms because the ionosphere reflects VHF-band signals which necessitate an airborne implementation. Remote sensing of the near-surface soil moisture content will not be implemented with the proposed airborne platform since the ERS-1 sensor is optimum for this application.

Appendix A

A soil classification system

This appendix has been included to define quantitatively the term "Soil Type" (Textural composition) which is used in Chapter 3.

The textural composition of soil is defined in terms of the percentages of Sand, Silt and Clay in the sample. The diameter of each individual particle determines whether the individual particle is classified as sand, silt or clay. Unfortunately, the American and International standards use different particle diameters for the sand-silt boundary. The International scale, illustrated in the Wentworth Grain Size Scale, is shown in Table A.1. The differences between the International Scale and the United States Department of Agriculture (USDA) Scale is shown in Figure A.1.

The textural composition of soil is defined in terms of the percentages of Sand, Silt and Clay in the sample. This definition of textural composition is illustrated in Figure A.2. Thus, for a soil to be classified as Sand, approximately 90% of the total sample must be composed of particles (grains) which satisfy the sand criterion, i.e. 90% of the particles have diameters greater than 0.05 mm (American System) or 0.02 mm (International System).

The number of particles per gram and the total particle surface area (in cm^2g^{-1}) associated with the soil particle diameters are given in Figure A.1. The surface area is important in determining the amount of *bound* water present in the soil which greatly affects the soil dielectric behaviour. Thus, high clay content soils would contain more *bound* water than sandy soils.

Limiting particle diameter					
mm	ϕ units		Size class		
2048	−11		Very large	Boulders	GRAVEL
1024	−10		Large		
512	− 9		Medium		
256	− 8		Small		
128	− 7		Large	Cobbles	
64	− 6		Small		
32	− 5		Very coarse	Pebbles	
16	− 4		Coarse		
8	− 3		Medium		
4	− 2		Fine		
2	− 1		Very fine	Granules	
1	0		Very coarse	Sand	
$^1/_2$	+ 1	500 μm	Coarse		
$^1/_4$	+ 2	250	Medium		
$^1/_8$	+ 3	125	Fine		
$^1/_{16}$	+ 4	62	Very fine		
$^1/_{32}$	+ 5	31	Very coarse	Silt	MUD
$^1/_{64}$	+ 6	16	Coarse		
$^1/_{128}$	+ 7	8	Medium		
$^1/_{256}$	+ 8	4	Fine		
$^1/_{512}$	+ 9	2	Very fine		
				Clay	

Table A.1: The Wentworth grain size scale showing the classification of sedimentary particle sizes. This system is the internationally accepted soil particle size classification. (Davis [17, p50])

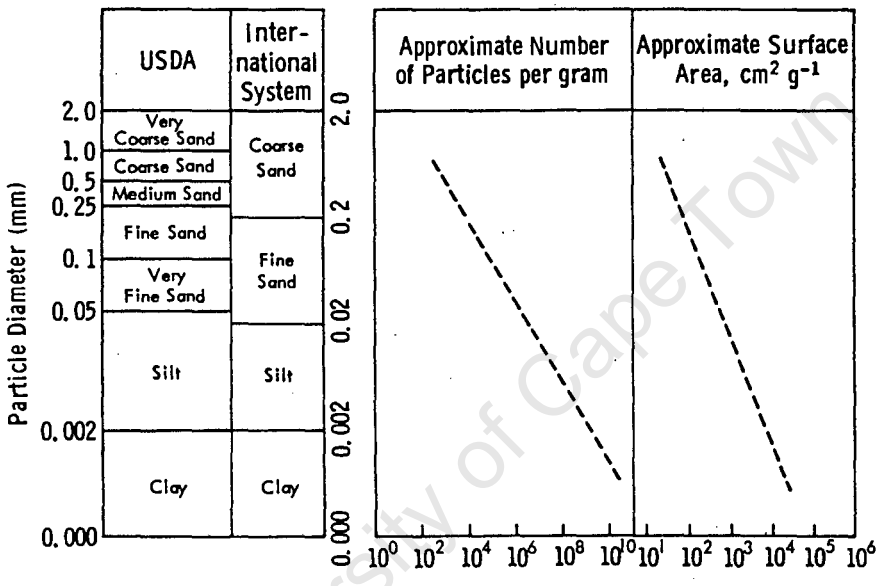

Figure A.1: Soil particle classification sizes. Note the difference between the USDA and International system with regard to the particle diameter at the sand-silt boundary. (Ulaby [98, p2088])

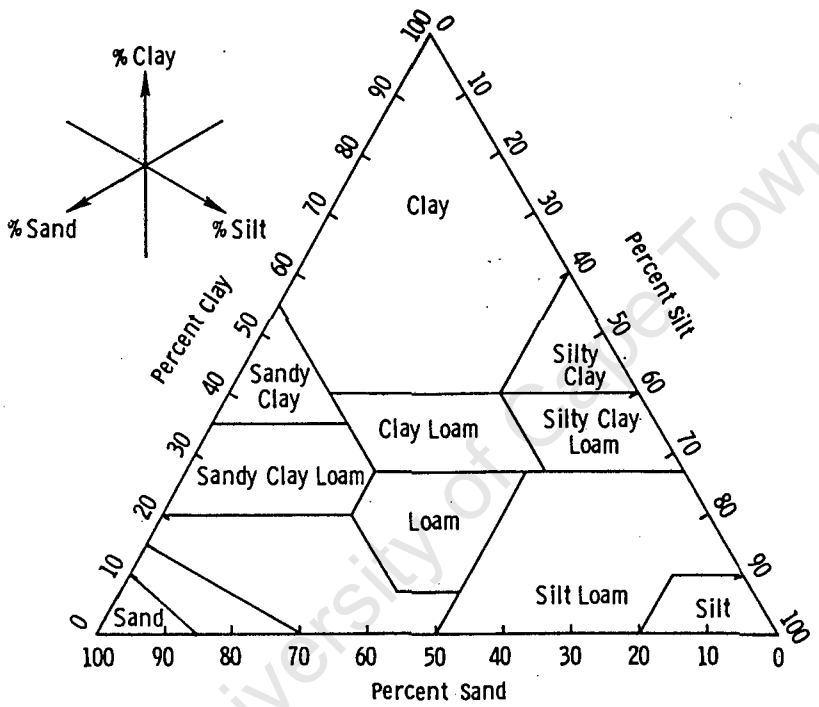

Figure A.2: The soil textural classification triangle. This classification triangle is based on the United States Department of Agriculture's particle size classification. (Ulaby [98, p2088])

Appendix B

The Geology of the Kalahari region

The information contained in this appendix was obtained in papers by Lancaster [57, 58] and Thomas [88], and Geological Survey booklets by Thomas [86] and Thomas [87]. The Kalahari region forms an extensive, mainly sand covered, plain in the interior of southern Africa. The altitude of this plain is 1000 to 1500 m. The region consists of extensive linear dune systems, pans and large river valleys which are today ephemerally flooded.

B.1 The climate of the Kalahari region

The southwestern parts of the Kalahari lie in a transition zone between areas of arid to hyper-arid climates to the north and southwest (i.e. Namib Desert) and the semi-arid climates to the north and east. The climate of the region is semi-arid to sub-arid, with an annual rainfall increasing from 150 mm in the south to 350 mm in the north (Lancaster [58, p368]). The effectiveness of this precipitation is limited as it occurs when the temperature and evaporation rates are highest.

B.2 The river systems

The ephemeral Nossob, Auob and Olifants rivers cross the region in well developed valleys which cut into the Precambrian or Palaeozoic rocks by up to 50 m in their middle reaches. These rivers originate in the highlands of Namibia. The Molopo amd Kuruman Rivers also traverse the area but originate on the edge of the

Highveld of South Africa. Flow in these rivers is ephemeral and flood discharges only reach the end point of the Molopo system after periods of exceptional rainfall (e.g. 1933 and 1974). The extent of the river system is shown in Figure B.1.

B.3 The dune systems

The southwestern Kalahari is dominated by linear dunes covering an area of approximately 150 km wide. These dunes have a spacing of 200-400 m and are 2-15 m high (Lancaster [58, p369]). Due to the prevailing wind direction, the dunes are aligned NW-SE as illustrated in Figure B.1. At the present time, all the dunes are vegetated to some extent, and only their crests are mobile.

A comprehensive discussion of the Kalahari dunes is contained in a paper by Thomas [88]. His work concentrated on the influence of vegetation on the mobility of the Kalahari dunes. He concluded that :

- There is sufficient evidence to suggest that the northern and eastern dune systems are relict aeolian landforms.
- The vegetation densities are sufficiently low on the crests of dunes in the Kalahari dune desert to permit significant aeolian activity to occur.
- Some linear dunes display greater aeolian activity than the average dunes. This can, in some cases, be attributed to the effects of overgrazing.

The aeolian origin of the sand dunes is important as they enable one the make certain assumptions about the sand grain size distribution. The red sand (Gordonian Formation) is made up of highly rounded quartz grains, uniformly about 0.5 mm in size, which according to Thomas [87, p13] is indicative of an aeolian origin. Research by Lancaster [57, p396] showed that the crests of the Kalahari dunes are well sorted, with sand grain sizes ranging from 0.37 to 0.62 mm. The size of the sand grains is one of the factors which determine the depth of microwave penetration.

B.4 The Kalahari pans

The Kalahari contains some of the largest concentration of pans in southern Africa. The pans occur where the Karoo Systems bedrock is close to the surface and the Kalahari sand cover is thin. The pans in the vicinity of the lower Molopo River contain less than 1 m of sandy sediments (Lancaster [58, p372]). These sediments were derived from invading linear dunes. The sediments overlie salt-weathered bedrock.

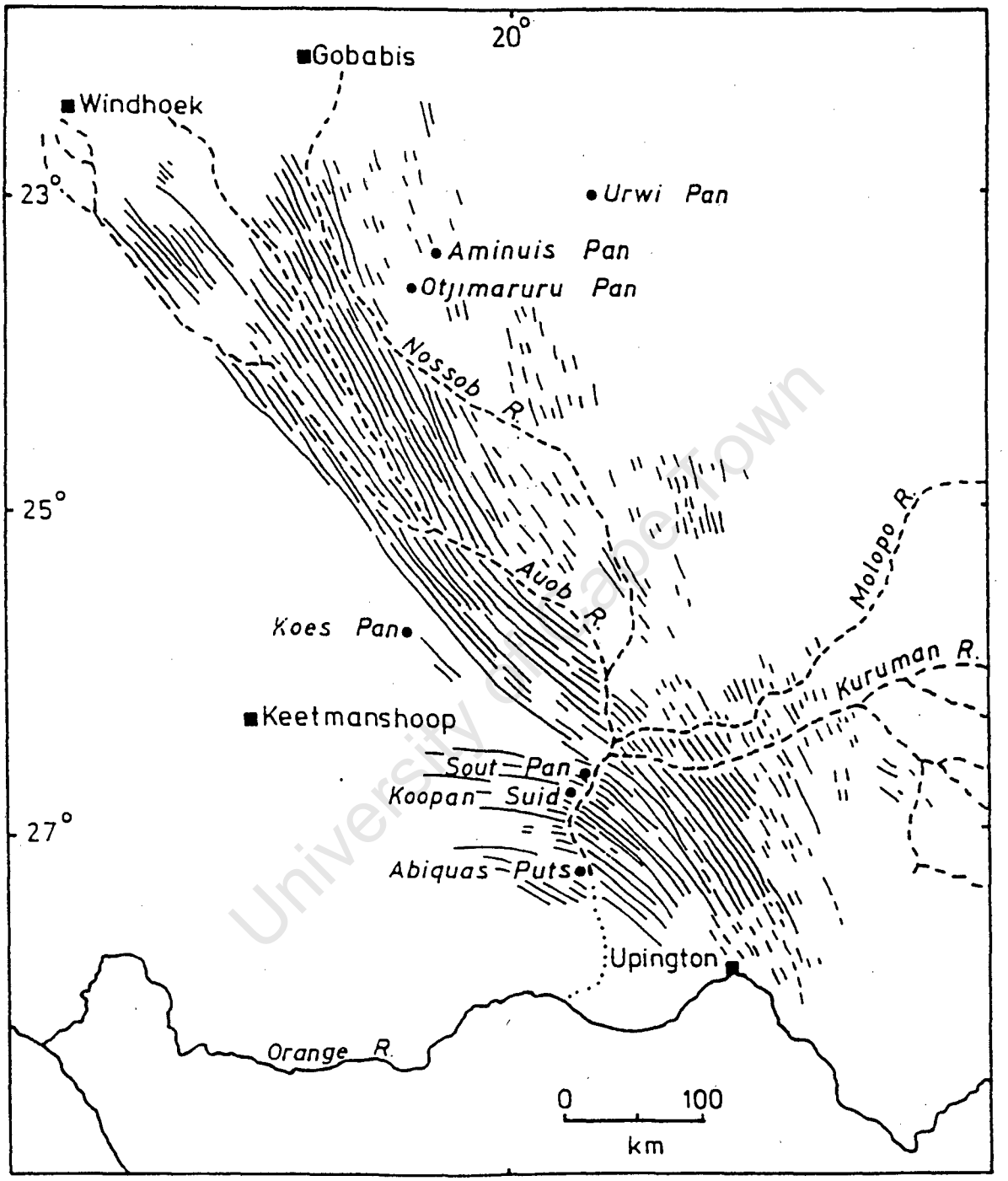

Figure B.1: The southern Kalahari showing the linear dune alignment and the ephemeral river system. (Lancaster [58, p369])

B.5 The subsurface geology of the southern Kalahari region

The above discussion concentrated on the Gordonian Formation (aeolian sand) which covers approximately 90% of the area. The incident radar signal is expected to penetrate this surface cover and reflect from a subsurface layer. Thus, the geology of the subsurface layers are discussed below. The information contained in this section was obtained in a booklet by Thomas [86].

The oldest rocks in the region are interpreted as belonging to the Olifantshoek Sequence. A small outcrop of the Groblershoop Formation can be found in the bed of the Kuruman River. Outcrops of the Nama Group, Karoo Sequence and Kalahari Group can also be found in the region. The Table B.1 shows the order of the rock record. The top entry in the table is the most recent formation and the last entry is the oldest exposed formation found in the region.

Table B.1: Geological formations found in the southern Kalahari region.

GROUP / SEQUENCE	FORMATION
	Gordonia
Kalahari Group	Mokalanen Eden Budin Wessels
Karoo Sequence	Prince Albert Dwyka
Nama Group	Breckhorn
Olifantshoek Sequence	Groblershoop Matsap Lucknow

The Kalahari has a complex history with the younger sequences lying unconformably on the older sequences. All the formations, with the exception of the Wessels and Budin Formations, are exposed somewhere on the surface. The aeolian sand can thus cover a large variety of surfaces making it difficult to predict from which surface the radar signal will reflect. In addition, the distribution of calcretes horizons which occur throughout the region, can range from loose silty soils to hard gravelly limestones [69] which further complicates the subsurface geological layering and makes interpretation of the radar imagery more difficult.

Appendix C

The Proposed Campaign

This flight plan is based on information contained in the body of this thesis. The applications as well as the locations selected for imaging were chosen for scientific, economic and environmental reasons. Also, the availability of 'ground truth' such as TM or SPOT imagery, or other geophysical information such as Aero-magnetic or resistivity data played an important role in the selection of the test sites. A map of the proposed flight plan is shown in Figure C.1.

C.1 Molopo - Nossob - Kuruman River System

The images planned for this region are intended to assess the subsurface imaging capability of the airborne radar. The radar's VHF frequency is expected to penetrate the aeolian sand that covers most of the Kalahari region. The Kalahari geology is discussed in Appendix B.

To the north of the proposed image area, there are sand dunes with depths from 5m to 20m. These dunes can be used to determine the imaging depth of the radar. The possibility of *in situ* microwave penetration depth measurements is also being considered for 'ground truthing'.

The ephemeral Nossob, Auob, Molopo and Kuruman rivers cross the region in well developed valleys. Flow in these rivers is ephemeral and flood discharges only reach the end point of the Molopo system after periods of exceptional rainfall. The surfaces of these rivers are covered by sand but water is sometimes found below the sand. The imaging radar may be able to identify such ground water areas. The lower Molopo River is of particular interest because it is completely cut off from the Orange River by sand dunes. The radar image may show the drainage channels which existed before the onset of the present day aridity.

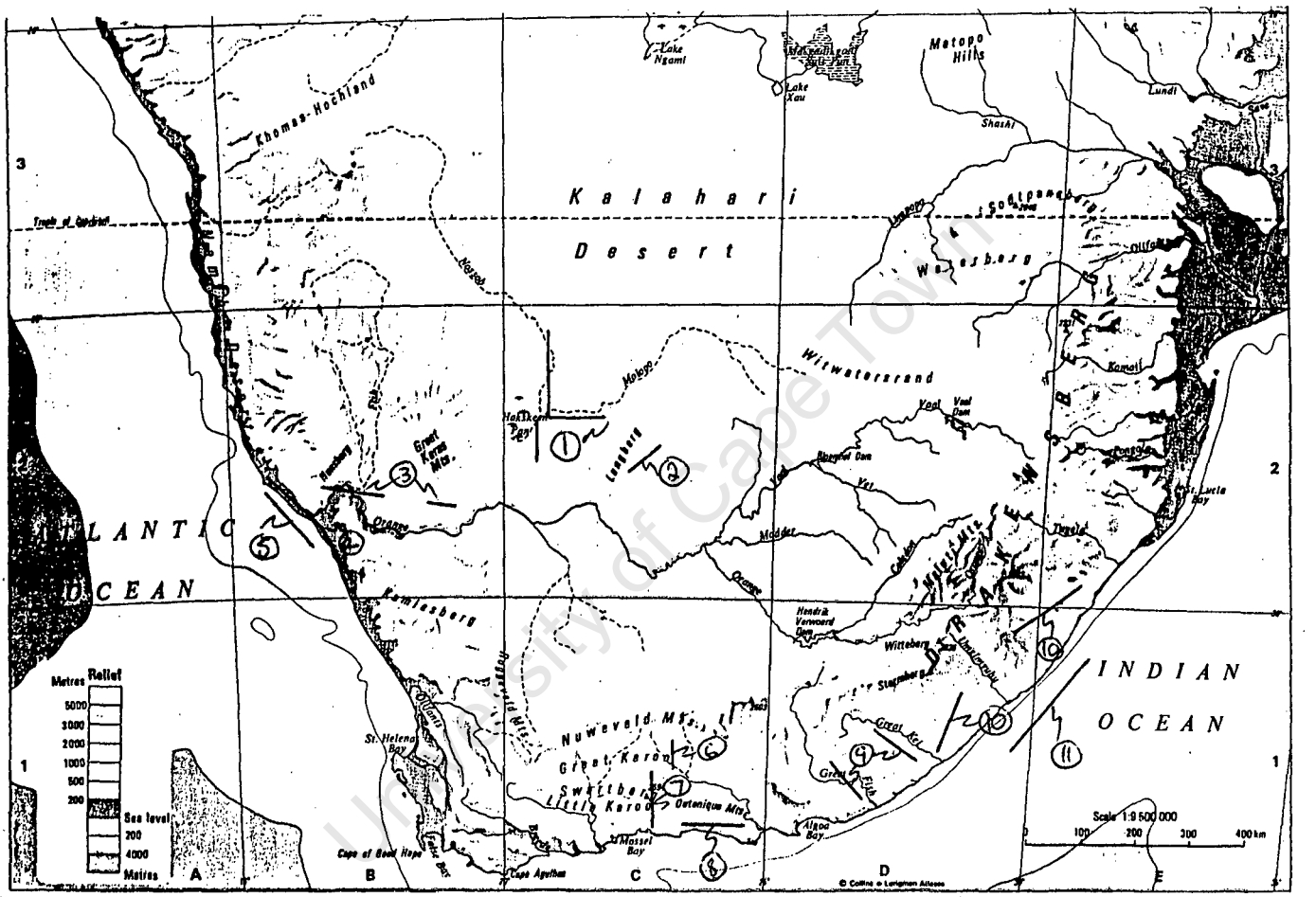

Figure C.1: A map of the proposed flight plan. The map numbers correspond to the section heading numbers.

South of the Kuruman River and east of the Molopo River are many pans. These pans occur where the Karoo System bedrock is close to the surface and the Kalahari sand cover is thin (approximately 1m). The radar image may expose paleodrainage channels which could account for the distribution of these pans. Also, identifying paleodrainages is important in hydrological studies of this very dry area.

The X-band imagery will *not* expose any subsurface geology but will highlight the surface texture variations in the area. Mapping the distribution of the dunes will be attempted but this is *not* expected to be successful. According to Blom [1, 9] the incidence angle for dune mapping must be less than the angle of repose for dry sand (approximately 34°). This angle is less than the proposed 45° incidence angle of the radar that will be flown.

Resistivity data [68] and Landsat TM imagery [70] of this area is available for a comparative study.

C.2 Ghaap Plateau

Dr. Newton [70] suggested imaging the Ghaap Plateau along the Kuruman - Sishen line. Since the purpose of this swath is to investigate the surface features, the X-band frequency will be used. For comparison, aero-magnetic maps and TM images are also available.

C.3 Fish River Canyon

Stereo radar images of the Fish River Canyon in the vicinity of Ai-Ais can be obtained by overflying the same area from different directions. Hence, the Ai-Ais area will be imaged (X-band) while flying from Upington to Luderitz and again while flying from Luderitz to Upington. Two swaths will be taken in each direction, one of moderately varying topography and the other of rapidly varying topography. This will be done to investigate the effect of relief type on the accuracy of the DEM. Also, the rapidly varying topography of the canyon is expected to cause layover and shadowing, the effects of which will be fully investigated. Both stereo pairs will be imaged using the *same-side* stereo arrangement discussed in Chapter 8.

C.4 Luderitz to Hondeklipbaai

This area is of considerable economic importance since it is rich in diamonds. Hence, swaths of the diamond bearing sands along the west coast will be taken while flying from Luderitz to Hondeklipbaai via Oranjemund and Kleinsee. The diamonds in this region are known to be in close proximity to the old drainage channels [66] since the water which once flowed in these channels transported the diamondiferous gravels to the coast. Although presently covered by sand, the VHF-band frequency is expected to penetrate the sand cover and to some extent reveal the subsurface gullies and paleochannels. Thus, the VHF imagery could have far reaching economic consequences. In addition to identifying possible diamond locations, the mapping of paleochannels could also be beneficial for hydrological studies of this very dry region. Also, the planned X-band imagery should enable mapping and differentiation of the superficial cover types. Landsat TM images [70] of the area are available.

C.5 Offshore imaging (Kleinsee to Luderitz)

Swaths of the sea surface will be taken while flying from Kleinsee to Luderitz. Using such images it might be possible to monitor schools of fish below the surface. The feasibility of this application is discussed in Chapter 7. Since sea surface imaging applications are based on the Bragg scattering phenomenon, X-band imagery would be required.

C.6 Beaufort West

Dr. Newton [70] suggested an X-band swath through the town of Beaufort West to investigate the differentiation of rock types in the Karoo sequence, including dolerite sills and dykes. The imagery might also be useful in fracture trace studies. Good geological maps of the area are available. To facilitate the geological interpretation of the imagery, stereo imaging is also being planned.

C.7 Great and Little Karoo

While flying from Beaufort West to George, the Great Karoo and Little Karoo will be imaged. Due to the semi-arid nature of the Karoo, subsurface penetration of the VHF signal is expected. Surface textural variations will be mapped

using the X-band frequency. Shape-from-shading and/or radar stereoscopy will be implemented to extract topographic information from the radar data.

C.8 Knysna - Tsitsikamma Forest

Radar penetration of the Knysna - Tsitsikamma forest canopy will be investigated while flying from George to Port Elizabeth. Since dense vegetation cover is the ideal terrain for shape-from-shading applications, a DEM will be extracted from the data.

Near Cape St. Francis, a project to determine the dynamics of the aeolian dune field is in progress. These dunes are crossed by at least one large river. Reasonably good knowledge of the sub-sand geology is available. It would thus be useful to take VHF and X-band imagery of this dune field.

C.9 Cradock - Grahamstown - Port Alfred

Stereo images of the Cradock - Grahamstown - Port Alfred swath can be produced by imaging the same area with slightly different imaging geometry. This particular area was chosen to coincide with the Shuttle Imaging Radar B (SIR-B) data so that a comparison can be made between VHF and X-band images of the airborne SAR and the L-band image of the SIR-B radar.

C.10 East London - Umtata - Durban

Using both the VHF and X-band frequencies it may be possible to map the distribution of sugar cane in the region. The sensors X-band frequency and large incidence angle is optimum for vegetation mapping. In addition, images of areas used for informal and formal settlement can be made. In Natal, many of these areas are covered by dense vegetation, and it will be interesting to compare high and low frequency images.

C.11 Offshore imaging (Durban)

Images of the sea surface will be used to investigate the feasibility of detecting oil spills using an imaging radar. This will involve a controlled oil spill off the coast, followed by clearing up operations. An extra flight might be planned to

monitor the clearing up operation. The sensor parameters (incidence angle of 45° and X-band frequency) are optimum for oil detection on the sea surface.

Appendix D

MathCad Simulations

MathCad is a software package for numerical manipulation of mathematical formulas and expressions. This software was used to implement and analyze formulas.

The section "The Dielectric Constant of Pure Water" and "The Dielectric Constant of Saline Water" is based on expressions by Ulaby [98].

The section "Simulation: Microwave Attenuation at 1.4 GHz" is based on a dielectric model for soil by Hallikainen [48] and an attenuation formula by Ulaby [98].

Next, the section "Subsurface Roughness as a function of Frequency" is based on expressions by Berlin [7] and others.

Lastly, the sections "Enhancement Ratio as a function of Sand Depth" and "Enhancement Ratio as a function of Incidence Angle" is entirely based on a simulation by Elachi [29].

THE DIELECTRIC CONSTANT OF PURE WATER

Frequency : $i := 4, 4.2 .. 12$

$f(i) := 10^{i}$

Temperature : $T := 25$

Dielectric constant - high limit :

$$\varepsilon_{w\infty}(T) := 4.9$$

Dielectric constant - low limit :

$$\varepsilon_{w0}(T) := 88.045 - 0.4147 \cdot T + 6.295 \cdot 10^{-4} \cdot T^2 + 1.075 \cdot 10^{-5} \cdot T^3$$

Relaxation frequency (Pure water) :

$$f_0(T) := \left(1.1109 \cdot 10^{-10} - 3.824 \cdot 10^{-12} \cdot T + 6.938 \cdot 10^{-14} \cdot T^2 - 5.096 \cdot 10^{-16} \cdot T^3\right)^{-1}$$

Real part of dielectric constant :

$$\varepsilon_{wr}(i, T) := \varepsilon_{w\infty}(T) + \left[\frac{\varepsilon_{w0}(T) - \varepsilon_{w\infty}(T)}{1 + \left(\frac{f(i)}{f_0(T)}\right)^2}\right]$$

Imaginary part of dielectric constant :

$$\varepsilon_{wi}(i, T) := \left[\frac{\left(\frac{f(i)}{f_0(T)}\right) \cdot \left(\varepsilon_{w0}(T) - \varepsilon_{w\infty}(T)\right)}{1 + \left(\frac{f(i)}{f_0(T)}\right)^2}\right]$$

GRAPH OF DIELECTRIC CONSTANT (REAL PART)

TEMPERATURE IS 25 DEGREES

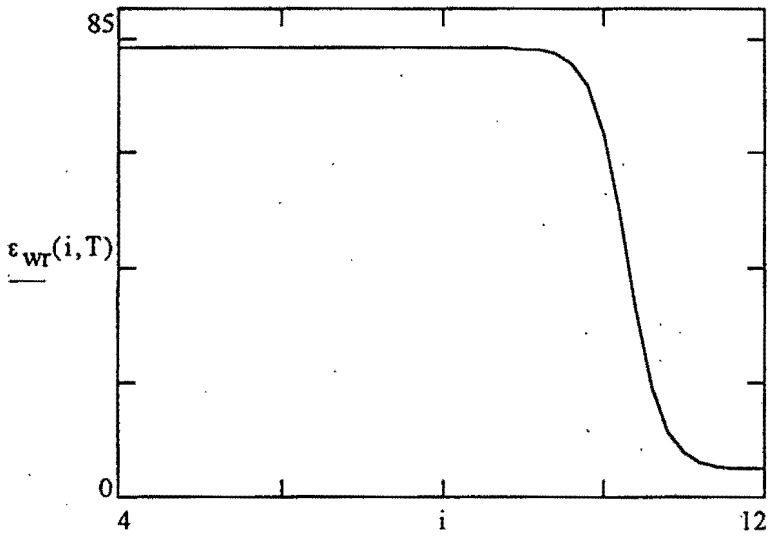

GRAPH OF DIELECTRIC CONSTANT (IMAGINARY PART)

TEMPERATURE IS 25 DEGREES

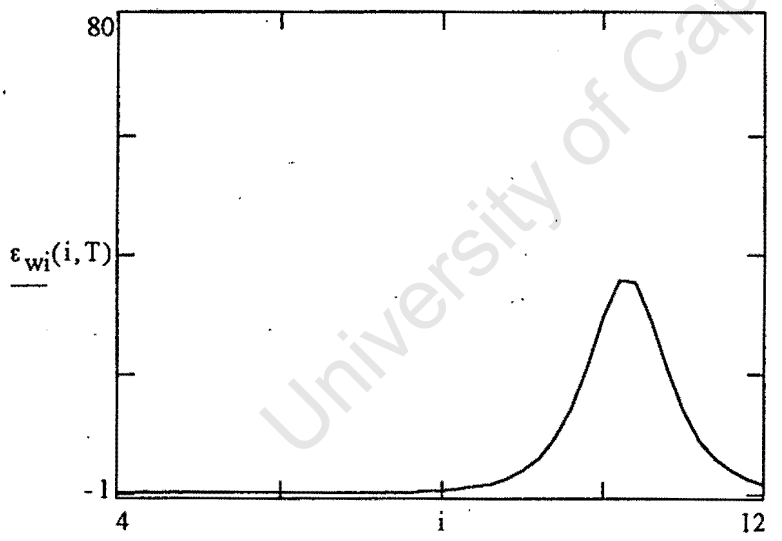

THE DIELECTRIC CONSTANT OF SALINE WATER

Frequency : $i := 4, 4.2 .. 12$

$f(i) := 10^{i}$

Free space permittivity : $\varepsilon_0 := 8.854 \cdot 10^{-12}$

Dielectric constant - high limit : $\varepsilon_{w\infty}(T,S) := 4.9$

Dielectric constant - low limit :

$$\varepsilon w_{00}(T) := 87.134 - 1.949 \cdot 10^{-1} \cdot T - 1.276 \cdot 10^{-2} \cdot T^2 + 2.491 \cdot 10^{-4} \cdot T^3$$

$$a(T,S) := 1.0 + 1.613 \cdot 10^{-5} \cdot T \cdot S - 3.656 \cdot 10^{-3} \cdot S + 3.210 \cdot 10^{-5} \cdot S^2 - 4.232 \cdot 10^{-7} \cdot S^3$$

$$\varepsilon_{w0}(T,S) := \varepsilon w_{00}(T) \cdot a(T,S)$$

Relaxation frequency (Pure water) :

$$\tau_0(T) := \left(1.1109 \cdot 10^{-10} - 3.824 \cdot 10^{-12} \cdot T + 6.938 \cdot 10^{-14} \cdot T^2 - 5.096 \cdot 10^{-16} \cdot T^3\right)$$

$$b(T,S) := 1.0 + 2.282 \cdot 10^{-5} \cdot T \cdot S - 7.638 \cdot 10^{-4} \cdot S - 7.760 \cdot 10^{-6} \cdot S^2 + 1.105 \cdot 10^{-8} \cdot S^3$$

$$\tau(T,S) := \tau_0(T) \cdot b(T,S)$$

$$f_0(T,S) := \tau(T,S)^{-1}$$

Ionic conductivity :

$$\sigma_{25}(S) := S \cdot \left(0.18252 - 1.4619 \cdot 10^{-3} \cdot S + 2.093 \cdot 10^{-5} \cdot S^2 - 1.282 \cdot 10^{-7} \cdot S^3\right)$$

$$\delta(T) := 25 - T$$

$$X(T,S) := 2.033 \cdot 10^{-2} + 1.266 \cdot 10^{-4} \cdot \delta(T) + 2.464 \cdot 10^{-6} \cdot \delta(T)^2$$

$$Y(T,S) := 1.849 \cdot 10^{-5} - 2.551 \cdot 10^{-7} \cdot \delta(T) + 2.551 \cdot 10^{-8} \cdot \delta(T)^2$$

$$\phi(T,S) := \delta(T) \cdot (X(T,S) - S \cdot (Y(T,S)))$$

$$\sigma(T,S) := \sigma_{25}(S)\cdot\exp(-\phi(T,S))$$

Real part of dielectric constant :

$$\varepsilon_{wr}(i,T,S) := \varepsilon_{w\infty}(T,S) + \left[\frac{\varepsilon_{w0}(T,S) - \varepsilon_{w\infty}(T,S)}{1 + \left(\frac{f(i)}{f_0(T,S)}\right)^2}\right]$$

Imaginary part of dielectric constant :

$$\varepsilon_{wi}(i,T,S) := \left[\frac{\left(\frac{f(i)}{f_0(T,S)}\right)\cdot\left(\varepsilon_{w0}(T,S) - \varepsilon_{w\infty}(T,S)\right)}{1 + \left(\frac{f(i)}{f_0(T,S)}\right)^2}\right] + \left(\frac{\sigma(T,S)}{2\cdot\pi\cdot\varepsilon_0\cdot f(i)}\right)$$

GRAPH OF DIELECTRIC CONSTANT (REAL PART)

SALT CONTENT IS 1 IN 1000

TEMPERATURE IS 25 DEGREES

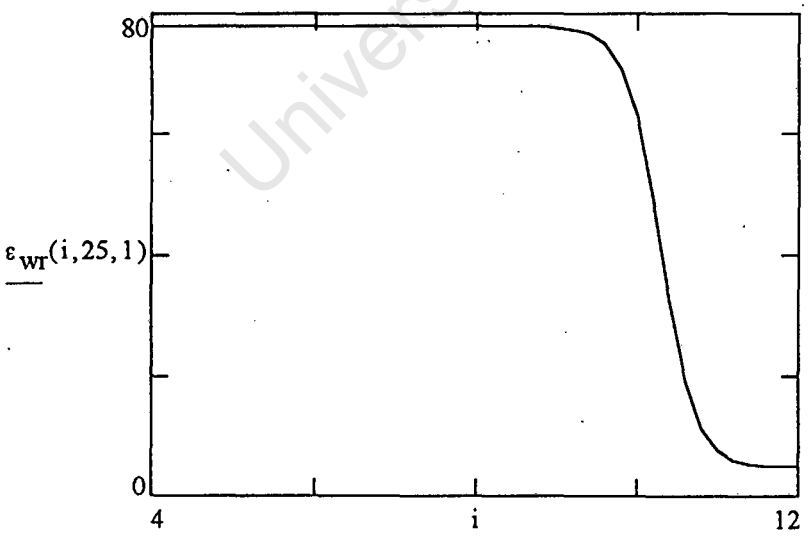

GRAPH OF DIELECTRIC CONSTANT (IMAGINARY PART)

SALT CONTENT IS 1 IN 1000

TEMPERATURE IS 25 DEGREES

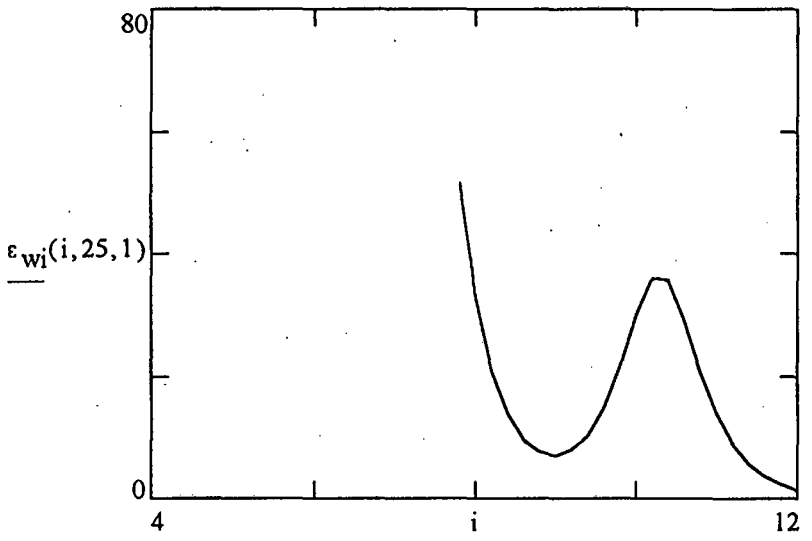

SIMULATION

MICROWAVE ATTENUATION AT 1.4 GHz

Constants:

Real:

$ar_0 := 2.862$ $br_0 := 3.803$ $cr_0 := 119.006$

$ar_1 := -0.012$ $br_1 := 0.462$ $cr_1 := -0.500$

$ar_2 := 0.001$ $br_2 := -0.341$ $cr_2 := 0.633$

Imaginary:

$ai_0 := 0.356$ $bi_0 := 5.507$ $ci_0 := 17.753$

$ai_1 := -0.003$ $bi_1 := 0.044$ $ci_1 := -0.313$

$ai_2 := -0.008$ $bi_2 := -0.002$ $ci_2 := 0.206$

Soil moisture:

$m_v := 0, 0.001 .. 0.6$

Soil textural components

$S := 60$ $C := 20$

Polynomial equations

$ar := ar_0 + ar_1 \cdot S + ar_2 \cdot C$ $ai := ai_0 + ai_1 \cdot S + ai_2 \cdot C$

$br := br_0 + br_1 \cdot S + br_2 \cdot C$ $bi := bi_0 + bi_1 \cdot S + bi_2 \cdot C$

$cr := cr_0 + cr_1 \cdot S + cr_2 \cdot C$ $ci := ci_0 + ci_1 \cdot S + ci_2 \cdot C$

$\varepsilon r(m_v) := ar + br \cdot m_v + cr \cdot m_v^2$ $\varepsilon i(m_v) := ai + bi \cdot m_v + ci \cdot m_v^2$

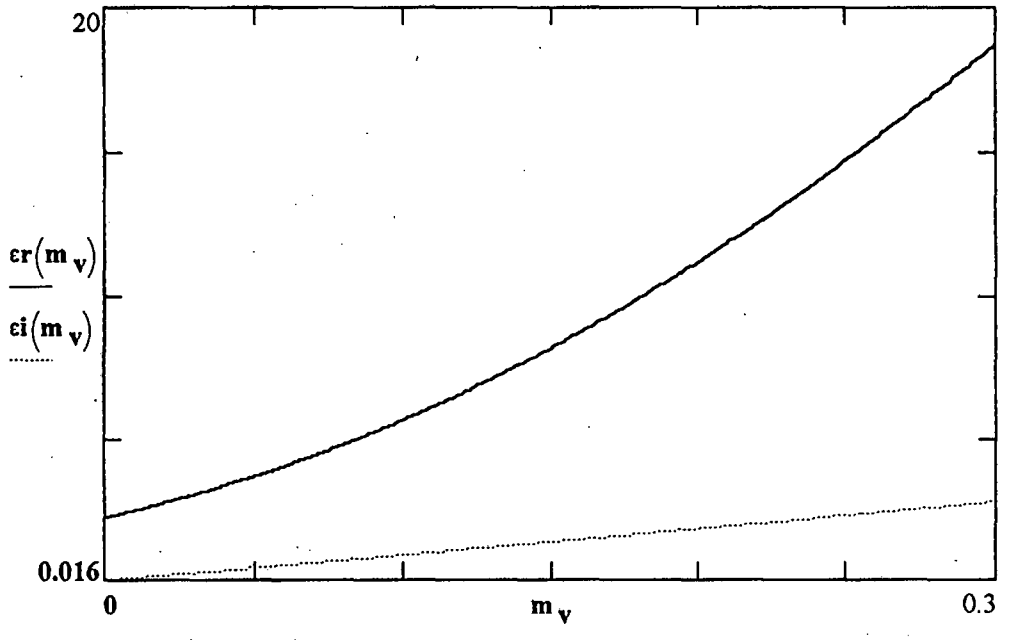

Frequency /Wavelength

Frequency : $f := 1.4 \cdot 10^9$ Hz

Light speed : $c := 3 \cdot 10^8$ m/s

Wavelength : $\lambda := \frac{c}{f}$ $\lambda = 0.214$ m

Loss tangent : $\tan\delta(m_v) := \frac{\varepsilon i(m_v)}{\varepsilon r(m_v)}$

Attenuation :

$$\alpha(m_v) := \left(\frac{2 \cdot \pi}{\lambda}\right) \cdot \left[\left(\frac{\varepsilon r(m_v)}{2}\right) \cdot \left[\left[1 + \left(\frac{\varepsilon i(m_v)}{\varepsilon r(m_v)}\right)^2\right]^{0.5} - 1\right]\right]^{0.5}$$

Attenuation: dB's / meter :

$$A(m_v) := \alpha(m_v) \cdot 20$$

Skin depth :

$$\delta(m_v) := \frac{1}{\alpha(m_v)}$$

Microwave Attenuation in soil

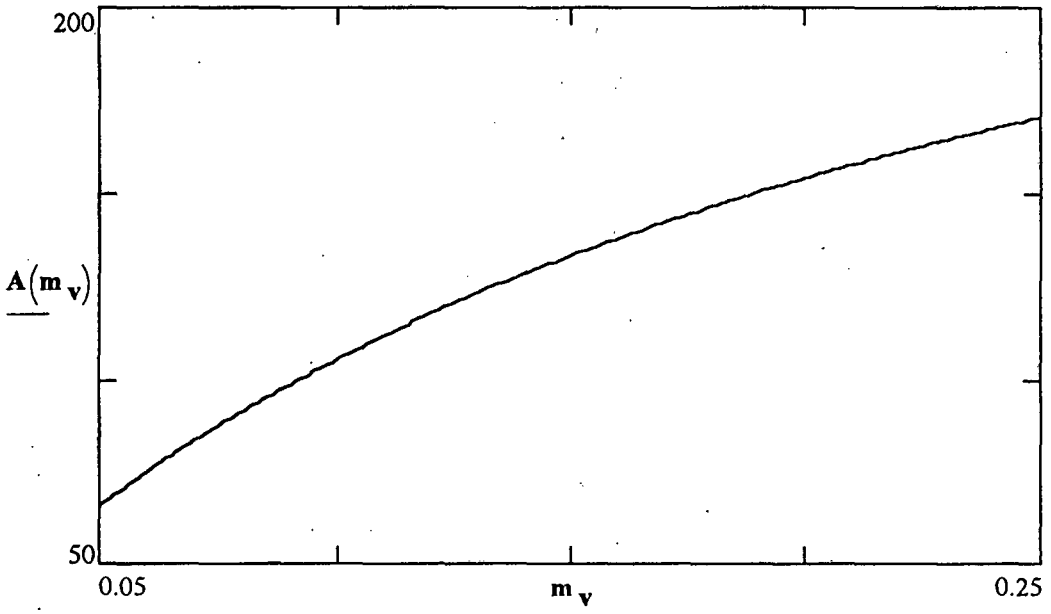

Skin depth (1.4 GHz)

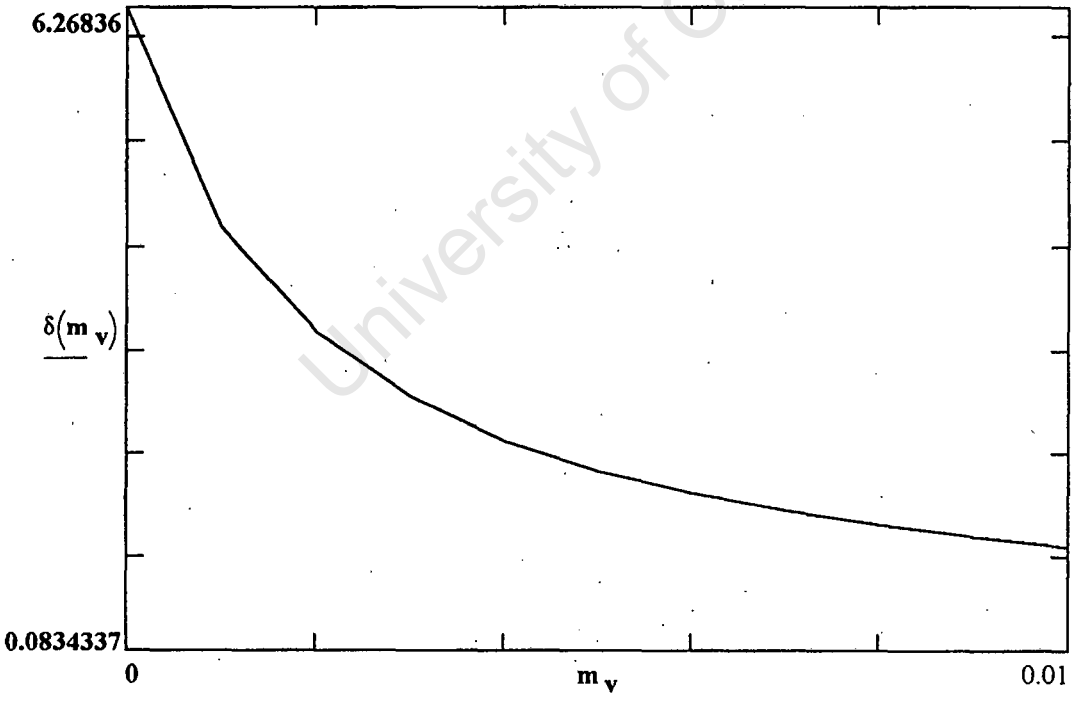

SUBSURFACE ROUGHNESS AS A FUNCTION OF FREQUENCY

Basic Units :

$m \equiv 1L$ $s \equiv 1T$

$Hz \equiv s^{-1}$ $MHz \equiv 10^{6} \cdot Hz$

$c \equiv 3 \cdot 10^{8} \cdot m \cdot s^{-1}$

$rad \equiv 1$

$deg \equiv \frac{\pi}{180} \cdot rad$

Frequency : $f := 50 \cdot MHz, 60 \cdot MHz .. 1000 \cdot MHz$

Wavelength : $\lambda(f) := \frac{c}{f}$

Incidence angle : $\theta := 10 \cdot deg$

Complex dielectric constant : $\varepsilon := 2.5$

In the substrate, the wavelength shortens.

Substrate wavelength : $s\lambda(f) := \frac{\lambda(f)}{\sqrt{\varepsilon}}$

Substrate incidence angle : $s\theta := \operatorname{asin}\left(\frac{\sin(\theta)}{\sqrt{\varepsilon}}\right)$

Microrelief height of subsurface :

Rayleigh criterion : $sh\_r(f) := \frac{s\lambda(f)}{8 \cdot \cos(s\theta)}$

Fraunhofer criterion : $sh\_f(f) := \frac{s\lambda(f)}{32 \cdot \cos(s\theta)}$

Subsurface microheight (Rayleigh criterion)

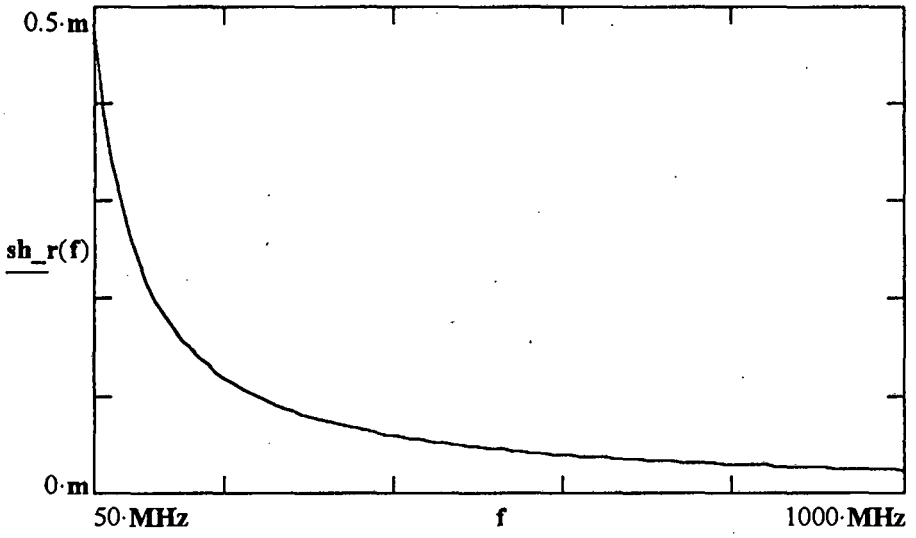

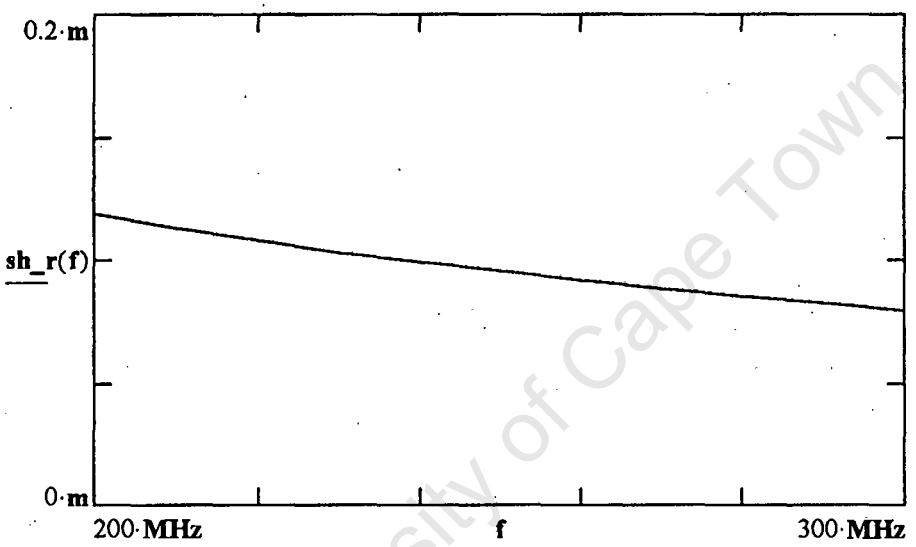

Subsurface microheight (Fraunhofer criterion)

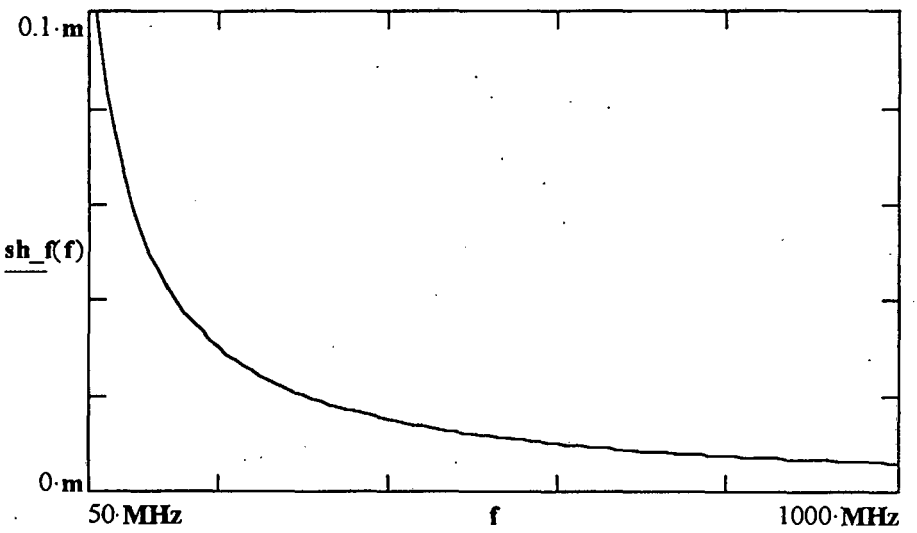

ENHANCEMENT RATIO AS A FUNCTION OF SAND DEPTH

Magnetic permeability of free space

absolute : $\mu 0 := 4 \cdot \pi \cdot 10^{-7} \cdot henry \cdot m^{-1}$

relative : $\mu r := 1$

Dielectric permittivity :

Free Space : (absolute) $\varepsilon 0 := 8.85 \cdot 10^{-12} \cdot farad \cdot m^{-1}$

Air medium : (relative) $\varepsilon r_0 := 1$

Bedrock medium : (relative) $\varepsilon r_1 := 8$

Sand medium : (relative) $\varepsilon r_2 := 2.5$

Speed of light : $c := 3 \cdot 10^{8} \cdot m \cdot sec^{-1}$

Transmit frequency : $f_0 := 1.3 \cdot GHz$

Depth of Sand layer : $L := 0 \cdot m, 0.5 \cdot m .. 5 \cdot m$

Skin depth of sand medium : $d := 5 \cdot m$

Incidence angles

Air medium : $\theta_0 := 50 \cdot deg$

Sand medium : $\theta_2 := asin\left(\frac{\sin(\theta_0)}{\sqrt{\varepsilon r_2}}\right)$

Wavelengths

Air medium : $\lambda_0 := \frac{c}{f_0}$

Sand medium : $\lambda_2 := \frac{\lambda_0}{\sqrt{\varepsilon r_2}}$

Scattering Functions

Scattering Function for Horizontal Polarization :

$$f_H(\varepsilon,\lambda,\theta) := \left(\frac{2\cdot\pi}{\lambda}\right)^4 \cdot \cos(\theta)^4 \cdot \left[\frac{\varepsilon - 1}{\left(\cos(\theta) + \sqrt{\varepsilon - \sin(\theta)^2}\right)^2}\right]^2$$

Scattering Function for Vertical Polarization :

$$f_V(\varepsilon,\lambda,\theta) := \left(\frac{2\cdot\pi}{\lambda}\right)^4 \cdot \cos(\theta)^4 \cdot \left[\frac{(\varepsilon - 1)\cdot\left[\varepsilon + (\varepsilon - 1)\cdot\sin(\theta)^2\right]}{\left(\varepsilon\cdot\cos(\theta) + \sqrt{\varepsilon - \sin(\theta)^2}\right)^2}\right]^2$$

Scattering Function for Cross Polarization :

$$g(\varepsilon,\lambda,\theta) := \left(\frac{2\cdot\pi}{\lambda}\right)^8 \cdot \left[\frac{\cos(\theta)^4\cdot(\varepsilon - 1)^4\cdot\left(\varepsilon - \sin(\theta)^2\right)}{\left(\cos(\theta) + \sqrt{\varepsilon - \sin(\theta)^2}\right)^2\cdot\left(\varepsilon\cdot\cos(\theta) + \sqrt{\varepsilon - \sin(\theta)^2}\right)^2}\right]$$

Intrinsic Impedances

Air medium : $\eta_0 := \sqrt{\frac{\mu r\cdot\mu 0}{\varepsilon r_0\cdot\varepsilon 0}}$ $\eta_0 = 376.819\cdot ohm$

Sand medium : $\eta_2 := \sqrt{\frac{\mu r\cdot\mu 0}{\varepsilon r_2\cdot\varepsilon 0}}$ $\eta_2 = 238.322\cdot ohm$

Transmissivities

Transmissivity for Horizontal Polarization :

$$T_H := \left(\left| \frac{2 \cdot \eta_2 \cdot \cos(\theta_0)}{\eta_2 \cdot \cos(\theta_0) + \eta_0 \cdot \cos(\theta_2)} \right| \right)^2 \cdot \left[\frac{\mathrm{Re}\left(\frac{\cos(\theta_2)}{\eta_2} \right)}{\mathrm{Re}\left(\frac{\cos(\theta_0)}{\eta_0} \right)} \right]$$

$$T_H = 0.866$$

Transmissivity for Vertical Polarization :

$$T_V := \left(\left| \frac{2 \cdot \eta_0 \cdot \cos(\theta_0)}{\eta_0 \cdot \cos(\theta_0) + \eta_2 \cdot \cos(\theta_2)} \right| \right)^2 \cdot \left(\frac{\mathrm{Re}(\eta_2 \cdot \cos(\theta_2))}{\mathrm{Re}(\eta_0 \cdot \cos(\theta_0))} \right)$$

$$T_V = 0.994$$

Enhancement Ratio

Enhancement Ratio for Horizontal Polarization

$$R_H(L) := T_H^2 \cdot \exp\left(\frac{-2 \cdot L}{d \cdot \cos(\theta_2)} \right) \cdot \left[\frac{f_H\left[\left(\frac{\varepsilon r_1}{\varepsilon r_2} \right), \lambda_2, \theta_2 \right]}{f_H(\varepsilon r_1, \lambda_0, \theta_0)} \right]$$

Enhancement Ratio for Vertical Polarization

$$R_V(L) := T_V^2 \cdot \exp\left(\frac{-2 \cdot L}{d \cdot \cos(\theta_2)} \right) \cdot \left[\frac{f_V\left[\left(\frac{\varepsilon r_1}{\varepsilon r_2} \right), \lambda_2, \theta_2 \right]}{f_V(\varepsilon r_1, \lambda_0, \theta_0)} \right]$$

Enhancement Ratio for Cross Polarization

$$R_{HV}(L) := T_H \cdot T_V \cdot \exp\left(\frac{-2 \cdot L}{d \cdot \cos(\theta_2)} \right) \cdot \left[\frac{g\left[\left(\frac{\varepsilon r_1}{\varepsilon r_2} \right), \lambda_2, \theta_2 \right]}{g(\varepsilon r_1, \lambda_0, \theta_0)} \right]$$

Graph of Enhancement Ratios

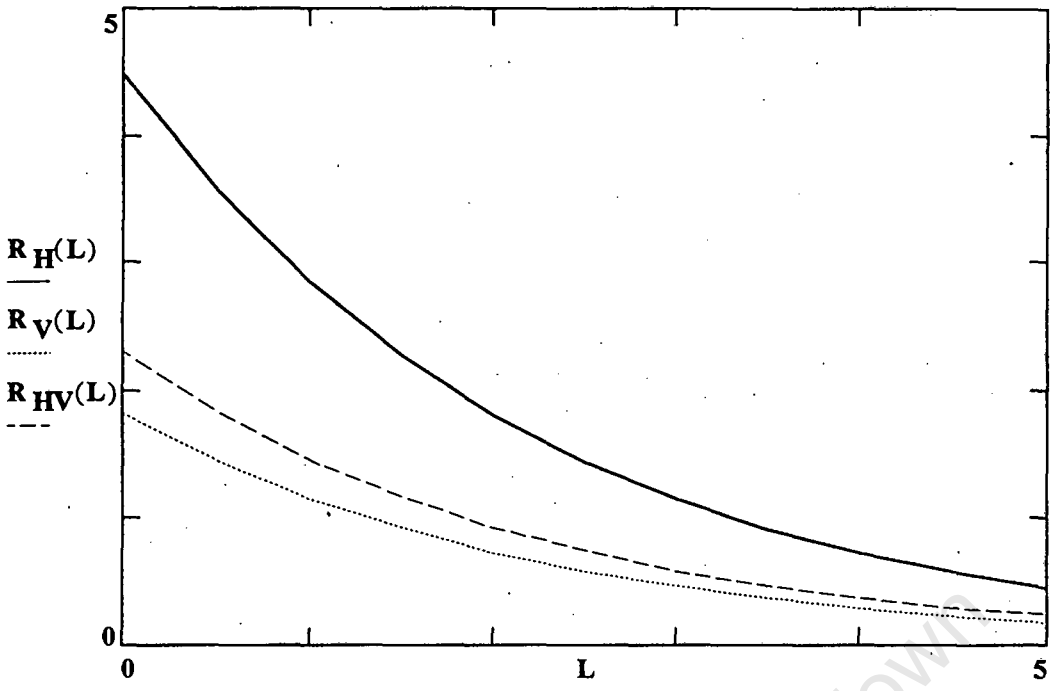

ENHANCEMENT RATIO AS A FUNCTION OF INCIDENCE ANGLE

Magnetic permeability of free space

Absolute : $\mu 0 := 4 \cdot \pi \cdot 10^{-7} \cdot henry \cdot m^{-1}$

Relative : $\mu r := 1$

Dielectric permittivity

Free Space : (absolute) $\varepsilon 0 := 8.85 \cdot 10^{-12} \cdot farad \cdot m^{-1}$

Air : (relative) $\varepsilon r_0 := 1$

Bedrock : (relative) $\varepsilon r_1 := 8$

Sand : (relative) $\varepsilon r_2 := 2.5$

Speed of light : $c := 3 \cdot 10^{8} \cdot m \cdot sec^{-1}$

Transmit frequency : $f_0 := 1.3 \cdot GHz$

Depth of Sand layer : $L := 4 \cdot m$

Skin depth of Sand medium : $d := 5 \cdot m$

Incidence angles

Air medium : $\theta_0 := 30 \cdot deg, 31 \cdot deg .. 70 \cdot deg$

Sand medium : $\theta_2(\theta_0) := asin\left(\frac{\sin(\theta_0)}{\sqrt{\varepsilon r_2}}\right)$

Wavelengths

Air medium :

$$\lambda_0 := \frac{c}{f_0}$$

Sand medium :

$$\lambda_2 := \frac{\lambda_0}{\sqrt{\varepsilon r_2}}$$

Scattering Functions

Scattering Function for Horizontal Polarization :

$$f_H(\varepsilon,\lambda,\theta) := \left(\frac{2\cdot\pi}{\lambda}\right)^4 \cdot \cos(\theta)^4 \cdot \left[\frac{\varepsilon - 1}{\left(\cos(\theta) + \sqrt{\varepsilon - \sin(\theta)^2}\right)^2}\right]^2$$

Scattering Function for Vertical Polarization :

$$f_V(\varepsilon,\lambda,\theta) := \left(\frac{2\cdot\pi}{\lambda}\right)^4 \cdot \cos(\theta)^4 \cdot \left[\frac{(\varepsilon - 1)\cdot\left[\varepsilon + (\varepsilon - 1)\cdot\sin(\theta)^2\right]}{\left(\varepsilon\cdot\cos(\theta) + \sqrt{\varepsilon - \sin(\theta)^2}\right)^2}\right]^2$$

Scattering Function for Cross Polarization :

$$g(\varepsilon,\lambda,\theta) := \left(\frac{2\cdot\pi}{\lambda}\right)^8 \cdot \left[\frac{\cos(\theta)^4\cdot(\varepsilon - 1)^4\cdot(\varepsilon - \sin(\theta)^2)}{\left(\cos(\theta) + \sqrt{\varepsilon - \sin(\theta)^2}\right)^2\cdot\left(\varepsilon\cdot\cos(\theta) + \sqrt{\varepsilon - \sin(\theta)^2}\right)^2}\right]$$

Intrinsic Impedances

Air medium :

$$n_0 := \sqrt{\frac{\mu r\cdot\mu 0}{\varepsilon r_0\cdot\varepsilon 0}} \qquad n_0 = 376.819\cdot\text{ohm}$$

Sand medium :

$$n_2 := \sqrt{\frac{\mu r\cdot\mu 0}{\varepsilon r_2\cdot\varepsilon 0}} \qquad n_2 = 238.322\cdot\text{ohm}$$

Transmissivities

Transmissivity for Horizontal Polarization :

$$T_H(\theta_0) := \left(\left| \frac{2 \cdot n_2 \cdot \cos(\theta_0)}{n_2 \cdot \cos(\theta_0) + n_0 \cdot \cos(\theta_2(\theta_0))} \right| \right)^2 \cdot \left[\frac{\mathrm{Re}\left(\frac{\cos(\theta_2(\theta_0))}{n_2} \right)}{\mathrm{Re}\left(\frac{\cos(\theta_0)}{n_0} \right)} \right]$$

Transmissivity for Vertical Polarization :

$$T_V(\theta_0) := \left(\left| \frac{2 \cdot n_0 \cdot \cos(\theta_0)}{n_0 \cdot \cos(\theta_0) + n_2 \cdot \cos(\theta_2(\theta_0))} \right| \right)^2 \cdot \left(\frac{\mathrm{Re}(n_2 \cdot \cos(\theta_2(\theta_0)))}{\mathrm{Re}(n_0 \cdot \cos(\theta_0))} \right)$$

Enhancement Ratio

Enhancement Ratio for Horizontal Polarization :

$$R_H(\theta_0) := T_H(\theta_0)^2 \cdot \exp\left(\frac{-2 \cdot L}{d \cdot \cos(\theta_2(\theta_0))} \right) \cdot \left[\frac{f_H\left[\left(\frac{\varepsilon r_1}{\varepsilon r_2} \right), \lambda_2, \theta_2(\theta_0) \right]}{f_H(\varepsilon r_1, \lambda_0, \theta_0)} \right]$$

Enhancement Ratio for Vertical Polarization :

$$R_V(\theta_0) := T_V(\theta_0)^2 \cdot \exp\left(\frac{-2 \cdot L}{d \cdot \cos(\theta_2(\theta_0))} \right) \cdot \left[\frac{f_V\left[\left(\frac{\varepsilon r_1}{\varepsilon r_2} \right), \lambda_2, \theta_2(\theta_0) \right]}{f_V(\varepsilon r_1, \lambda_0, \theta_0)} \right]$$

Enhancement Ratio for Cross Polarization :

$$R_{HV}(\theta_0) := T_H(\theta_0) \cdot T_V(\theta_0) \cdot \exp\left(\frac{-2 \cdot L}{d \cdot \cos(\theta_2(\theta_0))} \right) \cdot \left[\frac{g\left[\left(\frac{\varepsilon r_1}{\varepsilon r_2} \right), \lambda_2, \theta_2(\theta_0) \right]}{g(\varepsilon r_1, \lambda_0, \theta_0)} \right]$$

Graph of Enhancement Ratios

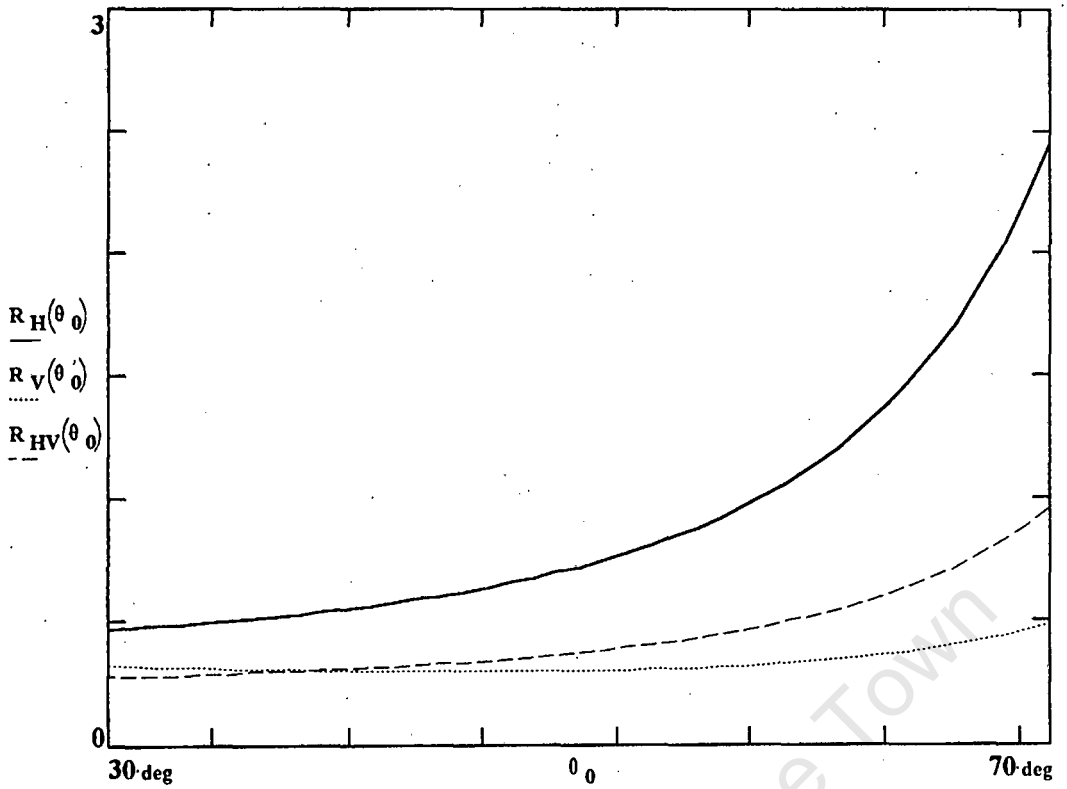

APPENDIX UNIT DEFINITIONS

MKS (SI) SYSTEM

I. Base units

$m \equiv 1L$ $kg \equiv 1M$ $sec \equiv 1T$ $coul \equiv 1Q$

II. Angular measure

$rad \equiv 1$ $deg \equiv \frac{\pi}{180} \cdot rad$

III. Derived units: Length

$cm \equiv .01 \cdot m$ $km \equiv 1000 \cdot m$ $mm \equiv .001 \cdot m$

$ft \equiv .3048 \cdot m$ $in \equiv 2.54 \cdot cm$ $yd \equiv 3 \cdot ft$ $mi \equiv 5280 \cdot ft$

IV. Derived units: Mass

$gm \equiv 10^{-3} \cdot kg$

$tonne \equiv 1000 \cdot kg$ (metric ton)

$lb \equiv 453.59247 \cdot gm$ (use convention that lb represents pounds mass.

$oz \equiv \frac{lb}{16}$

$ton \equiv 2000 \cdot lb$ ("short" ton)

$slug \equiv 32.174 \cdot lb$

V. Derived units: Time

$min \equiv 60 \cdot sec$ $hr \equiv 3600 \cdot sec$ $day \equiv 24 \cdot hr$

$yr \equiv 365.2422 \cdot day$ (tropical year)

VI. Derived units: Area, Volume

$hectare \equiv 10^4 \cdot m^2$ $acre \equiv 4840 \cdot yd^2$

$liter \equiv (.1 \cdot m)^3$ $mL \equiv 10^{-3} \cdot liter$

(Sometimes defined with "L" symbol.)

$fl\_oz \equiv 29.57353 \cdot cm^3$

$gal \equiv 128 \cdot fl\_oz$

VII. Derived units: Velocity, Acceleration

$mph \equiv \frac{mi}{hr}$ $kph \equiv \frac{km}{hr}$

$g \equiv 9.80665 \cdot \frac{m}{sec^2}$ (acceleration of gravity)

VIII. Derived units: Force, Energy, Power

$$\text{newton} \equiv \text{kg} \cdot \frac{\text{m}}{\text{sec}^2} \qquad \text{dyne} \equiv 10^{-5} \cdot \text{newton}$$

$$\text{lbf} \equiv \text{g} \cdot \text{lb}$$

(pound force)

$$\text{kgf} \equiv \text{g} \cdot \text{kg}$$

(kilogram force)

$$\text{joule} \equiv \text{newton} \cdot \text{m} \qquad \text{erg} \equiv 10^{-7} \cdot \text{joule} \qquad \text{cal} \equiv 4.1868 \cdot \text{joule}$$

$$\text{kcal} \equiv 1000 \cdot \text{cal}$$

$$\text{BTU} \equiv 1.05505585262 \cdot 10^{3} \cdot \text{joule}$$

$$\text{watt} \equiv \frac{\text{joule}}{\text{sec}} \qquad \text{kW} \equiv 1000 \cdot \text{watt} \qquad \text{hp} \equiv 550 \cdot \frac{\text{ft} \cdot \text{lbf}}{\text{sec}}$$

(standard horsepower)

IX. Derived units: Pressure, Viscosity

$$\text{Pa} \equiv \frac{\text{newton}}{\text{m}^2} \qquad \text{psi} \equiv \frac{\text{lbf}}{\text{in}^2} \qquad \text{atm} \equiv 1.01325 \cdot 10^{5} \cdot \text{Pa}$$

$$\text{torr} \equiv 1.33322 \cdot 10^{2} \cdot \text{Pa}$$

$$\text{in\_Hg} \equiv 3.38638 \cdot 10^{3} \cdot \text{Pa}$$

$$\text{stokes} \equiv 10^{-4} \cdot \frac{\text{m}^2}{\text{sec}}$$

$$\text{poise} \equiv .1 \cdot \text{Pa} \cdot \text{sec}$$

X. Derived units: Electrical

$$\text{amp} \equiv \frac{\text{coul}}{\text{sec}} \qquad \text{volt} \equiv \frac{\text{watt}}{\text{amp}} \qquad \text{ohm} \equiv \frac{\text{volt}}{\text{amp}} \qquad \text{weber} \equiv \text{volt} \cdot \text{sec}$$

$$\text{siemens} := \frac{1}{\text{ohm}} \qquad \text{farad} \equiv \frac{\text{coul}}{\text{volt}} \qquad \text{oersted} \equiv \frac{1000}{4 \cdot \pi} \cdot \frac{\text{amp}}{\text{m}}$$

$$\text{henry} \equiv \frac{\text{weber}}{\text{amp}} \qquad \text{tesla} \equiv \frac{\text{weber}}{\text{m}^2} \qquad \text{gauss} \equiv 10^{-4} \cdot \text{tesla}$$

XI. frequency

$$\text{Hz} \equiv \text{sec}^{-1}$$

$$\text{KHz} \equiv 10^{3} \cdot \text{Hz} \qquad \text{MHz} \equiv 10^{6} \cdot \text{Hz} \qquad \text{GHz} \equiv 10^{9} \cdot \text{Hz}$$

Bibliography

[1] Ronald G. Blom and Charles Elachi. Spaceborne and Airborne Imaging Radar Observations of Sand Dunes. *Journal of Geophysical Research*, 86(B4):3061–3073, April 1981.

[2] Ronald G. Blom and Michael Daily. Radar Image Processing for Rock-Type Discrimination. *IEEE Transactions on Geosc. and Remote Sensing*, 20(3):343–351, July 1982.

[3] M. Ansoult, L.W. De Backer, and M. Declercq. Statistical Relationship Between Apparent Dielectric Constant and Water Content in Porous Media. *Soil Science Society America Journal*, 49:47–50, 1985.

[4] Constantine A. Balanis. *Advanced Engineering Electromagnetics.* John Wiley and Sons, 1989.

[5] Thomas Bayer, Rudolf Winter, and Gunter Schreier. Terrain Influences in SAR Backscatter and Attempts to their Correction. *IEEE Transactions on Geosc. and Remote Sensing*, 29(3):451–462, May 1991.

[6] A. Beaudoin, Thuy Le Toan, and Q. H. J. Gwyn. SAR Observations and Modeling of the C-Band Backscatter Variability Due to Multiscale Geometry and Soil Moisture. *IEEE Transactions on Geosc. and Remote Sensing*, 28(5):886–895, September 1990.

[7] Fraydon L. Berlin, A. Tarabzouni, Abdullah H. Al-Naser, Kamel M. Sheikho, and Richard W. Larson. SIR-B Subsurface Imaging of a sand-buried landscape: Al Labbah Plateau, Saudi Arabia. *IEEE Transactions on Geosc. and Remote Sensing*, 24(4):595–602, July 1986.

[8] J. Robert Birchak, C. Gerald Gardner, and Jackie E. Hipp. High dielectric constant microwave probes for sensing soil moisture. *IEEE Proceedings*, 62(1):93–98, January 1974.

[9] Ronald G. Blom and Charles Elachi. Multifrequency and Multipolarization Radar Scatterometry of Sand Dunes and Comparison with Spaceborne and

Airborne Radar Images. *Journal of Geophysical Research*, 92(B8):7877–7889, July 1987.

[10] Ronald G. Blom, Charles Elachi, and Robert E. Crippen. Detection of subsurface features in SEASAT radar images of Means Valley, Mojave Desert, California. *Geology*, 12:346–349, June 1984.

[11] Ronald G. Blom, Leslie R. Schenck, and Ronald E. Alley. What are the Best Radar Wavelengths, Incidence Angles, and Polarizations for Discrimination Among Lava Flows and Sedimentary Rocks ? A Statistical Approach. *IEEE Transactions on Geosc. and Remote Sensing*, 25(2):208–213, March 1987.

[12] Alfred M. Bruckstein. On Shape from Shading. *Computer Vision, Graphics, and Image Processing*, 44:139–154, 1988.

[13] Jeffrey E. Campbell. Dielectric Properties and Influence of Conductivity in Soils at One to Fifty Megahertz. *Soil Science Society America Journal*, 54:332–341, March 1990.

[14] Weng Cho Chew. *Waves and Fields in Inhomogeneous Media.* Van Nostrand Reinhold, 1990.

[15] Jo Bea Cimino, Benjamin Holt, and Annie Holmes Richardson. The Shuttle Imaging Radar B (SIR-B) Experiment Report. Technical report, Jet Propulsion Laboratory, California Institute of Technology, Pasadena, California, March 1988.

[16] John C. Curlander and Robert N McDonough. *Synthetic Aperture Radar Systems and Signal Processing.* John Wiley and Sons, New York, Chichester, Brisbane,Toronto,Singapore, 1991.

[17] Richard A. Davis. *Depositional systems : A Genetic Approach to Sedimentary Geology.* Prentice Hall Inc., 1983.

[18] Myron C. Dobson, Leland Pierce, Kamal Sarabandi, and Fawwaz T. Ulaby. Preliminary Analysis of ERS-1 SAR for Forest Ecosystem Studies. *IEEE Transactions on Geosc. and Remote Sensing*, 30(2):203–211, March 1992.

[19] Myron C. Dobson and Fawwaz T. Ulaby. Active Microwave Soil Moisture Research. *IEEE Transactions on Geosc. and Remote Sensing*, 24(1):23–35, January 1986.

[20] Myron C. Dobson and Fawwaz T. Ulaby. Preliminary Evaluation of the SIR-B Response to Soil Moisture, Surface Roughness, and Crop Canopy Cover. *IEEE Transactions on Geosc. and Remote Sensing*, 24(4):517–526, July 1986.

[21] Myron C. Dobson, Fawwaz T. Ulaby, David R. Brunfeldt, and Daniel N. Held. External Calibration of SIR-B Imagery with Area-Extended and Point Targets. *IEEE Transactions on Geosc. and Remote Sensing*, 24(4):453–460, July 1986.

[22] Myron C. Dobson, Fawwaz T. Ulaby, Martti Hallikainen, Mohamed A. El-Rayes, and Lin-Kun Wu. Microwave Dielectric Behavior of Wet Soil - Part 2 : Dielectric Mixing Models. *IEEE Transactions on Geosc. and Remote Sensing*, 23(1):35–46, January 1985.

[23] Gitta Domik, Franz Leberl, and Jo Bea Cimino. Multiple Incidence Angle SIR-B Experiment Over Argentina: Generation of Secondary Image Products. *IEEE Transactions on Geosc. and Remote Sensing*, 24(4):492–497, July 1986.

[24] Stephen A. Drury. *Image Interpretation in Geology.* Allen and Unwin Ltd., 40 Museum Street, London, UK, 1987.

[25] Editorial. SAR technology for monitoring oil spills. OE Reports: The International Society for Optical Engineering, December 1993.

[26] Charles Elachi. Spaceborne Imaging Radar. *Scientific American*, December 1982.

[27] Charles Elachi. *Introduction to the Physics and Techniques of Remote Sensing.* Wiley Series in Remote Sensing. Wiley and Sons, 1987.

[28] Charles Elachi. *Spaceborne Radar Remote Sensing: Applications and Techniques.* The Institute of Electrical and Electronics Engineers Press, 1988.

[29] Charles Elachi, Gerald G. Schaber, and Ladislav E. Roth. Spaceborne Radar Subsurface Imaging in Hyperarid Regions. *IEEE Transactions on Geosc. and Remote Sensing*, 22(4):383–387, July 1984.

[30] Edwin T. Engman and James R. Wang. Evaluating Roughness Models of Radar Backscatter. *IEEE Transactions on Geosc. and Remote Sensing*, 25(6):709–713, November 1987.

[31] Diane L. Evans. Multisensor Classification of Sedimentary Rocks. *Remote Sensing of Environment*, 25:129–144, 1988.

[32] Diane L. Evans. Current status and future developments in radar remote sensing. *ISPRS Journal of Photogrammetry and Remote Sensing*, 47:79–99, 1992.

[33] Diane L. Evans, Tom G. Farr, J. P. Ford, Thomas W. Thompson, and C. L. Werner. Multipolarization Radar Images for Geologic Mapping and Vegetation Discrimination. *IEEE Transactions on Geosc. and Remote Sensing*, 24(2):246–257, March 1986.

[34] Diane L. Evans, Tom G. Farr, and Jakob J. van Zyl. Estimates of Surface Roughness Derived from Synthetic Aperture Radar (SAR) Data. *IEEE Transactions on Geosc. and Remote Sensing*, 30(2):382–389, March 1992.

[35] Diane L. Evans, Tom G. Farr, Jakob J. van Zyl, and Howard A. Zebker. Radar Polarimetry: Analysis Tools and Applications. *IEEE Transactions on Geosc. and Remote Sensing*, 26(6):774–789, November 1988.

[36] Tom G. Farr, Charles Elachi, Philip Hartl, and K. Chowdhury. Microwave penetration and attenuation in desert soil: A field experiment with the Shuttle Imaging Radar. *IEEE Transactions on Geosc. and Remote Sensing*, 24(4):590–594, July 1986.

[37] Robert T. Frankot and Rama Chellappa. Application of a Shape From Shading Technique to Synthetic Aperture Radar Imagery. In *1987 International Geoscience and Remote Sensing Symposium (IGARSS'87)*, pages 1323–1329. IEEE Geoscience and Remote Sensing Society, May 1987.

[38] Anthony Freeman. SAR Calibration: An Overview. *IEEE Transactions on Geosc. and Remote Sensing*, 30(6):1107–1121, November 1992.

[39] Adrian K. Fung and K.S. Chen. Backscatter from a Randomly Rough Dielectric Surface. *IEEE Transactions on Geosc. and Remote Sensing*, 30(2):356–369, March 1992.

[40] James Gilluly. *Principles Geology.* W.H. Freeman and Company, 1958.

[41] A. Laurence Gray and Peter J. Farris-Manning. Repeat-Pass Interferometry with Airborne Synthetic Aperture Radar. *IEEE Transactions on Geosc. and Remote Sensing*, 31(1):180–191, January 1993.

[42] A. Laurence Gray, Karim E. Mattar, and Peter J. Farris-Manning. Airborne SAR Interferometry at CCRS. In *Proceedings of the URSI Microwave Signature-92 Conference Igls-Innsbruck, Austria*, pages 3C–5 – 3C–8. Microwave Signature - 92, July 1992.

[43] A. Laurence Gray, Paris W. Vachon, Charles E. Livingstone, and Tom I. Lukowski. Synthetic Aperture Radar Calibration Using Reference Reflectors. *IEEE Transactions on Geosc. and Remote Sensing*, 28(3):374–382, May 1990.

[44] A. De Grys, editor. *Stratigraphy of South Africa.* Part 1: Lithostratigraphy of the Republic of South Africa, Namibia and the Republics of Bophuthatswana, Transkei and Venda. The South African Committee for Stratigraphy, Geological Survey, Department of Mineral and Energy Affairs, 1980.

[45] Bert Guindon. Development of a Shape-From-Shading Technique for the Extraction of Topographic Models from individual Spaceborne SAR Images. *IEEE Transactions on Geosc. and Remote Sensing*, 28(4):654–661, July 1990.

[46] Anders Gustavsson, Bjorn Larsson, and Hans Hellsten. Realization of an airborne low frequency SAR. In *Proceedings of URSI Microwave Signature-92 Conference Igls-Innsbruck, Austria*, pages 1C–23 – 1C–27. Microwave Signature - 92, July 1992.

[47] Jan O. Hagberg and Lars M.H. Ulander. On the Optimization of Interferometric SAR for Topographic Mapping. *IEEE Transactions on Geosc. and Remote Sensing*, 31(1):303–306, January 1993.

[48] Martti Hallikainen, Fawwaz T. Ulaby, Myron C. Dobson, Mohamed A. El-Rayes, and Lin-Kun Wu. Microwave Dielectric Behavior of Wet Soil - Part 1 : Empirical Models and Experimental Observations. *IEEE Transactions on Geosc. and Remote Sensing*, 23(1):25–34, January 1985.

[49] Jackie E. Hipp. Soil Electromagnetic Parameters as Functions of Frequency, Soil Density, and Soil Moisture. *IEEE Proceedings*, 62(1):98–103, January 1974.

[50] P. Hoekstra and A. Delaney. Dielectric Properties of Soils at UHF and Microwave Frequencies. *Journal of Geophysical Research*, 79(11):1699–1708, April 1974.

[51] S.A. Hovanessian. *Radar System Design and Analysis.* Artech House, 1984.

[52] P.D. Jackson, D. Taylor-Smith, and P.N Stanford. Resistivity-porosity-particle shape relationships for marine sands. *Geophysics*, 43:1250–1262, 1981.

[53] T.J. Jackson and Peggy E. O'Neil. Microwave Dielectric Model for Aggregated Soils. *IEEE Transactions on Geosc. and Remote Sensing*, 24(6):920–929, October 1986.

[54] Eric S. Kasischke, Guy A. Meadows, and Philip L. Jackson. *The use of Synthetic Aperture Radar Imagery to Detect Hazards to Navigation.* Environmental Research Institute of Michigan, Ann Arbor, Michigan, 1984.

[55] Verne H. Kaupp, L. C. Bridges, Michael A. Pisaruck, Harold C. MacDonald, and William P. Waite. Simulation of Spaceborne Stereo Radar Imagery: Experimental Results. *IEEE Transactions on Geosc. and Remote Sensing*, 21(3):400–405, July 1983.

[56] Verne H. Kaupp, William P. Waite, and Harold C. MacDonald. Incidence Angle Considerations for Spacecraft Imaging Radar. *IEEE Transactions on Geosc. and Remote Sensing*, 20(3):384–400, July 1982.

[57] N. Lancaster. Grain-size characteristics of the linear dunes in the Southwestern Kalahari. *Journal of Sedimentary Petology*, 56(3):395–400, 1986.

[58] N. Lancaster. Late Quaternary Palaeoenvironments in the Southwestern Kalahari. *Palaeogeography, Palaeoclimatology, Palaeoecology*, 70:367–376, 1989.

[59] Franz W. Leberl. *Radargrammetric Image Processing.* Artech House Inc., 1990.

[60] Franz W. Leberl, Gitta Domik, Johannes Raggam, Jo Bea Cimino, and Michael Kobrick. Multiple Incidence Angle SIR-B Experiment Over Argentina: Stereo-Radargrammetric Analysis. *IEEE Transactions on Geosc. and Remote Sensing*, 24(4):482–491, July 1986.

[61] Franz W. Leberl, Gitta Domik, Johannes Raggam, and Michael Kobrick. Radar Stereomapping Techniques and Application to SIR-B Images of Mt. Shasta. *IEEE Transactions on Geosc. and Remote Sensing*, 24(4):473–481, July 1986.

[62] Fuk K. Li and Richard. M. Goldstein. Studies of Multibaseline Spaceborne Interferometric Synthetic Aperture Radars. *IEEE Transactions on Geosc. and Remote Sensing*, 28(1):88–97, January 1990.

[63] G. Paul De Loor. The Dielectric Properties of Wet Materials. *IEEE Transactions on Geosc. and Remote Sensing*, 21(3):364–369, July 1983.

[64] Geoffrey J. Lynne and Geoffrey R. Taylor. Geological Assessment of SIR-B Imagery of the Amadeus Basin, N.T., Australia. *IEEE Transactions on Geosc. and Remote Sensing*, 24(4):575–581, July 1986.

[65] Soren N. Madsen, Howard A. Zebker, and Jan Martin. Topographic Mapping Using Radar Interferometry: Processing Techniques. *IEEE Transactions on Geosc. and Remote Sensing*, 31(1):246–256, January 1993.

[66] B.D. Maree. The Deposition and Distribution of Alluvial Diamonds. CAPEX, 1986.

[67] John F. McCauley, Carol S. Breed, and Gerald G. Schaber. Paleodrainages of the Eastern Sahara - The Radar Rivers revisited SIR-A/B Implication for a mid-tertiary Trans-African drainage system. *IEEE Transactions on Geosc. and Remote Sensing*, 24(4):624–648, July 1986.

[68] R. Meyer, A.W.A. Duvenhage, J.H. De Beer, and R.M.J. Huyssen. A geophysical - geohydrological study along the Kuruman River in the Kuruman and Gordonia Districts. *Transactions of the Geological Society of South Africa*, 88:501–515, 1985.

[69] F. Netterberg. Geology of Southern African Calcretes : Terminology, Description, Macrofeatures and Classification. *Transactions of the Geological Society of South Africa*, 83:255–283, 1980.

[70] A. Robert Newton. Private communications. Department of Geology, University of Cape Town, 1992.

[71] Yisok Oh, Kamal Sarabandi, and Fawwaz T. Ulaby. An Empirical Model and Inversion Technique for Radar Scattering from Bare Soil Surfaces. *IEEE Transactions on Geosc. and Remote Sensing*, 30(2):370–381, March 1992.

[72] Gary R. Olhoeft. Direct detection of hydrocarbon and organic chemicals with ground penetrating radar and complex resistivity. In *Proceedings of the NWWA/API Conference on Petroleum Hydrocarbons and Organic Chemicals in Ground Water*, pages 284–305, November 1986.

[73] Gary R. Olhoeft. Electrical properties from 10^{-3} to 10^{+9} Hz: Physics and Chemistry. In *Proceedings of the 2nd International Symposium on the Physics and Chemistry of Porous Media*, pages 281–298, October 1986.

[74] Michel Petit, Jean-Michel Stretta, Henri Farrugio, and Alain Wadsworth. Synthetic Aperture Radar Imaging of Sea Surface Life and Fishing Activities. *IEEE Transactions on Geosc. and Remote Sensing*, 30(5):1085–1089, September 1992.

[75] H. K. Ramapriyan, James P. Strong, Yubin Hung, and Charles W. Murray. Automated Matching of Pairs of SIR-B Images for Elevation Mapping. *IEEE Transactions on Geosc. and Remote Sensing*, 24(4):462–472, July 1986.

[76] D. Rankin and R. P. Singh. Effect of clay and salinity on the dielectric properties of rock. *Journal of Geophysical Research*, 90(B10):8793–8800, September 1985.

[77] R.F. Rawson and C.L. Liskow. Radar Reflectivity Measurements of Ocean Surface with and without a Surface Coat of Oil. In *1981 International Geoscience and Remote Sensing Symposium (IGARSS'81)*, pages 1268–1273. IEEE Geoscience and Remote Sensing Society, June 1981.

[78] Ladislav E. Roth and Charles Elachi. Coherent Electromagnetic Losses by Scattering from Volume Inhomogeneities. *IEEE Transactions on Antennas and Propagation*, pages 674–675, September 1975.

[79] R. S. Sayles and T. R. Thomas. Surface topography as a nonstationary random process. *Nature*, 271:431–434, 1978.

[80] Gerald G. Schaber, John F. McCauley, Carol S. Breed, and Gary R. Olhoeft. Shuttle Imaging Radar: Physical controls on signal penetration and subsurface scattering in the Eastern Sahara. *IEEE Transactions on Geosc. and Remote Sensing*, 24(4):603–623, July 1986.

[81] Waymond R. Scott and Glenn S. Smith. Measured Electrical Constitutive Parameters of Soil as Functions of Frequency and Moisture Content. *IEEE Transactions on Geosc. and Remote Sensing*, 30(3):621–623, May 1992.

[82] P. N. Sen, C. Scala, and M. H. Cohen. A self-similar model for sedimentary rocks with application to the dielectric constant of fused glass beads. *Geophysics*, 46(5):781–795, May 1981.

[83] Anatolij M. Shutko and E.M. Reutov. Mixture Formulas Applied in Estimation of Dielectric and Radiative Characteristics of Soils and Grounds at Microwave Frequencies. *IEEE Transactions on Geosc. and Remote Sensing*, 20(1):29–32, January 1982.

[84] Merrill Skolnik, editor. *Radar Handbook*. McGraw Hill, second edition, 1990.

[85] M.C. Smith, G. Vellidis, and D.L. Thomas. Measurement of Water Table Fluctuations in a sandy soil using Ground Penetrating Radar. *American Society of Agricultural Engineers*, 35(4):1161–1166, June 1992.

[86] M.A. Thomas and S.J. Malherbe. The Geology of the Nossob and Twee Rivieren areas. Department of Mineral and Energy Affairs, Geological Survey, East Street, Bellville, 1989.

[87] R.J. Thomas and M.A. Thomas. The Geology of the Noenieput area. Department of Mineral and Energy Affairs, Geological Survey, East Street, Bellville, 1989.

[88] S.G. Thomas. The Geomorphological role of vegitation in the the Dune System of the Kalahari. *Geomorphological Studies in Southern Africa*, pages 145–160, 1988.

[89] G.C. Topp, J.L. Davis, and A.P.Annan. Electromagnetic Determination of Soil Water Content: Measurements in Coaxial Transmission Lines. *Water Resources Research*, 16(3):574–582, June 1980.

[90] G.C. Topp, M. Yanuka, W.D. Zebchuk, and S. Zegelin. Determination of Electrical Conductivity Using Time Domain Reflectometry: Soil and Water Experiments in Coaxial Lines. *Water Resources Research*, 24(7):945–952, July 1988.

[91] Fawwaz T. Ulaby. Radar Response to Vegetation. *IEEE Transactions on Antennas and Propagation*, 23(1):36–45, January 1975.

[92] Fawwaz T. Ulaby, Percy P. Batlivala, and Myron C. Dobson. Microwave Backscatter Dependence on Surface Roughness, Soil Moisture, and Soil Texture: Part I - Bare Soil. *IEEE Transactions on Geoscience Electronics*, 16(4):286–295, October 1978.

[93] Fawwaz T. Ulaby and Gerald A. Bradley. Optimum Radar Parameters for Mapping Soil Moisture. *IEEE Transactions on Geoscience Electronics*, 14(2):81–93, April 1976.

[94] Fawwaz T. Ulaby, Gerald A. Bradley, and Myron C. Dobson. Microwave Backscatter Dependence on Surface Roughness, Soil Moisture, and Soil Texture: Part II - Vegetation-Covered Soil. *IEEE Transactions on Geoscience Electronics*, 17(2):33–40, April 1979.

[95] Fawwaz T. Ulaby and Myron C. Dobson. *Handbook of Radar Scattering Statistics for Terrain.* Artech House, 1989.

[96] Fawwaz T. Ulaby and Charles Elachi, editors. *Radar Polarimetry for Geoscience Applications.* Artech House, 1990.

[97] Fawwaz T. Ulaby, F. Kouyate, Adrian K. Fung, and Alois J. Sieber. A Backscatter Model for a Randomly Perturbed Periodic Surface. *IEEE Transactions on Geosc. and Remote Sensing*, 20(4):518–528, October 1982.

[98] Fawwaz T. Ulaby, Richard K. Moore, and Adrian K. Fung. *Microwave Remote Sensing, Active and Passive.* Addison-Wesley, 1981.

[99] Fawwaz T. Ulaby, Kamal Sarabandi, Kyle McDonald, Michael Whitt, and Myron C. Dobson. Michigan microwave canopy scattering model. *International Journal of Remote Sensing*, 11(7):1223–1253, 1990.

[100] J. van der Berg, P. Swart, and B. Lacquet. Microwave Properties of Phosphate Rock. *Journal of Microwave Power and Electromagnetic Energy*, 27(3):183–189, 1992.

[101] Jakob J. van Zyl. Unsupervised Classification of Scattering Behaviour Using Radar Polarimetry Data. *IEEE Transactions on Geosc. and Remote Sensing*, 27(1):36 – 45, January 1989.

[102] Jakob J. van Zyl, Charles F. Burnette, and Tom G. Farr. Inference of Surface Power Spectra from Inversion of Multifrequency Polarimetric Radar Data. *Geophysical Research Letters*, 18(9):1787 – 1790, September 1991.

[103] Jakob J. van Zyl, Howard A. Zebker, and Charles Elachi. Imaging radar polarization signatures: Theory and Observation. *Radio Science*, 22(4):529–543, July-August 1987.

[104] James R. Wang. The dielectric properties of soil-water mixtures at microwave frequencies. *Radio Science*, 15(5):977–985, September 1980.

[105] James R. Wang, Edwin T. Engman, James C. Shiue, M. Rusek, and Charlotte Steinmeier. The SIR-B Observations of Microwave Backscatter Dependence on Soil Moisture, Surface Roughness, and Vegetation Covers. *IEEE Transactions on Geosc. and Remote Sensing*, 24(4):510–516, July 1986.

[106] James R. Wang and Thomas J. Schmugge. An empirical model for the complex dielectric permittivity of soils as a function of water content. *IEEE Transactions on Geosc. and Remote Sensing*, 18(4):288–295, October 1980.

[107] Robert L. Wildey. Radarclinometry for the Venus Radar Mapper. *Photogrammetric Engineering and Remote Sensing*, 52(1):41–50, January 1986.

[108] Darold Wobschall. A theory of the complex dielectric permittivity of soil containing water: The semidisperse model. *IEEE Transactions on Geoscience Electronics*, 15(1):49–58, January 1977.

[109] Paul F. Worthington. Geophysical investigations of groundwater resources in the Kalahari Basin. *Geophysics*, 42(4):838–849, June 1977.

[110] Howard A. Zebker. Decorrelation in Interferometric Radar Echoes. *IEEE Transactions on Geosc. and Remote Sensing*, 30(5):950–959, September 1992.

[111] Howard A. Zebker and Richard. M. Goldstein. Topographic Mapping From Interferometric Synthetic Aperture Radar Observations. *Journal of Geophysical Research*, 91(B5):4993–4999, April 1986.

[112] Howard A. Zebker, Jan Martin, Soren N. Madsen, Kevin B. Wheeler, Timothy Miller, Yunling Lou, Giovanni Alberti, and Sergio Vetrella. The TOPSAR Interferometric Radar Topographic Mapping Instrument. *IEEE Transactions on Geosc. and Remote Sensing*, 30(5):933–940, September 1992.

[113] Howard A. Zebker and Jakob J. van Zyl. Imaging Radar Polarimetry From Wave Synthesis. *Journal of Geophysical Research*, 92(B1):683–701, January 1987.